The Dissertation Committee for Hamidreza Mashayekh
certifies that this is the approved version of the following dissertation:

Parameter estimation in layered media using dispersion-constrained full waveform inversion

Committee:

Loukas F. Kallivokas, Co-supervisor

John L. Tassoulas, Co-supervisor

Lance Manuel

Mark Mear

Kenneth H. Stokoe

Parameter estimation in layered media using dispersion-constrained full waveform inversion

by

Hamidreza Mashayekh

DISSERTATION

Presented to the Faculty of the Graduate School of

The University of Texas at Austin

in Partial Fulfillment

of the Requirements

for the Degree of

DOCTOR OF PHILOSOPHY

THE UNIVERSITY OF TEXAS AT AUSTIN

August 2018

To my kind and patient wife.

To my adorable son.

To my beloved mother and father,
whose unconditional love, support and sacrifice have lit my life.

Acknowledgments

I would like to express my sincere gratitude and appreciation to my doctoral co-advisors, Professor Loukas F. Kallivokas and Professor John L. Tassoulas, for their assistance and supervision of this work. I am thankful to Professors Kenneth Stokoe, Lance Manuel, and Mark Mear, for serving on my dissertation committee, and for their valuable comments. I want to express my gratitude to Professors Robert Gilbert and Maria Juenger, who supported me when I needed most. My sincere thanks also goes to Professors Jon Olson and Masa Prodanovic, who gave me the chance to serve as the instructor and teacher assistant of the Numerical methods and programming course, which supported me during this research.

I also wish to thank Dr. Arash Fathi, Dr. Babak Poursartip, Dr. Seungbum Koo, Heedong Goh, Dr. Saeed Enayatpour, Dr. Mir Mohammad Sadeghi and Mohsen Babazadeh for their valuable help and friendship.

I cannot express my gratitude to my mother, father, brothers, wife, and son, who supported and encouraged me in this study. This couldn't happen without their unconditional love and support.

Parameter estimation in layered media using dispersion-constrained full waveform inversion

Publication No. _____

Hamidreza Mashayekh, Ph.D.
The University of Texas at Austin, 2018

Supervisors: Loukas F. Kallivokas
John L. Tassoulas

The need to estimate the properties of layered elastic or viscoelastic media arises commonly in various engineering applications, including geotechnical site characterization and pavement condition assessment. The layered medium is usually probed with small-amplitude waves, and the medium's response is used to drive an inverse medium problem leading to the identification of the properties. In this dissertation, we solve the property estimation problem by a new methodology that seeks to minimize the misfit between measured and computed responses, constrained by the dispersion relation of the layered medium; the latter expressed in terms of the forward eigenvalue problem and the associated orthonormality condition. The medium's properties are recovered upon satisfaction of the first-order optimality conditions of the system's Lagrangian. Next, we extend the methodology for the characterization of a finite-depth layered elastic medium to the case of a layered medium underlain

by a halfspace. The layered medium is treated using a Thin Layer Method (TLM), while the halfspace is treated with the introduction of a Perfectly-Matched-Layer (PML). The PML adds complexity to the dispersion relation, including non-physical modes, which will be addressed systematically to resolve the medium's characterization. Effectively, the physical setting and the modeling choices reduce the originally three-dimensional problem to one spatial dimension along only the depth of the medium. Then, we discuss the extension of the methodology for estimating the mechanical properties and the stratification of horizontally-layered soils using surface records of soil motion induced by the passing of trains or other moving loads. At each step, we report numerical results and demonstrate the method's capabilities and effectiveness, and discuss how the technique can be used for field applications.

Table of Contents

List of Figures

Chapter 1

Introduction

The dissertation focuses on the full-waveform-based property estimation of layered media. The dissertation consists of three journal papers, each of which is focusing on a particular topic of the developed methodology. Specifically:

In the first paper, entitled *"Parameter estimation in layered media using dispersion-constrained inversion,"* we have tackled the problem of estimating the material properties of a layered stratum. We solve the property estimation problem by a new methodology that seeks to minimize the misfit between measured and computed responses, constrained by the dispersion relation of the layered medium; the latter is expressed in terms of the forward eigenvalue problem and the associated orthonormality condition. The medium's properties are recovered upon satisfaction of the first-order optimality conditions of the system's Lagrangian. Numerical results based on stationary dynamic loads demonstrate the efficiency of the method. This paper, co-authored by Hamidreza Mashayekh, Loukas F. Kallivokas, and John L. Tassoulas, was submitted to the Journal of Engineering Mechanics for publication and is currently in press.

The second paper, entitled *"Dispersion-constrained full-waveform inversion in a layered halfspace,"* extends the methodology to the case of a layered halfspace. To mimic the halfspace, a Perfectly-Matched-Layer (PML) absorbing boundary condition is used. The presence of the PML results in non-physical modes, which are filtered out using an energy criterion. Numerical results are included, attesting to the ability of the extended method to reconstruct the properties of a layered halfspace. This paper, co-authored by Hamidreza Mashayekh, Loukas F. Kallivokas, and John L. Tassoulas, has been submitted to Computational Geosciences for possible publication, and is currently under review.

In the third paper, entitled *"Layered soil parameter estimation from a moving load,"* the methodology has been extended to account for moving loads. The core methodology remains the same, but modifications to accommodate the moving loads are included. Specifically, instead of driving the inversion by the response misfit, the inversion is driven by a Green's function misfit. A procedure suitable for field implementation has also been developed. Numerical results featuring realistic train loads, attest to the method's capabilities. This paper, co-authored by Hamidreza Mashayekh and Loukas F. Kallivokas, has been submitted to Soil Dynamics and Earthquake Engineering for possible publication, and is currently under review.

Chapter 2

Parameter estimation in layered media using dispersion-constrained inversion [1]

2.1 Introduction

In many engineering applications, it is desirable or required to characterize the mechanical properties of a semi-infinite medium by means of nondestructive tests. These applications may pertain to deep earth structures, as in exploration geophysics [59], or to the near-surface layers, as in the condition evaluation of pavements [24, 33] or in geotechnical site characterization [37]. In nondestructive tests for such applications, the medium is probed with waves, –elastic, acoustic, or electromagnetic–, the response is recorded, and the distribution of material properties (e.g., shear modulus) is determined by an inversion procedure [38].

For near-surface problems, of interest in this article, the applications that drive most developments to date originate from infrastructure assessment needs. For example, one of the most-widely used nondestructive tests for pavement condition assessment is the Falling Weight Deflectometer (FWD) test in which the medium is probed using an impulse load and the response

[1] Hamidreza Mashayekh, Loukas F. Kallivokas, John L. Tassoulas

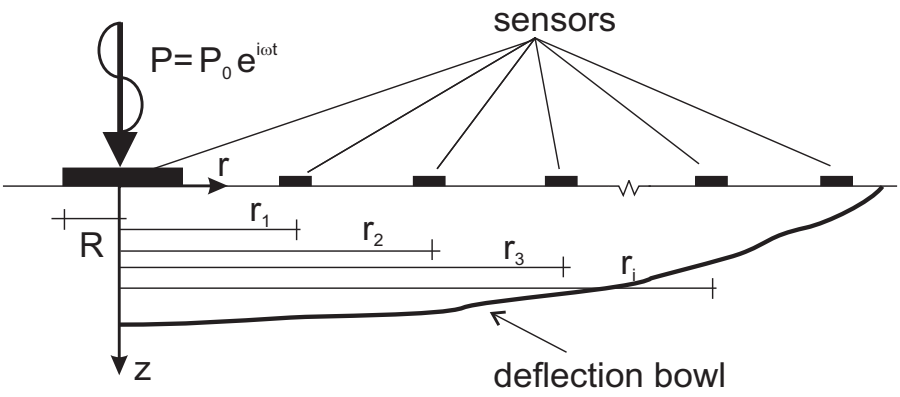

Figure 2.1: Schematic drawing of FWD field test: dynamic load, sensor locations, and induced surface deflection bowl

is measured at a number of sensor locations (Fig. 2.1). Several attempts have been made toward interpretation of FWD test results and extraction of the desired properties of the layered medium. In the context of pavement condition assessment, the property extraction procedures are usually referred to as backcalculations of the relevant properties. In general, backcalculation procedures can be categorized into static and dynamic, on the basis of whether the theoretical response at sensor locations is computed by static analysis or the true dynamic nature of the test is considered. In the static approach, the maximum displacements of the medium at sensor locations are calculated by static elasticity and matched to maximum displacements recorded by sensors. This approach is widely used because of its simplicity and speed, but several studies have shown that static backcalculation results are not reliable [25, 53, 54, 78]. In the dynamic approach, the response is calculated via an appropriate forward elastodynamic analysis, and the results are matched to

measured displacements. The dynamic forward problem is implemented either in the time [47, 49] or frequency [36, 77] domains. Most frequency-domain procedures [31, 82, 83] are built on the stiffness-matrix formulation introduced by Kausel and Roësset [40], with further developments by Doyle [18] and Al-Khoury et al. [4].

Various techniques have been implemented for the backcalculation of properties [33]. They can be categorized as (i) closed-form solutions [1, 34, 70]; (ii) database searches [6, 14]; (iii) optimization techniques [12, 35, 73]; (iv) regression analysis [5, 52, 67]; and (v) neural nets or evolutionary algorithms [23, 56, 57, 66, 69, 72]. Most of the reported techniques are either of an *ad hoc* nature, or resort to simplifying assumptions that are inconsistent with the underlying physical problem (e.g. static versus dynamic).

While progress in the imaging of the near-surface layered media is ongoing, a robust solution remains elusive, possibly because the developed methodologies have not benefited, or have not sought to benefit, from recent advances in related fields. The near-surface imaging problem belongs to a broader class of wave-driven inverse medium problems, where, for example, "backcalculation" refers to, and/or is replaced by, "inversion" (another term that is often used is parameter identification). The tackling of such inverse medium problems is often cast in the context of a partial-differential-equation-constrained optimization framework, whereby a suitably-chosen and application-specific objective functional is sought to be minimized, constrained by the underlying physics, the latter expressed in terms of the governing differential equa-

tions [2, 11, 21, 38, 60]. The technical apparatus for casting and resolving the optimization problem is rooted in the early work of Lions [46]. Such problems, including the one of interest herein, are ill-posed, and typically admit multiple solutions, some physical and some non-physical. To further narrow the range of possible solutions for the distribution of the properties, several schemes may be used, aimed either at the regularization of the solution, a process that may filter out non-physical solutions (via, e.g., Tikhonov regularization), or aimed at improving the optimizer's ability to converge to the true (and unique) solution via, possibly physics-based, numerical schemes.

In this paper, we borrow from, and improve upon, recent developments in wave-driven inverse medium problems. Specifically, we focus on the problem of a horizontally-layered medium subjected to a surface disc load (Fig. 2.1), and seek to reconstruct the properties of the layers using the recorded surface displacements. We too take the route of casting the inverse medium problem as a constrained optimization problem, but opt to describe the underlying physics constraint by the associated eigenvalue problem instead of using differential equations. In principle, any form encompassing the physics of the problem could serve as a constraint (e.g., differential or integral equations). Here, using differential equations as a constraint would result in a two-dimensional problem in either the time or the frequency domain, even under the present conditions of axisymmetry. The motivation for using the eigenvalue problem as a constraint stems from the fact that by using expansions of the displacement in the horizontal directions, which, in turn, give rise to an eigenvalue

problem, the spatial dimensionality of the problem is reduced to one, entailing computational gains. Thus, using the eigenvalue problem, i.e., the dispersion relation, appears to be an optimal choice for the problem at hand. In the context of the inverse medium problem of interest herein, using the dispersion relation as a constraint is new; one notable exception where the eigenvalue problem was used as a constraint for shape optimization purposes is the work in [3].

To obtain the associated eigenvalue problem of a semi-infinite layered medium we describe the forward full-waveform problem in the frequency domain, based on the thin-layer method [39]: the displacement components in the layered medium are computed using a semidiscrete approach, analytical in all horizontal directions but discrete (numerical) in the medium's depth direction (semi-infinite). To find the property distribution, i.e., to *invert* or *backcalculate*, we seek a stationary point to the problem's Lagrangian, where the latter consists of the misfit between computed and measured responses at various sensor locations, augmented by the imposition of the dispersion relation (eigenvalue problem) and the mode-shape orthonormality conditions. The medium's properties are extracted by enforcing the first-order optimality conditions of the system's Lagrangian. A similar physical problem was considered by Astaneh and Guddati [7], where the inversion was driven by the misfit between computed and experimentally-obtained phase velocities. It is worth noting that the development in [7] is intended for inversion on the basis of tests in which surface waves are generated and observed in the far field, while our

methodology employs arbitrary near-field as well as far-field measurements.

We report numerical results based on synthetic records, attesting to the effectiveness of our approach.

2.2 Problem definition

To highlight the dispersion-constrained inversion approach, we focus on the simplest possible identification problem, typically associated with the condition assessment of pavements. Accordingly, we consider a horizontally-layered medium, comprising n elastic or viscoelastic layers, subjected to a dynamic load applied vertically on the surface of the medium (Fig. 2.2(a)). For simplicity, but without loss of generality in the methodology discussed herein, we assume that the medium is fixed at the bottom. In general, each i-th layer is characterized by the shear modulus G_i, Poisson's ratio ν_i, mass density ρ_i, thickness h_i, and material damping β_i. The load is applied normal to the surface at the disc's center: we assume the load to be harmonic at an operating frequency ω, i.e., $P = P_0 e^{i\omega t}$, where P_0 is the amplitude of the applied load. Given the symmetry of the problem about the vertical load axis, the problem can be formally reduced to an axisymmetric problem cast in the (r, z) system, as shown in Fig. 2.2(b), where the origin coincides with the disc's center, r denotes radial distance from the origin, and z denotes depth, measured from the surface.

For the purpose of the ensuing discussion, we assume that all layer parameters are *a priori* known, except for the shear moduli and the layer thick-

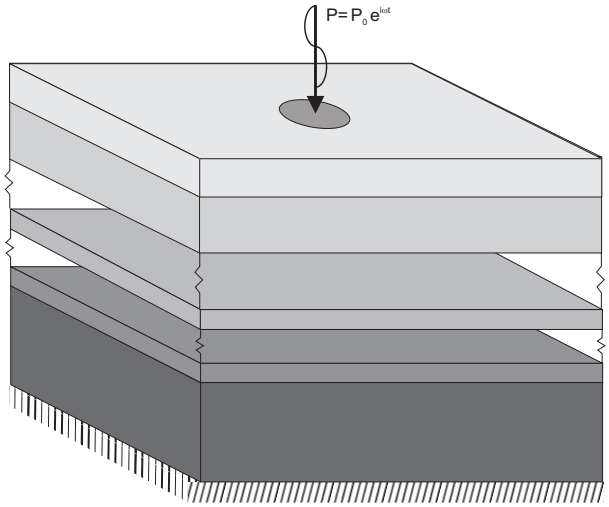

(a) In three dimensions

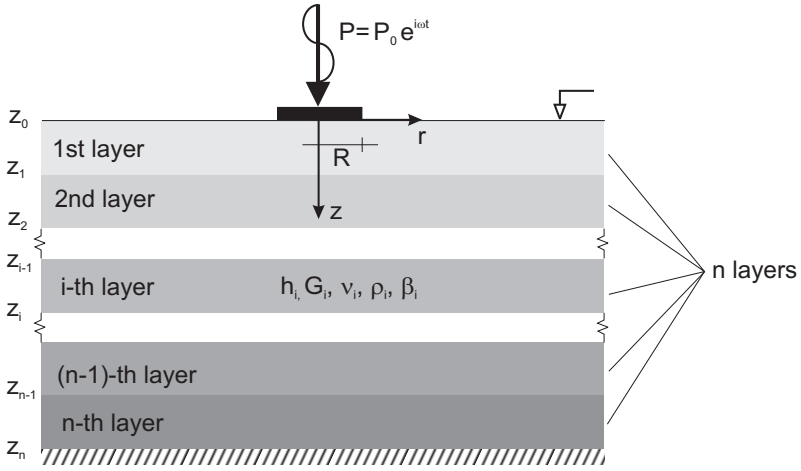

(b) In two dimensions (axisymmetric case)

Figure 2.2: Layered media subjected to a stationary dynamic load

nesses, even though, in typical field operations, the layer thicknesses can be obtained by GPR (Ground Penetrating Radar) imaging. Therefore, although the inversion framework can be used to invert for any layer parameters, here, for the sake of simplicity, we assume that the density, Poisson's ratio, and damping can be estimated reasonably well from other information, e.g, clayey vs. sandy layer, prior to shear-modulus inversion. We note that there is no need to *a priori* know the number of layers: if the number of layers is known, the inversion process can be further constrained to advantage. However, in the general case, when the number of layers is not known, the number is recovered *indirectly*, once the shear modulus distribution is obtained. We also remark that the inverse methodology discussed herein can accommodate additional unknown parameters (e.g., damping), at the expense of increased complexity and computational cost, but without any substantive modification to the inversion framework/algorithm.

Thus, our goal is to recover the shear moduli G_i for all n layers ($i = 1...n$), when given the response of the medium to a known excitation, the latter measured at one or multiple surface sensors. The dispersion-constrained approach discussed herein requires that the misfit between the measured displacement and the computed displacement, where the latter corresponds to a trial guess of the layered medium's properties, be minimized. In addition, we require that the physics of the underlying problem be satisfied: we express the physics of the problem in terms of the associated eigenvalue problem, which we use as a minimization constraint –thence, the *dispersion-constrained* ter-

minology. The inversion is carried out exclusively in the frequency domain; however, time-domain records can also be used if first processed via Fourier transforms.

2.3 The forward eigenvalue problem

To set the stage for the dispersion-constrained inversion, we review first the forward eigenvalue problem; most of the technical details can be found in [39]. Here we report the key steps from [39] for completeness.

For any layer i (Fig. 2.2(b)), the equilibrium equations in cylindrical coordinates and in the frequency domain can be written as (an $e^{i\omega t}$ harmonic term has been assumed throughout):

$$\frac{\partial \tilde{\sigma}_r}{\partial r} + \frac{\tilde{\sigma}_r - \tilde{\sigma}_\theta}{r} + \frac{\partial \tilde{\tau}_{rz}}{\partial z} = -\rho_i \omega^2 \tilde{u}, \tag{2.1a}$$

$$\frac{\partial \tilde{\tau}_{rz}}{\partial r} + \frac{\tilde{\tau}_{rz}}{r} + \frac{\partial \tilde{\sigma}_z}{\partial z} = -\rho_i \omega^2 \tilde{w}, \tag{2.1b}$$

where, at the top surface ($z = 0$):

$$\tilde{\sigma}_z = \begin{cases} q & , \quad 0 \le r \le R \\ 0 & , \quad R \le r \end{cases} \tag{2.2}$$

In (2.2), $q = \frac{P_0}{\pi R^2}$ is the stress amplitude on the surface when a harmonic load $P_0 e^{i\omega t}$ is applied on the disc of radius R. Due to the axisymmetric character of the problem, the dependence on the polar angle has been dropped, and consequently, the radial component of the displacement $\tilde{u} \equiv \tilde{u}(r, z)$, and the

vertical component of the displacement $\tilde{w} \equiv \tilde{w}(r, z)$. Customary notation has been adopted for the Fourier-transformed normal and shear stress components $\tilde{\sigma}_r$, $\tilde{\sigma}_\theta$, $\tilde{\sigma}_z$, $\tilde{\tau}_{rz}$. Similarly, combining the constitutive law for a linear elastic material, and the small-strain kinematic conditions, leads to the equations of motion for the i-th layer:

$$(\lambda_i + 2G_i)\left(\frac{\partial^2 \tilde{u}}{\partial r^2} + \frac{1}{r}\frac{\partial \tilde{u}}{\partial r} - \frac{\tilde{u}}{r^2}\right) + G_i \frac{\partial^2 \tilde{u}}{\partial z^2} + (\lambda_i + G_i)\frac{\partial^2 \tilde{w}}{\partial r \partial z} + \rho_i \omega^2 \tilde{u} = 0, \tag{2.3a}$$

$$(\lambda_i + 2G_i)\frac{\partial^2 \tilde{w}}{\partial z^2} + G_i\left(\frac{\partial^2 \tilde{w}}{\partial r^2} + \frac{1}{r}\frac{\partial \tilde{w}}{\partial r}\right) + (\lambda_i + G_i)\left(\frac{1}{r}\frac{\partial \tilde{u}}{\partial z} + \frac{\partial^2 \tilde{u}}{\partial r \partial z}\right) + \rho_i \omega^2 \tilde{w} = 0. \tag{2.3b}$$

where λ_i is the first Lamé constant of the i-th layer. Using separation of variables and the eigenfunctions, the displacement components can be written as:

$$\begin{bmatrix} \tilde{u}(r, z) \\ \tilde{w}(r, z) \end{bmatrix} = \begin{bmatrix} H_1^{(2)}(kr) & 0 \\ 0 & H_0^{(2)}(kr) \end{bmatrix} \begin{bmatrix} u(z) \\ w(z) \end{bmatrix}, \tag{2.4}$$

where k is the wavenumber, $u(z)$ and $w(z)$ are the radial and vertical displacement components, and $H_0^{(2)}(kr)$ and $H_1^{(2)}(kr)$ denote the 0-th and 1-st order Hankel functions of the second kind, respectively. Introducing (2.4) into (2.3), results in:

$$-k^2(\lambda_i + 2G_i)u + G_i \frac{d^2 u}{dz^2} - k(\lambda_i + G_i)\frac{dw}{dz} + \rho_i \omega^2 u = 0, \tag{2.5a}$$

$$-k^2 G_i w + (\lambda_i + 2G_i)\frac{d^2 w}{dz^2} + k(\lambda_i + G_i)\frac{du}{dz} + \rho_i \omega^2 w = 0. \tag{2.5b}$$

The strong form of the forward problem can be cast as: find the displacement components (u, w) for each layer i, subject to fixed conditions $(u = w = 0)$ at z_n (Fig. 2.2(b)), to the continuity of displacements and tractions along the layer interfaces, z_{i-1} and z_i for all i, and to traction-free conditions $(\tilde{\sigma}_z = \tilde{\tau}_{rz} = 0)$ everywhere along the surface z_0 $(z = 0)$, except under the load. Next, following a standard Galerkin approach, the weak form for the i-th layer with $z \in (z_{i-1}, z_i)$ becomes:

$$k^2(\lambda_i + 2G_i)\int_{z_{i-1}}^{z_i} u\check{u}dz + k\lambda_i \int_{z_{i-1}}^{z_i} \frac{dw}{dz}\check{u}dz - G_i \int_{z_{i-1}}^{z_i} \frac{d}{dz}\left[\frac{du}{dz} - kw\right]\check{u}dz - \rho_i\omega^2 \int_{z_{i-1}}^{z_i} u\check{u}dz = 0, \tag{2.6a}$$

$$k^2 G_i \int_{z_{i-1}}^{z_i} w\check{w}dz - kG_i \int_{z_{i-1}}^{z_i} \frac{du}{dz}\check{w}dz - \int_{z_{i-1}}^{z_i} \frac{d}{dz}\left[(\lambda_i + 2G_i)\frac{dw}{dz} + k\lambda_i u\right]\check{w}dz - \rho_i\omega^2 \int_{z_{i-1}}^{z_i} w\check{w}dz = 0, \tag{2.6b}$$

where, $\check{u}(z)$ and $\check{w}(z)$ are admissible test functions. After integration by parts, and collecting like-terms, there results:

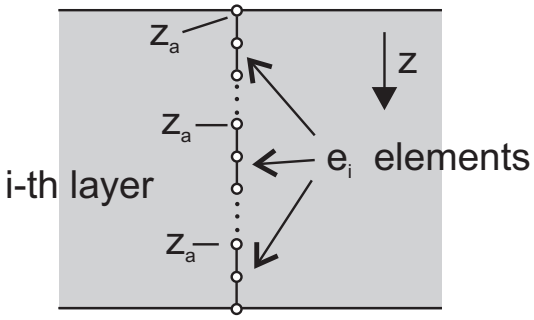

Figure 2.3: i-th layer discretization into e_i elements

$$k^2(\lambda_i+2G_i)\int_{z_{i-1}}^{z_i} u\check{u}dz + k\Big[\lambda_i\int_{z_{i-1}}^{z_i}\frac{dw}{dz}\check{u}dz - G_i\int_{z_{i-1}}^{z_i} w\frac{d\check{u}}{dz}dz\Big]$$
$$+ G_i\int_{z_{i-1}}^{z_i}\frac{du}{dz}\frac{d\check{u}}{dz}dz - \rho_i\omega^2\int_{z_{i-1}}^{z_i} u\check{u}dz = G_i\Big[\frac{du}{dz} - kw\Big]\,\check{u}\,\Big|_{z_{i-1}}^{z_i} = \hat{\tau}_{rz}\,\check{u}\,\Big|_{z_{i-1}}^{z_i}, \tag{2.7a}$$

$$k^2G_i\int_{z_{i-1}}^{z_i} w\check{w}dz - k\Big[G_i\int_{z_{i-1}}^{z_i}\frac{du}{dz}\check{w}dz - \lambda_i\int_{z_{i-1}}^{z_i} u\frac{d\check{w}}{dz}dz\Big]$$
$$+ (\lambda_i+2G_i)\int_{z_{i-1}}^{z_i}\frac{dw}{dz}\frac{d\check{w}}{dz}dz - \rho_i\omega^2\int_{z_{i-1}}^{z_i} w\check{w}dz$$
$$= \Big[(\lambda_i+2G_i)\frac{dw}{dz} + k\lambda_i u\Big]\,\check{w}\,\Big|_{z_{i-1}}^{z_i} = \hat{\sigma}_z\,\check{w}\,\Big|_{z_{i-1}}^{z_i}, \tag{2.7b}$$

where, $\hat{\tau}_{rz} = \tilde{\tau}_{rz}/H_1^{(2)}(kr)$ and $\hat{\sigma}_z = \tilde{\sigma}_z/H_0^{(2)}(kr)$. We note that upon assembly of all the layers, the right-hand-sides of equations (2.7) will sum up to zero, due to the continuity and boundary conditions. Next, each layer i is discretized into e_i elements (Fig. 2.3). The displacement components of the trial pair (u, w) and of the test pair $(\check{u}, \check{w})$ are approximated within each element using standard Lagrange shape functions. Accordingly, within each layer i:

$$u(z) = \boldsymbol{\phi}^T(z)\,\boldsymbol{u} \quad , \quad w(z) = \boldsymbol{\phi}^T(z)\,\boldsymbol{w}, \tag{2.8}$$

where $\boldsymbol{u}$ and $\boldsymbol{w}$ are vectors of the nodal values of the radial and vertical displacement components, respectively, and $\boldsymbol{\phi}(z)$ are vectors of shape functions within each layer. For example, if the element shape functions are of polynomial degree d, then the vector $\boldsymbol{\phi}(z)$ has dimension $e_i d + 1$. There results the following quadratic eigenvalue problem in terms of the wavenumber k and the eigenvectors $\boldsymbol{U}$:

$$(k^2\mathbf{A} + k\mathbf{B} + \mathbf{G} - \omega^2\mathbf{M})\boldsymbol{U} = \mathbf{0} \quad ; \quad \boldsymbol{U} = \begin{bmatrix} \boldsymbol{u} \\ \boldsymbol{w} \end{bmatrix}. \tag{2.9}$$

$\mathbf{A}$,$\mathbf{B}$,$\mathbf{G}$ and $\mathbf{M}$ are global matrices assembled using the individual layer matrices, i.e.,

$$\mathbf{A} = \bigcup_{i=1}^{n} \mathcal{A}_i \quad ; \quad \mathbf{B} = \bigcup_{i=1}^{n} \mathcal{B}_i \quad ; \quad \mathbf{G} = \bigcup_{i=1}^{n} \mathcal{G}_i \quad ; \quad \mathbf{M} = \bigcup_{i=1}^{n} \mathcal{M}_i, \tag{2.10}$$

where the i-th layer matrices $\mathcal{A}_i$,$\mathcal{B}_i$,$\mathcal{G}_i$ and $\mathcal{M}_i$ are defined as:

$$\mathcal{A}_i = \begin{bmatrix} (\lambda_i + 2G_i) \int_{z_{i-1}}^{z_i} \boldsymbol{\phi}\boldsymbol{\phi}^T dz & 0 \\ 0 & G_i \int_{z_{i-1}}^{z_i} \boldsymbol{\phi}\boldsymbol{\phi}^T dz \end{bmatrix},$$

$$\mathcal{B}_i = \begin{bmatrix} 0 & \lambda_i \int_{z_{i-1}}^{z_i} \boldsymbol{\phi}\boldsymbol{\phi}'^T dz - G_i \int_{z_{i-1}}^{z_i} \boldsymbol{\phi}'\boldsymbol{\phi}^T dz \\ \lambda_i \int_{z_{i-1}}^{z_i} \boldsymbol{\phi}'\boldsymbol{\phi}^T dz - G_i \int_{z_{i-1}}^{z_i} \boldsymbol{\phi}\boldsymbol{\phi}'^T dz & 0 \end{bmatrix},$$

$$\mathcal{G}_i = \begin{bmatrix} G_i \int_{z_{i-1}}^{z_i} \boldsymbol{\phi}'\boldsymbol{\phi}'^T dz & 0 \\ 0 & (\lambda_i + 2G_i) \int_{z_{i-1}}^{z_i} \boldsymbol{\phi}'\boldsymbol{\phi}'^T dz \end{bmatrix},$$

$$\mathcal{M}_i = \rho_i \begin{bmatrix} \int_{z_{i-1}}^{z_i} \boldsymbol{\phi}\boldsymbol{\phi}^T dz & 0 \\ 0 & \int_{z_{i-1}}^{z_i} \boldsymbol{\phi}\boldsymbol{\phi}^T dz \end{bmatrix}. \tag{2.11}$$

We note that each of above layer matrices has dimension $[2(e_i d+1)] \times [2(e_i d+1)]$. The discrete quadratic eigenvalue problem (2.9) admits $2N$ eigenvalues (the wavenumbers k) and $2N$ eigenvectors (modes), where N is the

total number of degrees of freedom, defined as:

$$N = \sum_{i=1}^{n} 2e_i d \ . \tag{2.12}$$

For each wavenumber k, $-k$ is also an eigenvalue, and, thus, the $2N$ wavenumbers are arranged in N pairs of the form $(k, -k)$. Since the wavenumbers with positive imaginary part correspond to propagating modes that grow away from the origin, only half of the wavenumbers are physically acceptable, i.e., from each pair $(k, -k)$, only the wavenumber with negative imaginary part will be retained. For the N surviving modes, we choose a normalization of the eigenvectors, similar to the one used by Kausel [39] and Waas [79]:

$$\frac{1}{2}\boldsymbol{U}_s^T(2k_s\mathbf{A} + \mathbf{B})\boldsymbol{U}_s = k_s \qquad , \qquad s = 1, 2, ..., N \ . \tag{2.13}$$

Then, as shown in [39], the radial and vertical displacement components within each layer i are given as:

$$\tilde{u}(r, z_a) = qR \sum_{s=1}^{N} U_{s,l}\ U_{s,\frac{N}{2}+1} I_{2s}(r)/k_s, \tag{2.14a}$$

$$\tilde{w}(r, z_a) = qR \sum_{s=1}^{N} U_{s,m}\ U_{s,\frac{N}{2}+1} I_{1s}(r), \tag{2.14b}$$

where s is the eigenmode/eigenvalue index. Within every layer i, the elements are numbered from the top of the layer, with z_a denoting the z coordinate at the beginning of the j-th element, with $j = 1, ..., e_i$ (Fig. 2.3). That is:

$$z_a = z_{i-1} + (j-1)\frac{z_i - z_{i-1}}{e_i} \qquad , \qquad j = 1, ..., e_i \; . \tag{2.15}$$

Thus, in (2.14) $U_{s,l}$ and $U_{s,m}$ denote the l-th and m-th components of the $\boldsymbol{U}_s$ eigenvector, respectively. We note that the $\boldsymbol{U}_s$ eigenvector's components are arranged such that all the $\frac{N}{2}$ radial components are first, followed by the $\frac{N}{2}$ vertical components. Accordingly:

$$l = 1 + d(j-1) \quad ; \quad m = \tfrac{N}{2} + 1 + d(j-1) \quad \text{if } i = 1 \tag{2.16a}$$

$$l = 1 + d(j-1) + \sum_{p=1}^{i-1} e_p d \quad ; \quad m = \tfrac{N}{2} + 1 + d(j-1) + \sum_{p=1}^{i-1} e_p d \quad \text{if } i \neq 1 \tag{2.16b}$$

Furthermore, $I_{1s}(r)$ and $I_{2s}(r)$ in (2.14) are defined as:

$$I_{1s}(r) = \begin{cases} \dfrac{\pi}{2\boldsymbol{i}k_s} J_0(k_s r) H_1^{(2)}(k_s R) - \dfrac{1}{R k_s^2}, & 0 \leq r \leq R \\ \dfrac{\pi}{2\boldsymbol{i}k_s} J_1(k_s R) H_0^{(2)}(k_s r), & R \leq r \end{cases} \tag{2.17a}$$

$$I_{2s}(r) = \begin{cases} \dfrac{\pi}{2\boldsymbol{i}} J_1(k_s r) H_1^{(2)}(k_s R), & 0 \leq r \leq R \\ \dfrac{\pi}{2\boldsymbol{i}} J_1(k_s R) H_1^{(2)}(k_s r), & R \leq r \end{cases} \tag{2.17b}$$

When the vertical displacements are measured on the surface ($z_a = 0$ or $z = 0$), at a distance r from the load, (2.14b) reduces to:

$$\tilde{w}(r,0) = qR\sum_{s=1}^{N}(U_{s,\frac{N}{2}+1})^2 I_{1s}(r). \tag{2.18}$$

We use expression (2.18) to define the misfit between measured and computed displacements (vertical component only). In summary, it should be noted that the eigenvalue problem (2.9) and the orthonormality condition (2.13) embody the physics of the problem and constitute the forward or state problem: both (2.9) and (2.13) must be satisfied, as the misfit is minimized. The inversion process is outlined in the next section.

2.4 The inverse problem

Our goal is to find the along-the-depth distribution of the shear modulus of the probed layered medium, when the medium is subjected to a known surface disc load. As discussed earlier, we assume that the density, Poisson's ratio, and damping are known. Thus, the first Lamé constant, is expressed as a function of the shear modulus G, i.e., $\lambda = \frac{2G\nu}{1-2\nu}$. Similarly, for viscoelastic layers, G is replaced by its complex counterpart $G(1+2i\beta)$.

A usual starting point in inverse-medium problems is the construction of a misfit functional defined most often as the difference, in the least-squares sense, between the measured response and a computed response. The computed response corresponds to a medium described by a set of assumed material properties, which we then seek to determine via an iterative process whose goal is to minimize the misfit. Accordingly, let $\mathfrak{F}$ denote the misfit functional

defined as:

$$\mathfrak{F} := \frac{1}{2}\sum_{i=1}^{N_s}\sum_{j=1}^{M_\omega}|\tilde{w}^{(j)}(r_i,0) - \tilde{w}_m^{(j)}(r_i,0)|^2 \,, \tag{2.19}$$

where N_s is the number of sensors, M_ω is the number of discrete frequencies at which sensor measurements are taken, $\tilde{w}^{(j)}(r_i,0)$ denotes the computed displacement of the layered medium at the j-th frequency on the surface and at distance r_i from the origin, and $\tilde{w}_m^{(j)}(r_i,0)$ denotes the measured displacement at the same point and the same frequency. As cast, functional (2.19) is the amplitude of the complex-valued misfit, and it is a reasonable choice, since it accounts for both the real and imaginary parts, or equivalently, it includes both amplitude and phase information. Expression (2.19) is capable of accounting for recorded data along the deflection bowl induced by the load and over a wide range of excitation frequencies.

To ensure that the physics of the underlying problem is always satisfied during the material inversion iterations, the misfit functional is augmented by the side imposition of the physics to produce the problem's Lagrangian. In general, the side imposition of the physics can be done in a variety of ways: for example, the strong, or a weak, form of the forward problem cast in terms of the governing differential equations, can be side-imposed via Lagrange multipliers. This, in fact, has been a commonly used strategy in partial-differential-equation-constrained optimization approaches for tackling inverse medium problems [21, 37, 46]. We argue that, in principle, any form, continuous or discrete, that faithfully captures the physics of the forward problem,

can be used in the Lagrangian. Here, the discrete eigenvalue problem (2.9), accompanied by the orthonormality condition (2.13), is our choice for describing the physics of the problem. Accordingly, we side-impose (2.9) and (2.13), via Lagrange multipliers, to the misfit functional, effectively constraining the misfit minimization by the dispersion relation. Thus:

$$\mathfrak{L} = \frac{1}{2}\sum_{i=1}^{N_s}\sum_{j=1}^{M_\omega}|\tilde{w}^{(j)}(r_i,0) - \tilde{w}_m^{(j)}(r_i,0)|^2 + \mathfrak{C}, \tag{2.20}$$

where $\mathfrak{C}$ is the dispersion constraint defined as:

$$\begin{aligned}\mathfrak{C} = \Re e\Big\{ &\sum_{j=1}^{M_\omega}\sum_{s=1}^{N} \boldsymbol{\lambda}_s^{(j)^T}(\mathbf{A}{k_s^{(j)}}^2 + \mathbf{B}k_s^{(j)} + \mathbf{G} - {\omega_j}^2\mathbf{M})\boldsymbol{U}_s^{(j)} \\ &+ \sum_{j=1}^{M_\omega}\sum_{s=1}^{N} \xi_s^{(j)}\left(\frac{1}{2}\boldsymbol{U}_s^{(j)^T}(2\mathbf{A}k_s^{(j)} + \mathbf{B})\boldsymbol{U}_s^{(j)} - k_s^{(j)}\right)\Big\},\end{aligned} \tag{2.21}$$

and $\boldsymbol{\lambda}_s^{(j)}$ is a vector of Lagrange multipliers used to side-impose the eigenvalue problem, and $\xi_s^{(j)}$ is a scalar Lagrange multiplier used for the side-imposition of the orthonormality condition. Since the matrices and eigenvalue parameters are complex, it is sufficient to side-impose only the real part of the product of the complex Lagrange multipliers by the eigenvalue problem and of the orthonormality condition. Next, introducing (2.17) and (2.18) in the Lagrangian, (2.20) becomes:

$$\mathfrak{L} = \frac{1}{2}\sum_{i=1}^{N_s}\sum_{j=1}^{M_\omega}\left|qR\sum_{s=1}^{N}\left[(U^{(j)}_{s,\frac{N}{2}+1})^2 I_{1s}^{(j)}(r_i)\right] - \tilde{w}_m^{(j)}(r_i,0)\right|^2 + \mathfrak{C}, \tag{2.22}$$

or, equivalently:

$$\mathfrak{L} = \begin{cases} \dfrac{1}{2}\displaystyle\sum_{j=1}^{M_\omega}\sum_{i=1}^{N_s}\left| qR\sum_{s=1}^{N}\left[(U^{(j)}_{s,\frac{N}{2}+1})^2\frac{\pi}{2\boldsymbol{i}k_s^{(j)}}J_0(k_s^{(j)}r_i)H_1^{(2)}(k_s^{(j)}R) - \frac{1}{Rk_s^{(j)^2}}\right] \right. \\ \qquad\qquad \left. -\tilde{w}_m^{(j)}(r_i,0)\right|^2 + \mathfrak{C}, \quad 0 \le r_i \le R \\ \dfrac{1}{2}\displaystyle\sum_{j=1}^{M_\omega}\sum_{i=1}^{N_s}\left| qR\sum_{s=1}^{N}\left[(U^{(j)}_{s,\frac{N}{2}+1})^2\frac{\pi}{2\boldsymbol{i}k_s^{(j)}}J_1(k_s^{(j)}R)H_0^{(2)}(k_s^{(j)}r_i)\right] \right. \\ \qquad\qquad \left. -\tilde{w}_m^{(j)}(r_i,0)\right|^2 + \mathfrak{C}, \quad R \le r_i \end{cases} \tag{2.23}$$

Definitions (2.22) and (2.23) of the Lagrangian are of the form:

$$\mathfrak{L} \equiv \mathfrak{L}(\boldsymbol{\lambda}_s^{(j)}, \xi_s^{(j)}, \boldsymbol{U}_s^{(j)}, k_s^{(j)}, G_c), \tag{2.24}$$

i.e., the Lagrangian functional is a function of the Lagrange multipliers $\boldsymbol{\lambda}_s^{(j)}$ and $\xi_s^{(j)}$, the state variables $\boldsymbol{U}_s^{(j)}$ and $k_s^{(j)}$, and the material parameters G_c. The latter are the shear moduli of all the elements in the discretization, assumed constant over each element.

2.4.1 Optimality conditions

Next, we seek a stationary point for $\mathfrak{L}$ by requiring that the first variations of $\mathfrak{L}$ vanish:

$$\nabla\mathfrak{L} = \begin{bmatrix} \delta_{\boldsymbol{\lambda}_s^{(j)},\xi_s^{(j)}}\mathfrak{L} \\ \delta_{\boldsymbol{U}_s^{(j)},k_s^{(j)}}\mathfrak{L} \\ \delta_{G_c}\mathfrak{L} \end{bmatrix} = 0\ . \tag{2.25}$$

i. The state problem:

Taking variations of the Lagrangian functional $\mathfrak{L}$ with respect to the Lagrange multipliers (or adjoint variables) $\boldsymbol{\lambda}_s^{(j)}$ and $\xi_s^{(j)}$ and setting them equal to zero, recovers the forward eigenvalue problem, i.e., equations (2.9) and (2.13):

$$\delta_{\boldsymbol{\lambda}_s^{(j)}}\mathfrak{L} = 0 \Rightarrow (\mathbf{A}_j {k_s^{(j)}}^2 + \mathbf{B}k_s^{(j)} + \mathbf{G}_j - {\omega_j}^2\mathbf{M}_j)\boldsymbol{U}_s^{(j)} = 0\ , \tag{2.26a}$$

$$\delta_{\xi_s^{(j)}}\mathfrak{L} = 0 \Rightarrow \frac{1}{2}{\boldsymbol{U}_s^{(j)}}^T(2\mathbf{A}_j k_s^{(j)} + \mathbf{B})\boldsymbol{U}_s^{(j)} = k_s^{(j)}\ . \tag{2.26b}$$

ii. The adjoint problem:

Similarly, we enforce the vanishing of the variation of $\mathfrak{L}$ with respect to the state variables, i.e., the wavenumbers $k_s^{(j)}$, and the eigenvectors $\boldsymbol{U}_s^{(j)}$. There results:

$$\begin{aligned}\delta_{\boldsymbol{U}_s^{(j)}}\mathfrak{L} = \Re e\left\{2qRU^{(j)}_{s,\frac{N}{2}+1}\sum_{i=1}^{N_s} I_{1s}^{(j)}(r_i)(\overline{\tilde{w}^{(j)}(r_i,0) - \tilde{w}_m^{(j)}(r_i,0)})\boldsymbol{W}_I{}^T\delta\boldsymbol{U}_s^{(j)}\right\}\\ +\Re e\Big\{\boldsymbol{\lambda}_s^{(j)T}(\mathbf{A}{k_s^{(j)}}^2 + \mathbf{B}k_s^{(j)} + \mathbf{G} - {\omega_j}^2\mathbf{M})\delta\boldsymbol{U}_s^{(j)}\\ + \xi_s^{(j)}{\boldsymbol{U}_s^{(j)}}^T(2\mathbf{A}k_s^{(j)} + \mathbf{B})^T\delta\boldsymbol{U}_s^{(j)}\Big\} = 0,\end{aligned} \tag{2.27}$$

or

$$\begin{aligned}(\mathbf{A}{k_s^{(j)}}^2 + \mathbf{B}k_s^{(j)} + \mathbf{G} - \omega_j^2\mathbf{M})^T\boldsymbol{\lambda}_s^{(j)} + (2\mathbf{A}k_s^{(j)} + \mathbf{B})\boldsymbol{U}_s^{(j)}\xi_s^{(j)}\\ = -2qRU^{(j)}_{s,\frac{N}{2}+1}\sum_{i=1}^{N_s} I_{1s}^{(j)}(r_i)(\overline{\tilde{w}^{(j)}(r_i,0) - \tilde{w}_m^{(j)}(r_i,0)})\boldsymbol{W}_I,\end{aligned} \tag{2.28}$$

and,

$$\delta_{k_s^{(j)}}\mathfrak{L} = \Re e\left\{ qR(U^{(j)}_{s,\frac{N}{2}+1})^2 \sum_{i=1}^{N_s} \hat{I}^{(j)}_{1s}(r_i)(\overline{\tilde{w}^{(j)}(r_i,0) - \tilde{w}^{(j)}_m(r_i,0)})\delta k_s^{(j)} \right\} + \Re e\left\{ \boldsymbol{\lambda}_s^{(j)^T}(2\mathbf{A}k_s^{(j)} + \mathbf{B})\boldsymbol{U}_s^{(j)}\delta k_s^{(j)} + \xi_s^{(j)}(\boldsymbol{U}_s^{(j)^T}\mathbf{A}\boldsymbol{U}_s^{(j)} - 1)\delta k_s^{(j)} \right\} = 0, \tag{2.29}$$

or

$$\boldsymbol{U}_s^{(j)^T}(2\mathbf{A}k_s^{(j)} + \mathbf{B})^T\boldsymbol{\lambda}_s^{(j)} + (\boldsymbol{U}_s^{(j)^T}\mathbf{A}\boldsymbol{U}_s^{(j)} - 1)\xi_s^{(j)} = -qR(U^{(j)}_{s,\frac{N}{2}+1})^2 \sum_{i=1}^{N_s} \hat{I}^{(j)}_{1s}(r_i)(\overline{\tilde{w}^{(j)}(r_i,0) - \tilde{w}^{(j)}_m(r_i,0)}). \tag{2.30}$$

In the above, $\boldsymbol{W}_I = \Big[0, \ldots 0, 1, 0, \ldots 0\Big]^T$, and

$$\hat{I}^{(j)}_{1s}(r) = \begin{cases} \dfrac{\pi\, i}{2k_s^{(j)}}[RJ_0(k_s^{(j)}r)H_2^{(2)}(k_s^{(j)}R) + rJ_1(k_s^{(j)}r)H_1^{(2)}(k_s^{(j)}R)] + \dfrac{2}{Rk_s^{(j)^3}} & , 0 \le r \le R \\ \dfrac{\pi\, i}{2k_s^{(j)}}[RJ_2(k_s^{(j)}R)H_0^{(2)}(k_s^{(j)}r) + rJ_1(k_s^{(j)}R)H_1^{(2)}(k_s^{(j)}r)] & , R \le r \end{cases} \tag{2.31}$$

Equations (2.28) and (2.30) constitute the adjoint problem, which is a symmetric system of $N+1$ linear equations, per:

$$\begin{bmatrix} (\mathbf{A}{k_s^{(j)}}^2 + \mathbf{B}k_s^{(j)} + \mathbf{G} - \omega_j^2\mathbf{M})^T & (2\mathbf{A}k_s^{(j)} + \mathbf{B})\boldsymbol{U}_s^{(j)} \\ {\boldsymbol{U}_s^{(j)}}^T(2\mathbf{A}k_s^{(j)} + \mathbf{B})^T & ({\boldsymbol{U}_s^{(j)}}^T\mathbf{A}\boldsymbol{U}_s^{(j)} - 1) \end{bmatrix} \begin{bmatrix} \boldsymbol{\lambda}_s^{(j)} \\ \xi_s^{(j)} \end{bmatrix} = \\ \begin{bmatrix} -2qRU^{(j)}_{s,\frac{N}{2}+1}\Big(\sum\limits_{i=1}^{N_s} I_{1s}^{(j)}(r_i)(\overline{\tilde{w}^{(j)}(r_i,0) - \tilde{w}_m^{(j)}(r_i,0)})\Big)\boldsymbol{W}_I \\ -qR(U^{(j)}_{s,\frac{N}{2}+1})^2\Big(\sum\limits_{i=1}^{N_s} \hat{I}_{1s}^{(j)}(r_i)(\overline{\tilde{w}^{(j)}(r_i,0) - \tilde{w}_m^{(j)}(r_i,0)})\Big) \end{bmatrix}, \tag{2.32}$$

Thus, the Lagrange multipliers, or adjoint variables, $\boldsymbol{\lambda}_s^{(j)}$ and $\xi_s^{(j)}$ are obtained as a solution of the linear system (2.32), which is driven by the (conjugated) misfit, as it can be seen from the right-hand-side of (2.32).

iii. The control problem:

Lastly, we take the variation of $\mathfrak{L}$ with respect to the element shear moduli G_c:

$$\begin{aligned} \delta_{G_c}\mathfrak{L} = \Re e\Bigg\{ &\sum_{j=1}^{M_\omega}\sum_{s=1}^{N} {\boldsymbol{\lambda}_s^{(j)}}^T\Big(\frac{\partial \mathbf{A}}{\partial G_c}{k_s^{(j)}}^2 + \frac{\partial \mathbf{B}}{\partial G_c}k_s^{(j)} + \frac{\partial \mathbf{G}}{\partial G_c}\Big)\boldsymbol{U}_s^{(j)} \\ &+ \sum_{j=1}^{M_\omega}\sum_{s=1}^{N} \xi_s^{(j)}\Big(\frac{1}{2}{\boldsymbol{U}_s^{(j)}}^T\Big(2\frac{\partial \mathbf{A}}{\partial G_c}k_s^{(j)} + \frac{\partial \mathbf{B}}{\partial G_c}\Big)\boldsymbol{U}_s^{(j)}\Big)\Bigg\}\delta G_c \end{aligned} \tag{2.33}$$

Clearly, the true/target profile would enforce the vanishing of the control equation (2.33). The right-hand-side of (2.33), modulo the variation δG_c, represents the reduced gradient of the Lagrangian, since at any given inversion

iteration, the state and adjoint problems are satisfied. Thus, from (2.25), it follows that, at any inversion iteration, there holds:

$$\nabla \mathfrak{L} \;=\; \begin{bmatrix} 0 \\ 0 \\ \nabla_{G_c} \mathfrak{L} \end{bmatrix} \;, \tag{2.34}$$

where,

$$\begin{aligned} \nabla_{G_c} \mathfrak{L} = \Re e \Bigg\{ \sum_{j=1}^{M_\omega} \sum_{s=1}^{N} {\boldsymbol{\lambda}_s^{(j)}}^T \Big(\frac{\partial \mathbf{A}}{\partial G_c} {k_s^{(j)}}^2 + \frac{\partial \mathbf{B}}{\partial G_c} k_s^{(j)} + \frac{\partial \mathbf{G}}{\partial G_c} \Big) \boldsymbol{U}_s^{(j)} \\ + \sum_{j=1}^{M_\omega} \sum_{s=1}^{N} \xi_s^{(j)} \Big(\frac{1}{2} {\boldsymbol{U}_s^{(j)}}^T \Big(2 \frac{\partial \mathbf{A}}{\partial G_c} k_s^{(j)} + \frac{\partial \mathbf{B}}{\partial G_c} \Big) \boldsymbol{U}_s^{(j)} \Big) \Bigg\} \,. \end{aligned} \tag{2.35}$$

We use the reduced gradient $\nabla_{G_c} \mathfrak{L}$, as outlined below, to update the shear moduli during the inversion iterations.

2.4.2 The inversion process

To update/determine the shear moduli G_c, we use a gradient-based minimization scheme: starting with an assumed initial distribution for the moduli G_c, and a set of M_ω frequencies, we first solve the state problem (2.9) and (2.13), to obtain $k_s^{(j)}$ and $\boldsymbol{U}_s^{(j)}$. Next, using the wavenumbers $k_s^{(j)}$ and the eigenvectors $\boldsymbol{U}_s^{(j)}$, we compute the vertical displacement $\tilde{w}^{(j)}$ via (2.18), which, in turn, allows the computation of the misfit $\tilde{w}^{(j)} - \tilde{w}_m^{(j)}$ for every sensor for which measurements have been collected. Armed with the misfit and the state variables $(k_s^{(j)}, \boldsymbol{U}_s^{(j)})$, we then solve the adjoint problem (2.32) for each frequency set to obtain the adjoint variables $\boldsymbol{\lambda}_s^{(j)}$ and $\xi_s^{(j)}$. To update the

moduli G_c, we use a conjugate gradient approach [62], and to ensure sufficient decrease of the objective functional at each inversion iteration, we employ an Armijo backtracking line search. Accordingly: let $\boldsymbol{G}_k$ denote the vector of all element moduli G_c and let $\boldsymbol{g}_k = (\nabla_{\boldsymbol{G}} \mathfrak{L})_k$ denote the reduced gradient (2.35) of the Lagrangian at the k-th inversion iteration. Then, the update $\boldsymbol{G}_{k+1}$ to $\boldsymbol{G}_k$ is constructed via:

$$\boldsymbol{G}_{k+1} = \boldsymbol{G}_k + \alpha_k \boldsymbol{S}_k, \tag{2.36}$$

where α_k is a step length, and $\boldsymbol{S}_k$ denotes search direction, defined as:

$$\boldsymbol{S}_k = \begin{cases} -\boldsymbol{g}_k & , \text{for } k = 1 \\ -\boldsymbol{g}_k + \frac{\boldsymbol{g}_k \cdot \boldsymbol{g}_k}{\boldsymbol{g}_{k-1} \cdot \boldsymbol{g}_{k-1}} \boldsymbol{S}_{k-1} & , \text{for } k > 1 \end{cases} \tag{2.37}$$

The entire inversion process is summarized in Algorithm 1.

2.4.3 Frequency-continuation scheme

As discussed in the introduction, regularization is often used in inverse medium problems to filter out non-physical property distributions. In addition to regularizations, other optimizer-assisting schemes are also enlisted; here, we opt for one such scheme, over regularization. Specifically, we use a frequency-continuation scheme, which is consistent with field-deployable equipment capabilities. Accordingly: we probe the medium at a first set of $M_\omega^{(1)}$ frequencies, whose range is between ω_0 and ω_1, and invert for the properties using Algorithm 1. Once the inversion is concluded, we drive the inversion anew using

Algorithm 1 Shear moduli inversion scheme

Set iteration counter $k \leftarrow 1$
Set initial guess for shear moduli $\boldsymbol{G}$
Compute misfit $\mathfrak{F}$ ▷ Eq. (2.19)
Set convergence tolerance *tol*
Set maximum number of iterations *maxiter*
while $\mathfrak{F} > tol$ and $k < maxiter$ **do**
    Solve the state problem for $k_s^{(j)}$ and $\boldsymbol{U}_s^{(j)}$ ▷ Eqs. (2.9),(2.13)
    Solve the adjoint problem for $\boldsymbol{\lambda}_s^{(j)}$ and $\xi_s^{(j)}$ ▷ Eqs. (2.32)
    Compute the discrete reduced gradient $\boldsymbol{g}_k$ ▷ Eq. (2.35)
    Compute search direction $\boldsymbol{S}_k$ ▷ Eq. (2.37)
    Choose step length α_k
    Update material properties and compute $\boldsymbol{G}_{k+1}$ ▷ Eq. (2.36)
    Compute misfit $\mathfrak{F}$ ▷ Eq. (2.19)
    $k \leftarrow k + 1$
end while

a second set $M_\omega^{(2)}$ of frequencies within, now, the range (ω_0,ω_2) with $\omega_2 > \omega_1$, while using the previously converged profile as initial guess. We note that: a) the initial range (ω_0,ω_1) is a low-frequency range, aimed at recovering approximately the property profile, since probing with high-frequency content would lead to solutions diverging from the target, as is typically the case with this class of problems; b) the next set $M_\omega^{(2)}$ contains a few frequencies from $M_\omega^{(1)}$, but also includes higher frequencies, thus allowing refinement of the property profile and the potential discovery of small defects. A small number (5-10) of randomly selected frequencies in each of the probing M_ω sets is sufficient for convergence.

2.5 Numerical results

To highlight the dispersion-constrained inversion outlined in the previous section, we discuss next four cases of varying complexity, all based on synthetic data. We use (2.23) with one sensor for the first 3 cases, with the sensor placed at the center of the disc ($r = 0$), and then use (2.23) with 3 equally-spaced sensors for the last case study to demonstrate the capabilities of the process. The first case (case A) involves a typical heterogeneous layered soil medium with shear moduli monotonically increasing with depth. The second case (case B) pertains to a layered stratum with an interspersing soft layer between stiffer layers; and for the third case (case C), we consider a mixed target profile with a stiff but fairly thin layer at the top, which is the typical case for pavements. For the fourth numerical example, case A is revisited using a 3-sensor array. Finally, to study the performance of the proposed inversion process in the presence of noisy data, we revisit cases A and D while introducing 5% Gaussian noise to the sensor data. In all cases, to quantify the fitness of the inverted profile with respect to the target, we define the following normalized L_2 metric:

$$\mathcal{E} = \left[\frac{\int_0^{z_n} (G_e - G_c)^2 dz}{\int_0^{z_n} {G_e}^2 dz} \right]^{0.5}, \tag{2.38}$$

where G_e denotes the exact shear modulus profile. In all cases, the misfit tolerance *tol* in Algorithm 1 was set to 10^{-10} and the number of maximum inversion iterations *maxiter* was set to 2000.

2.5.1 Inversion with noise-free data

2.5.1.1 Case A: Layered stratum with monotonically increasing moduli

Consider a target layered medium comprising three layers with an overall depth of 2.5m, where each layer has larger shear modulus than the overlaying layer. The mass density ρ for all layers is set to 1800 kg/m^3. Poisson's ratio ν is 0.25 for all layers and, a very small damping $\beta = 0.001$ is used. The disc radius is set to $R = 15$cm. The target shear modulus, and the corresponding shear velocity c_s, profiles are:

$$G = \begin{cases} 150\,\text{MPa} & 0 \leq \text{z} \leq 1\,\text{m} \\ 250\,\text{MPa} & 1 \leq \text{z} \leq 1.7\,\text{m} \\ 350\,\text{MPa} & 1.7 \leq \text{z} \leq 2.5\,\text{m} \end{cases} \qquad c_s \approx \begin{cases} 289\,\text{m/s} & 0 \leq \text{z} \leq 1\,\text{m} \\ 373\,\text{m/s} & 1 \leq \text{z} \leq 1.7\,\text{m} \\ 441\,\text{m/s} & 1.7 \leq \text{z} \leq 2.5\,\text{m} \end{cases}$$

We use 25 quadratic elements to discretize the stratum's depth when inverting for the properties. To create the synthetic data, we use 52 quadratic elements. We note that the mesh used to generate the synthetic data conforms to the physical layer interfaces and consists of elements, which, for any given layer, must and do have identical properties. By contrast, the mesh used for the inversion consists of a different number of elements than those used for the synthetic data. Moreover, these elements do not necessarily conform to the physical layer interfaces, while the individual element properties are set to vary freely. The described meshing differences eliminate any potential biasing of the inversion.

Following the frequency-continuation scheme described earlier, we use four sets of ten randomly distributed frequencies within each set; the sets are [0,25] Hz, [0,50] Hz, [0,100] Hz and [0,150] Hz. We start the inversion with a homogeneous initial guess of 100MPa. Figure 2.4 shows the inverted profile at the end of the inversion process for each M_ω set. We note that the first set, which has a lower frequency content, constructs an approximate profile starting from a homogeneous initial guess, while the subsequent sets refine the profile as convergence to the target profile is attained. Figure 2.5 shows the reduction of misfit across all four frequency sets. For the first frequency set, we see a drop of about six orders of magnitude in the misfit, seven orders of magnitude for the second frequency set, three orders of magnitude for the third set, and about two orders of magnitude reduction in the fourth frequency set. As shown in Figure 2.5, each inversion process consists of 2000 iterations. The fitness metric after each frequency set is indicative of the progress toward convergence. Overall, the three layers and their interfaces have been satisfactorily recovered, and the final profile is quite close to the target ($\mathcal{E} = 6\%$).

2.5.1.2 Case B: Layered stratum with a soft layer trapped between stiffer layers

Next, we consider a three-layer stratum with ρ=1800 kg/m^3, ν=0.25, $\beta = 0.001$, of an overall depth of 2.5m, and the following shear modulus target profile and corresponding shear velocity c_s profile:

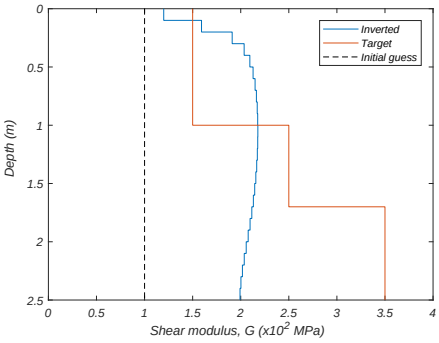

(a) Case A - after $M_\omega^{(1)}$, $\mathcal{E}$=35%

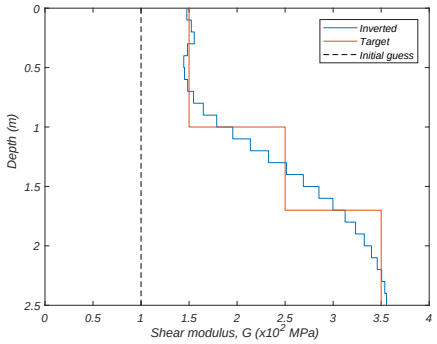

(b) Case A - after $M_\omega^{(2)}$, $\mathcal{E}$=8.5%

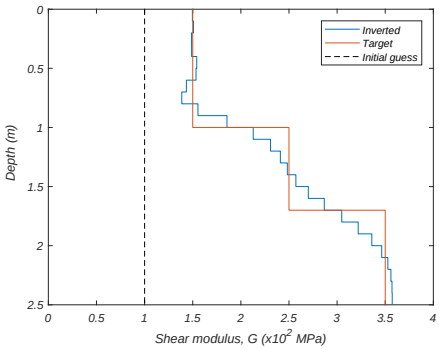

(c) Case A - after $M_\omega^{(3)}$, $\mathcal{E}$=7.1%

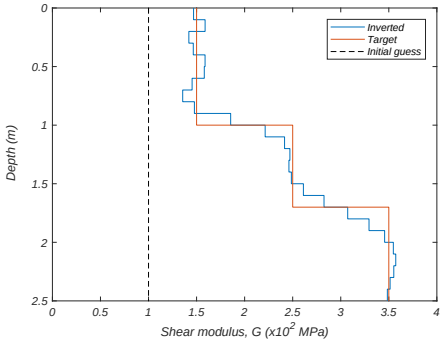

(d) Case A - after $M_\omega^{(4)}$, $\mathcal{E}$=6%

Figure 2.4: Case A: target and inverted shear modulus profiles shown at the end of the inversion process for each frequency set M_ω, with fitness metric $\mathcal{E}$

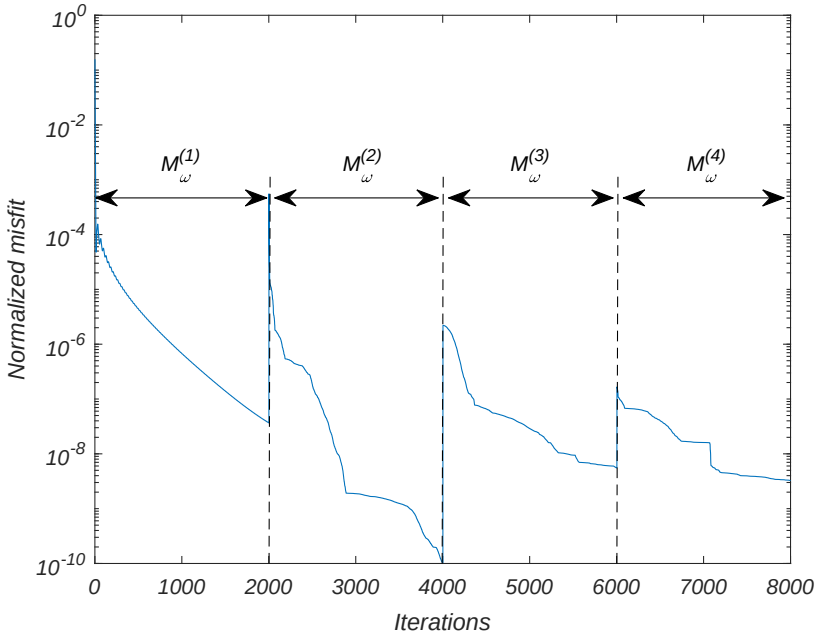

Figure 2.5: Case A - Misfit reduction for all frequency sets M_ω

$$G = \begin{cases} 200\,\text{MPa} & 0 \leq \text{z} \leq 1\,\text{m} \\ 150\,\text{MPa} & 1 \leq \text{z} \leq 1.5\,\text{m} \\ 250\,\text{MPa} & 1.5 \leq \text{z} \leq 2.5\,\text{m} \end{cases} \qquad c_s \approx \begin{cases} 333\,\text{m/s} & 0 \leq \text{z} \leq 1\,\text{m} \\ 289\,\text{m/s} & 1 \leq \text{z} \leq 1.5\,\text{m} \\ 373\,\text{m/s} & 1.5 \leq \text{z} \leq 2.5\,\text{m} \end{cases}$$

Again, we use 52 quadratic elements for the synthetic data, and 25 quadratic elements for the inversion, and the same frequency continuation scheme as in case A. We note that there is a thin layer at $1 \leq z \leq 1.5\,\text{m}$, which has a smaller shear modulus in comparison with the adjacent layers. Figure 2.6 shows the inverted profile at the end of the inversion process for each M_ω set. We note that the reconstruction is quite satisfactory even in this case where the presence of the soft layer tends to mask the deeper stratum structure, due to its trapped energy potential. The associated fitness metric was $\mathcal{E} = 4.8\%$.

2.5.1.3 Case C: A thin top layer - typical pavement structure

Next, we consider a medium comprising four layers, where the top layer is rather thin and stiff (a reasonable approximation for pavements). The target profile is:

$$G = \begin{cases} 1000\,MPa & 0 \leq z \leq 0.2\,m \\ 400\,MPa & 0.2 \leq z \leq 0.6\,m \\ 300\,MPa & 0.6 \leq z \leq 1\,m \\ 500\,MPa & 1 \leq z \leq 2\,m \end{cases} \qquad c_s \approx \begin{cases} 745\,m/s & 0 \leq z \leq 0.2\,m \\ 471\,m/s & 0.2 \leq z \leq 0.6\,m \\ 408\,m/s & 0.6 \leq z \leq 1\,m \\ 527\,m/s & 1 \leq z \leq 2\,m \end{cases}$$

We use, again, 52 quadratic elements for the synthetic data, and 25 quadratic elements for inversion. We use the same frequency continuation

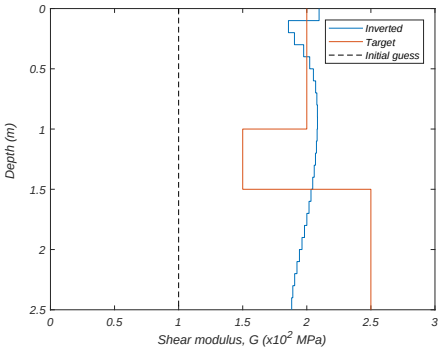

(a) Case B - after $M_\omega^{(1)}$, $\mathcal{E}$=20%

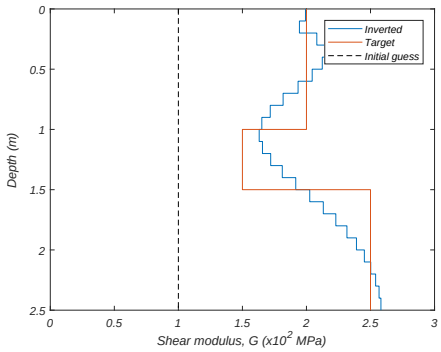

(b) Case B - after $M_\omega^{(2)}$, $\mathcal{E}$=10%

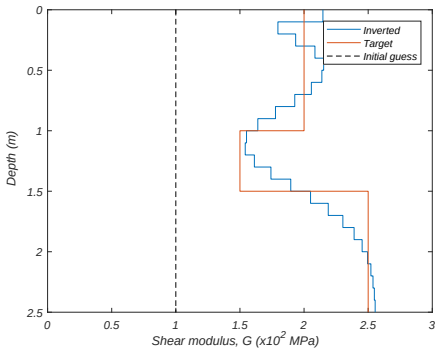

(c) Case B - after $M_\omega^{(3)}$, $\mathcal{E}$=8%

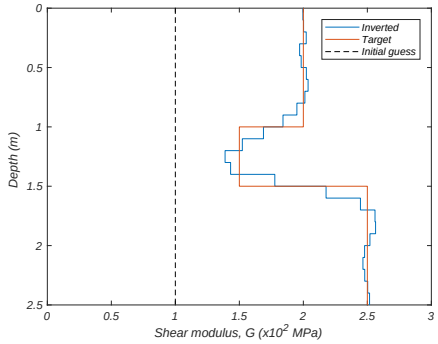

(d) Case B - after $M_\omega^{(4)}$, $\mathcal{E}$=4.8%

Figure 2.6: Case B: target and inverted shear modulus profiles shown at the end of the inversion process for each frequency set M_ω, with fitness metric $\mathcal{E}$

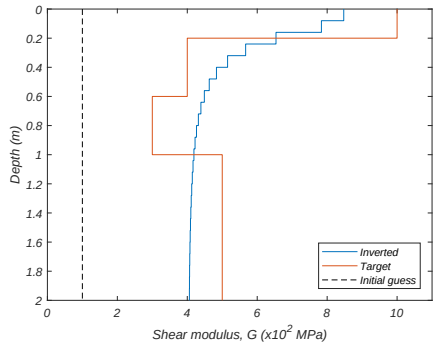

(a) Case C - after $M_\omega^{(1)}$, $\mathcal{E}$=24%

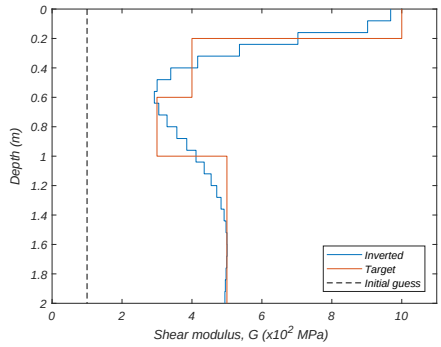

(b) Case C - after $M_\omega^{(2)}$, $\mathcal{E}$=15%

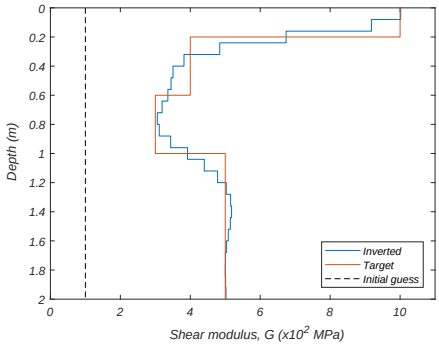

(c) Case C - after $M_\omega^{(3)}$, $\mathcal{E}$=9.4%

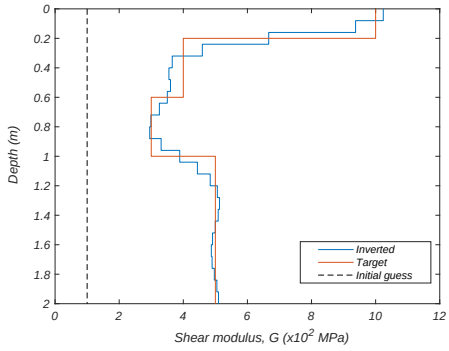

(d) Case C - after $M_\omega^{(4)}$, $\mathcal{E}$=6.2%

Figure 2.7: Case C: target and inverted shear modulus profiles shown at the end of the inversion process for each frequency set M_ω, with fitness metric $\mathcal{E}$

scheme as in the preceding cases. The inverted profiles for each frequency set are shown in Fig. 2.7.

Despite the thinness of the top layer, and the sharp contrast (jump) in the shear moduli between the top and second layers, the inversion process has again quite satisfactorily recovered the target, with a fitness of $\mathcal{E} = 6.2\%$.

2.5.1.4 Case D: Case A revisited with a 3-sensor array

We consider again case A, with the same profile and mesh properties as previously described. For the inversion process, we use (2.23) with $N_s = 3$ to solve the inverse medium problem: synthetically measured and computed displacements are recorded at 3 sensor locations, namely at $r = 0$, $r = 30$ cm and $r = 60$ cm. That is, the first sensor is under the load, whereas the other two are along the surface of the stratum. As in the preceding cases, the frequency-continuation scheme is used to drive the inversion with the same probing frequency sets as of case A. Figure 2.8 shows the inverted shear modulus profile. The result shows a good match between the inverted shear modulus profile and the target profile with the fitness metric $\mathcal{E} = 4.4\%$ –an improvement over the single sensor case ($\mathcal{E} = 6\%$).

2.5.2 Inversion with noisy data

Here, we apply 5% Gaussian noise to the synthetic sensor data used for cases A and D, and attempt to invert for the layer moduli. In each case, to generate the noisy data, we treated the synthetic complex displacements over all frequency sets as a (power) signal; we assumed a 5% background noise, and computed the signal-to-noise ratio (SNR$\simeq$ 13 dB). We fed the synthetic data and the SNR to Matlab's `awgn` function (Gaussian noise) to generate the noisy data. The resulting noisy displacement amplitudes varied between 0.05% and 4.4% of the unperturbed synthetic data.

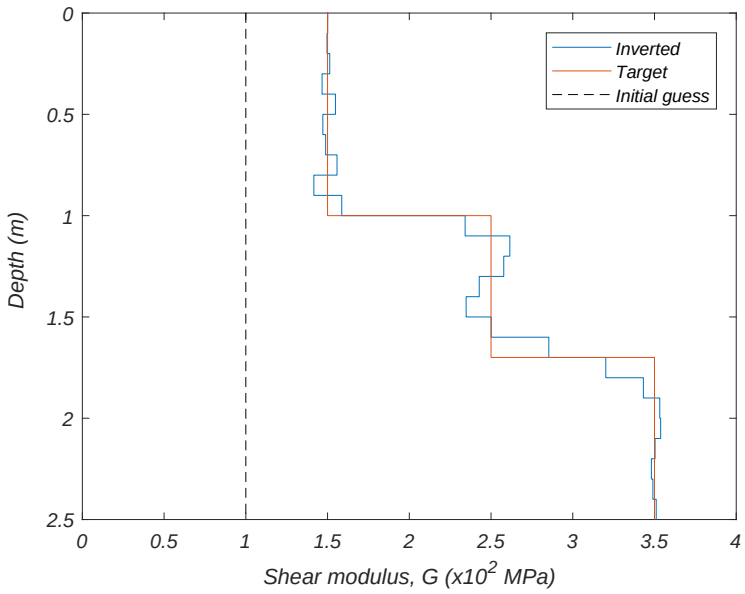

Figure 2.8: Case D: inverted shear modulus profile of case A with a 3-sensor array

2.5.2.1 Case E: Case A with noisy data

We consider case A with the same profile and mesh properties as used in case A. The same set of frequencies and frequency-continuation scheme are used for the inversion (Fig. 2.11). Similar to case A, the inverted shear modulus profile at the end of each frequency set and corresponding fitness metric is shown in Figure 2.9. Despite the increase in the fitness metric, the inverted profile represents the target profile satisfactorily. Three different layers are distinguishable and the shear modulus of each layer has been recovered. Comparing with case A, adding 5% noise to the data results in change of fitness metric from 6% to 9.6%. Figure 2.10 shows the reduction of the misfit through the inversion for each frequency set. Due to the applied noise, the reduction in the order of misfit at each frequency set is smaller than in case A (Fig. 2.5). Figure 2.11 shows the noisy sensor data for all frequencies used for the inversion. More interestingly, Fig. 2.11 depicts the frequency response curves one would obtain using the target profile, the profile inverted using noise-free data, and the profile inverted using noisy data. As it can be seen, all frequency response curves are fairly close. We note that the frequency response curve obtained for the noisy data case departs the most from the corresponding sensor data points, as also evidenced by the relatively large misfit values.

We note that, in the absence of regularization, the inversion process could yield non-physical profiles that match the data (noisy or noise-free). In Case E though, the inversion process resulted in a profile that matches closely the target, in the presence of noisy data and in the absence of regularization.

We note that a frequency response curve that would have closely matched the noisy data (with a misfit value similar to Case A), would have had to be fairly oscillatory in the low frequency regime. Such a frequency response would correspond to a profile that is not recoverable by the relatively coarse mesh we are using. Thus, we conjecture that, in effect, the coarseness of the mesh has, in this case, acted as a regularizer. In general, regularization would be required to alleviate solution multiplicity.

2.5.2.2 Case F: Case D with noisy data

Next, we consider case D with the same profile and mesh properties as earlier, i.e., we use 25 quadratic elements along the depth. Measured and computed displacements are recorded at 3 sensors: $r = 0$, $r = 30$ cm and $r = 60$ cm. The synthetically measured displacements are polluted with 5% Gaussian noise and then used for the inversion process. The inverted shear modulus profile is shown in Figure 2.12. Comparing with case D, the fitness metric has increased from 4.4% to 7% due to the added noise. Despite the noise, the inverted profile matches the target reasonably well. Comparing with case E, the use of three sensors, instead of one, has resulted in an improved fitness metric of 7% versus 9.6%.

2.6 Conclusion

We discussed a new dispersion-constrained optimization approach for resolving the inverse medium problem associated with the reconstruction of

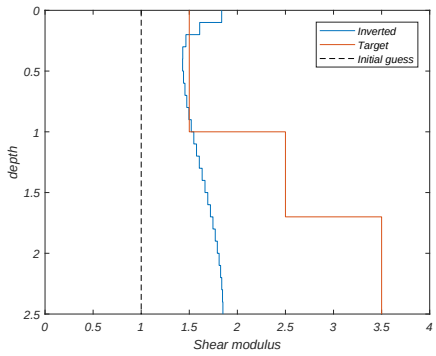

(a) Case E - after $M_\omega^{(1)}$, $\mathcal{E}$=41%

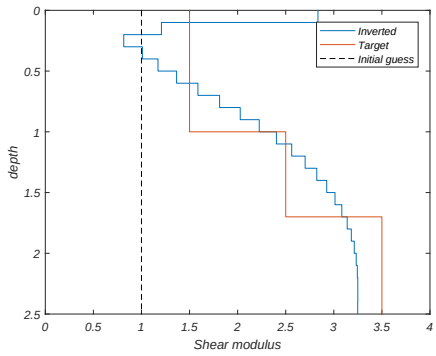

(b) Case E - after $M_\omega^{(2)}$, $\mathcal{E}$=17.6%

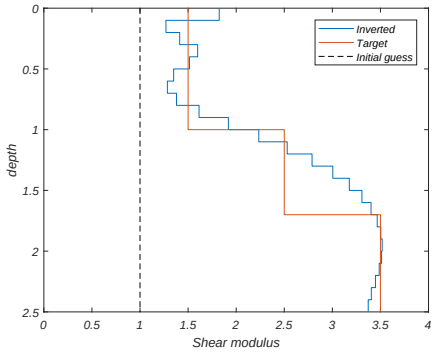

(c) Case E - after $M_\omega^{(3)}$, $\mathcal{E}$=13.1%

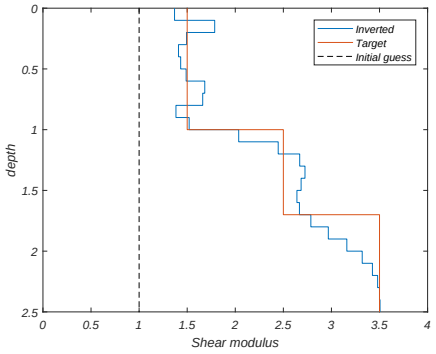

(d) Case E - after $M_\omega^{(4)}$, $\mathcal{E}$=9.6%

Figure 2.9: Case E: target and inverted shear modulus profiles shown at the end of the inversion process for each frequency set M_ω, with fitness metric $\mathcal{E}$ (noisy-data)

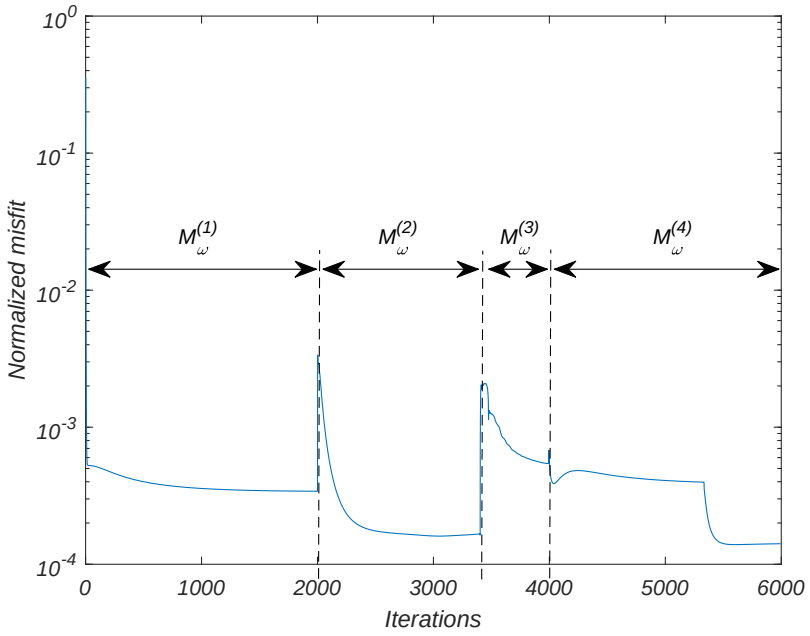

Figure 2.10: Case E - Misfit reduction for each frequency set M_ω

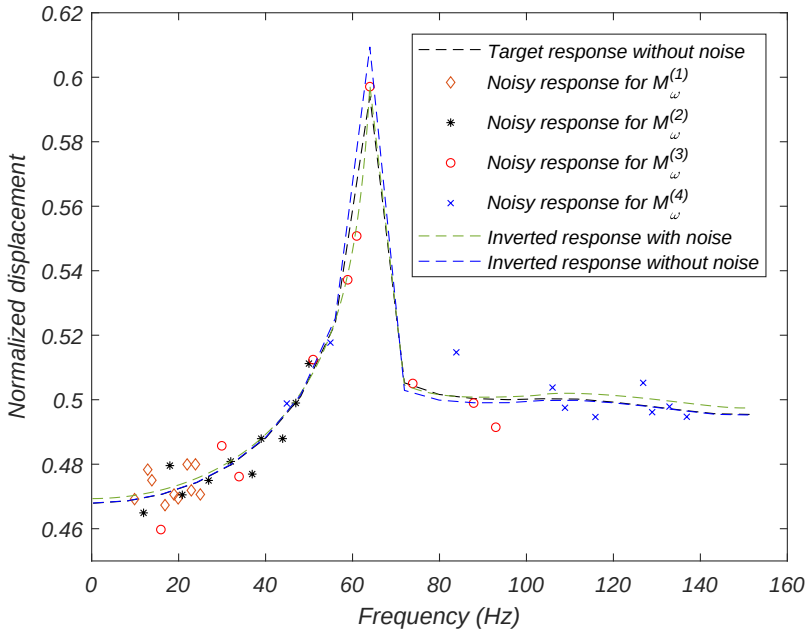

Figure 2.11: Frequency responses of the target profile for cases A and E, of the inverted profile with noise-free data and of the inverted profile with noisy data, along with the sensor data used for each frequency set

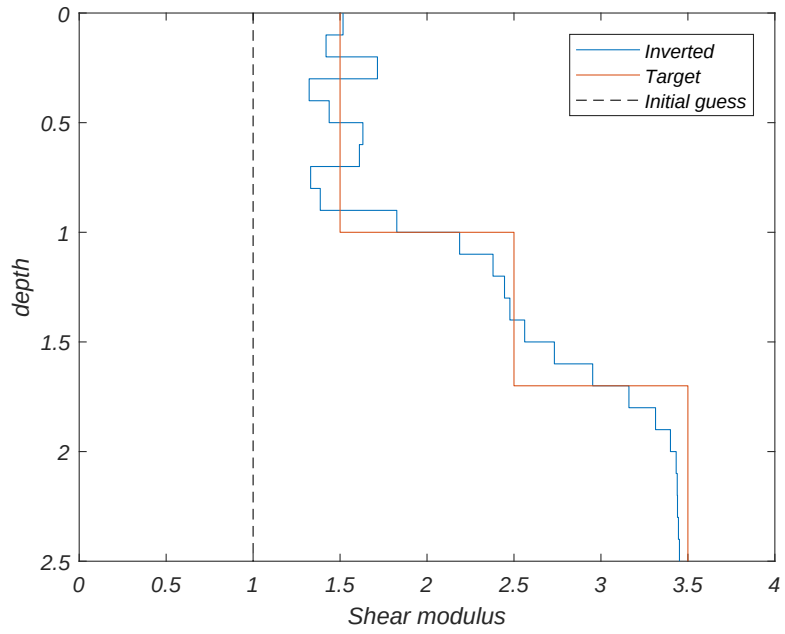

Figure 2.12: Case F: inverted shear modulus profile of case A with a 3-sensor array and 5% added noise

the material profile of a layered medium, based on surface measurements of its response to surface excitation. The methodology imposes the forward eigenvalue problem, provided by the thin-layer method, as a side constraint to a misfit functional to form the inversion problem's Lagrangian. This facilitates the iterations toward minimization of the misfit. Other key advantages of the methodology include: a) use is made of the complete recorded displacement waveforms, whether in the near-field or the far-field, without need for any simplifying assumptions; b) spatial discretization is needed only in one dimension. The methodology accommodates single or multiple sensor measurements, and takes advantage of the frequency agility of typical wave generating field equipment to embed, to advantage, a frequency-continuation scheme within the inversion problem.

The reported numerical results attest to the method's ability to invert for the moduli, and indirectly for the thicknesses, of a layered medium. Apart from demonstrating successful inversions of shear-modulus profiles using measurements from a single sensor, we have shown that increasing the number of sensors in the inversion process will lead to improvements in the inverted profiles. Therefore, the methodology is highly promising in applications to pavement testing where data from multiple sensors are routinely recorded. Furthermore, our computational experiments indicate that the methodology is capable of recovering the material parameters satisfactorily in the presence of noise in the recorded displacement data.

Chapter 3

Dispersion-constrained full-waveform inversion in a layered halfspace [1]

3.1 Introduction

The interest in the imaging of the near-surface deposits is driven by various infrastructure needs, including geotechnical site characterization, fault or sinkhole detection, pavement condition assessment, and others. Imaging requires the spatial resolution of the properties of the targeted deposits. To this end, the deposits are usually probed by waves generated by surface sources (either mechanical or electromagnetic), and the response of the medium to the probing is usually recorded in the time domain, at surface-deployed sensors. The recorded response is then used to characterize the deposits, thus giving rise to an inverse medium problem, endowed with some of the same complexities shared with deep-earth geophysical probing applications.

The spatial distribution of the near-surface deposits is often irregular, though not of a random or arbitrary nature. It is thus not uncommon to assume that a horizontally layered medium adequately describes the deposits –particularly true for engineered deposits (as is the case with, for example,

[1] Hamidreza Mashayekh, Loukas F. Kallivokas, John L. Tassoulas

pavements). The layered medium assumption represents a reasonable simplification, which, when justified by local site conditions, could accelerate preliminary investigations. This is the case of interest in this article: a rapid and robust methodology for the imaging of horizontally layered media resting on a halfspace using elastic waves for probing.

Difficulties with the field deployment of moving sources limit the probing loads to stationary, yet dynamic. The wave-generating surface load could be applied either through a plate in contact with the medium and driven by a signal generator (Vibroseis), or through hammering action, or by a weight falling from a prescribed height directly on the medium or on plate firmly affixed to the medium, etc. In most cases, it is possible to record the load in addition to the medium's response, which, in turn, could be recorded directly under the load, in the proximity of the load (near-field), or at the far-field.

To date, a handful of methods have been developed for the resolution of the spatial distribution of the properties (mechanical properties of the layers, layer thicknesses, and the halfspace properties); a review of methods, mostly from an engineering perspective, can be found in [33]. Despite the horizontal layering assumption, most existing methodologies require enlisting further simplifications to address the inversion: for example, in, so-called, backcalculation methods, the load, despite its dynamic nature, is assumed to be static [27, 48, 51, 71, 78]. In others (e.g. SASW, MASW), the surface recordings are treated as containing only portion of the propagating waveforms (the surface waves only) [30, 61, 68]. More recently, in an interesting departure from

the norm, in [7], the inversion was driven by a misfit between computed and experimentally-obtained phase velocities, with the latter though still generated by treating the field records as containing surface waves only.

Herein, we overcome the aforementioned limitations by accommodating the complete waveforms in the sensor data, by treating the load as dynamic, and without any other assumptions beyond the horizontal layering. Recent three-dimensional full-waveform inversion methodologies (e.g. [20–22]) could be applied, but the resulting complexity and computational cost is unwarranted in the presence of layering. However, the ideas propelled by PDE-constrained full-waveform inversion are still applicable: here, we tailor them to the layered medium case, albeit with a twist. Specifically, we use best-available methods for the solution of the forward problem: the Thin-Layer-Method for the resolution of the motion in the layered medium, and a Perfectly-Matched-Layer to model the halfspace. Following inverse medium lines, we define a misfit between computed and measured sensor data, and seek to minimize it. But, more importantly, we use the dispersion relation, as expressed by the associated eigenvalue problem, to constrain the minimization process, as we have recently done for the layered stratum case [55], thus departing from the PDE-as-a-constraint norm. The presence of the halfspace and its PML ersatz introduces complexities that merit specialized treatment, as will be discussed. In all, we show that the methodology reduces the problem to one spatial dimension, thereby allowing for the rapid characterization of the near-surface layered deposits in a robust manner. We report numerical results using both

noisy and noise-free data.

3.2 Problem definition/assumptions

Our goal is to characterize the layered subsurface in terms of the material properties of the layers, when the medium is subjected to a known dynamic surface disc load.

In general, there are several choices for describing the pair of elastic properties of each layer: the Lamé parameters, Young's modulus and Poisson's ratio, the bulk and shear moduli, the P- and S-wave velocities, the corresponding slownesses, etc. Irrespective of the choice for the elastic moduli pair, there are, in total, four material properties to invert for per layer: the elastic pair, mass density, and damping (for single-parameter attenuation models). Herein, of the four parameters per layer, we assume that three are *a priori* known and seek to invert only for the second Lamé parameter –the shear modulus. Whereas for pavements, where the mass density, Poisson's ratio, and damping may be reasonably well estimated, in the general case (e.g., site characterization) prior estimation of all three parameters cannot be justified. Nevertheless, here, we focus on a single distributed parameter inversion (the shear modulus) solely for the purpose of delineating the methodology. We note though that the approach remains the same, irrespective of the number of material parameters one seeks to invert for, and the method can be easily adapted to accommodate the additional material unknowns (we discuss later such an adaptation); however, it is noted that as the number of inversion parameters

is increased, it is expected that the ill-posedness of the inversion scheme will be exacerbated.

With these assumptions in mind, the shear moduli are unknown, but the first Lamé parameter λ is expressed in terms of the shear modulus G, i.e., $\lambda = \frac{2G\nu}{1-2\nu}$, where ν is Poisson's ratio (assumed known). Similarly, in the case of viscoelastic layers, G is replaced by its complex counterpart $G(1 + 2i\eta)$, where the damping factor η is also assumed known. We note that, following a successful inversion, the number of layers and their thicknesses will be indirectly determined, and, thus, neither the number of physical layers nor the layer thicknesses need be included explicitly as inversion parameters.

In common field applications, the driving load is typically dynamic, yet stationary, and the response of the medium is recorded at a few sensors situated under and at distance from the load (Fig. 3.1). Both the load and the sensor responses are recorded in the time domain. Here, we opt to work in the frequency domain, and assume that the time-domain records have been previously processed with a Fourier Transform. Consequently, we consider a harmonic load $P_0 e^{i\omega t}$ applied on a disc of radius R on the surface of a layered medium (Fig. 3.1).

The assumption of a layered subsurface, coupled with the axisymmetric character of the applied load, allows for the reduction of the spatial dimensionality of the problem at hand, as schematically depicted in the sequence of models shown in Fig. 3.2: from the originally three-dimensional problem (Fig. 3.2(a)), the layering assumption and the axisymmetric load lead to the

two-dimensional model depicted in Fig. 3.2(b), where the bottom-most layer (n-th layer) represents the halfspace and the spatial dependence extends over the radial direction (r) and the depth (z) only. Figure 3.2(c) depicts the associated computational model, where the originally semi-infinite n-th layer has been replaced by a finite-thickness n-th layer terminated by a buffer PML layer, also of finite thickness: the latter –the PML (Perfectly-Matched-Layer)– serves as an absorbing medium for outgoing waves, and is itself, as shown in Fig. 3.2(c), terminated at a fixed boundary.

While operating in the frequency domain, we also use a radial wavenumber expansion, or, equivalently, Hankel transforms in the radial direction, following the concepts of the Thin Layer Method (TLM) [40]: this results in the reduction of the two-dimensional problem depicted in Fig. 3.2(c) to a one-dimensional problem along only the depth direction (Fig. 3.2(d)).

Under the aforementioned assumptions, the full waveform inversion process reduces to the identification of the shear moduli of the one-dimensional discrete problem resulting from the discretization of the layered halfspace along the depth. We note that the number of inversion parameters equals the number of elements used for the discretization, since we assume a constant shear modulus per discrete element. Thus, the moduli of the physical layers are recoverable by synthesizing the discrete element moduli, upon successfully inverting for the element moduli.

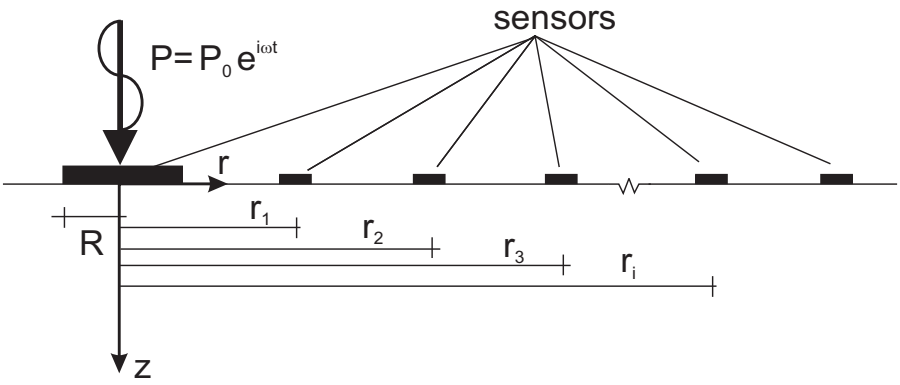

Figure 3.1: Typical field setup of a near-surface characterization application: stationary harmonic disc load and sensor locations

3.3 Full waveform inversion

3.3.1 Definition of the Lagrangian $\mathfrak{L}$

The typical starting point in full waveform inversion is the definition of the misfit functional, which is most often defined as the difference, in the least-squares sense, between the measured and computed responses. The measured responses are obtained from the recorded motion at select points on the medium's surface due to a stationary harmonic disc load applied on the surface (Fig. 3.1). The computed responses correspond to the response of the layered medium when the latter is described by a set of trial material properties. Accordingly, let the misfit functional $\mathfrak{F}$ be defined as:

$$\mathfrak{F} = \frac{1}{2} \sum_{i=1}^{N_s} \sum_{j=1}^{M_\omega} |d_i^{(j)}|^2 \,, \tag{3.1}$$

where $d_i^{(j)}$ is the misfit difference:

$$d_i^{(j)} = \tilde{w}^{(j)}(r_i, 0) - \tilde{w}_m^{(j)}(r_i, 0). \tag{3.2}$$

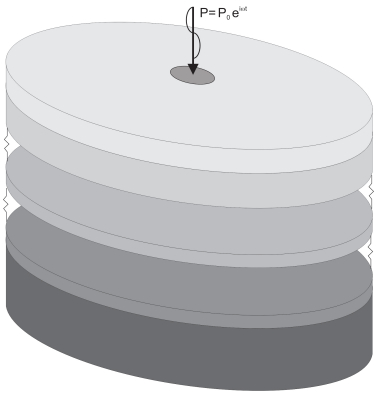

(a) 3D model of the physical problem in a semi-infinite domain

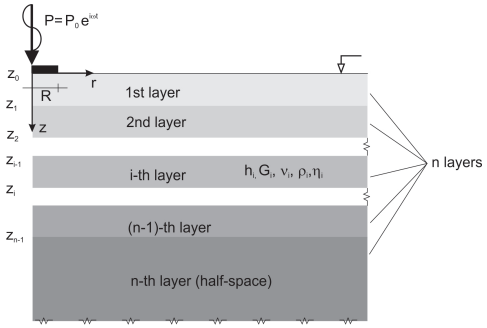

(b) 2D axisymmetric model in a semi-infinite domain

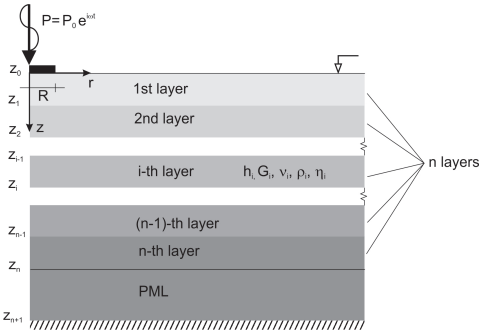

(c) 2D axisymmetric model in a PML-truncated domain

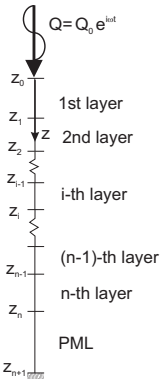

(d) 1D model after radial Hankel transform in a PML-truncated domain

Figure 3.2: Sequence of reduced-dimensionality models for a layered medium subjected to a stationary axisymmetric harmonic load

In (3.1), N_s is the number of sensors, M_ω is the number of discrete frequencies at which sensor measurements are recorded, $\tilde{w}^{(j)}(r_i, 0)$ represents the computed vertical displacement component of the layered medium at the j-th frequency ω_j on the surface ($z = 0$) and at distance r_i from the origin, and $\tilde{w}_m^{(j)}(r_i, 0)$ represents the measured displacement at the same point and for the same ω_j frequency. We note that the functional (3.1) accounts for both the real and imaginary parts of the response, or equivalently, it includes both amplitude and phase information.

Next, to construct the problem's Lagrangian $\mathfrak{L}$ we seek to side-impose to (3.1), as a constraint, a suitable mathematical description of the wave-induced motion in the layered halfspace. We denote the constraint as $\mathfrak{C}$; accordingly, the Lagrangian $\mathfrak{L}$ becomes:

$$\mathfrak{L} = \mathfrak{F} + \mathfrak{C} = \frac{1}{2} \sum_{i=1}^{N_s} \sum_{j=1}^{M_\omega} |d_i^{(j)}|^2 + \mathfrak{C}. \tag{3.3}$$

Candidate expressions for $\mathfrak{C}$ include the equations of elastodynamics in the frequency domain, in either a strong or a weak form, which, in turn, could be cast in either a continuous or discrete form. Given the spatial dimensionality reduction to 1D we are aiming for, which is afforded, as it will be shown, by the apparatus of the Thin Layer Method, the possible choices for describing $\mathfrak{C}$ reduce to either the one-dimensional problem depicted in Fig. 3.2(d), where the domain is subjected to the Hankel-transformed applied load Q_0, or the associated eigenvalue problem. Here, we opt for the latter: thus, we define $\mathfrak{C}$ as the inner product of the discrete eigenvalue problem and the Lagrange

multipliers used to side-impose the eigenvalue problem. Since the eigenvalue problem encompasses the dispersive properties of the medium, the inversion approach, by virtue of (3.3), is, in effect, dispersion-constrained. We describe next the technical details of $\mathfrak{C}$.

3.3.2 The side constraint $\mathfrak{C}$

To describe $\mathfrak{C}$, the discrete eigenvalue problem must be constructed first: the steps follow the sequence of models depicted in Fig. 3.2. The layered medium is modeled following the concepts of the Thin Layer Method [39, 40]. The halfspace is modeled via the introduction of a Perfectly-Matched-Layer (PML), attached to the n-th physical layer (Fig. 3.2); both the n-th layer and the PML share the same elastic moduli values. The PML too is treated with the Thin Layer Method, similarly to the n overlain layers of the interior domain [41].

3.3.2.1 Interior domain - the n physical layers

For any layer $i, i = 1, \ldots, n$ (Fig. 3.2(c)) of the interior domain, the equilibrium equations in cylindrical coordinates and in the frequency domain can be written as:

$$\frac{\partial \tilde{\sigma}_r}{\partial r} + \frac{\tilde{\sigma}_r - \tilde{\sigma}_\theta}{r} + \frac{\partial \tilde{\tau}_{rz}}{\partial z} = -\rho_i \omega^2 \tilde{u}, \tag{3.4a}$$

$$\frac{\partial \tilde{\tau}_{rz}}{\partial r} + \frac{\tilde{\tau}_{rz}}{r} + \frac{\partial \tilde{\sigma}_z}{\partial z} = -\rho_i \omega^2 \tilde{w}, \tag{3.4b}$$

where a tilde over the subtended variable denotes Fourier transform, and, otherwise, customary notation has been used; in particular, $\tilde{u}(r, z)$ and $\tilde{w}(r, z)$,

are the radial and vertical components of the displacement vector. Following [39], the displacement components $\tilde{u}$ and $\tilde{w}$ are Hankel-transformed, to yield:

$$u(z;k) = \mathcal{H}_1\{\tilde{u}(r,z)\},\ w(z;k) = \mathcal{H}_0\{\tilde{w}(r,z)\}, \tag{3.5}$$

where $\mathcal{H}_0$ and $\mathcal{H}_1$ denote the zeroth- and first-order Hankel transforms, respectively. Similarly, the stresses become:

$$\sigma_z(z;k) = \mathcal{H}_0\{\tilde{\sigma}_z(r,z)\} = \left[(\lambda + 2G)\frac{dw}{dz} + k\lambda u\right], \tag{3.6a}$$

$$\tau_{rz}(z;k) = \mathcal{H}_1\{\tilde{\tau}_{rz}(r,z)\} = G\left(\frac{du}{dz} - kw\right). \tag{3.6b}$$

Then, by taking into account the kinematic conditions and the constitutive law, the equations of motion for the i-th layer, written now in terms of u and w, reduce to:

$$-k^2(\lambda_i + 2G_i)u + G_i\frac{d^2u}{dz^2} - k(\lambda_i + G_i)\frac{dw}{dz} + \rho_i\omega^2 u = 0, \tag{3.7a}$$

$$-k^2 G_i w + (\lambda_i + 2G_i)\frac{d^2w}{dz^2} + k(\lambda_i + G_i)\frac{du}{dz} + \rho_i\omega^2 w = 0, \tag{3.7b}$$

where, λ_i and G_i are the i-th layer's first Lamé parameter and shear modulus, respectively. Next, using a standard Galerkin approach, the weak form of the

equations of motion becomes:

$$k^2(\lambda_i+2G_i)\int_{z_{i-1}}^{z_i} u\check{u}dz + k\Big[\lambda_i\int_{z_{i-1}}^{z_i}\frac{dw}{dz}\check{u}dz - G_i\int_{z_{i-1}}^{z_i} w\frac{d\check{u}}{dz}dz\Big] + G_i\int_{z_{i-1}}^{z_i}\frac{du}{dz}\frac{d\check{u}}{dz}dz - \rho_i\omega^2\int_{z_{i-1}}^{z_i} u\check{u}dz = G_i\Big[\frac{du}{dz}-kw\Big]\check{u}\Big|_{z_{i-1}}^{z_i} = \tau_{rz}\,\check{u}\Big|_{z_{i-1}}^{z_i}, \tag{3.8a}$$

$$k^2G_i\int_{z_{i-1}}^{z_i} w\check{w}dz - k\Big[G_i\int_{z_{i-1}}^{z_i}\frac{du}{dz}\check{w}dz - \lambda_i\int_{z_{i-1}}^{z_i} u\frac{d\check{w}}{dz}dz\Big] + (\lambda_i+2G_i)\int_{z_{i-1}}^{z_i}\frac{dw}{dz}\frac{d\check{w}}{dz}dz - \rho_i\omega^2\int_{z_{i-1}}^{z_i} w\check{w}dz = \Big[(\lambda_i+2G_i)\frac{dw}{dz}+k\lambda_i u\Big]\check{w}\Big|_{z_{i-1}}^{z_i} = \sigma_z\,\check{w}\Big|_{z_{i-1}}^{z_i}, \tag{3.8b}$$

where $\check{u}$ and $\check{w}$ are admissible test functions.

3.3.2.2 The Perfectly-Matched-Layer (PML)

To account for the halfspace, we introduce a PML buffer of L_{PML} thickness, attached to the bottom n-th layer, and terminated at a fixed boundary (Fig. 3.3). In the PML, the physical coordinate z is mapped onto a complex-stretched $\tilde{z}$; we use the standard stretching function for the $z\to\tilde{z}$ map [41, 43]: Accordingly:

$$\tilde{z} = \int_{z_n}^{z}\varepsilon_z(z',\omega)dz', \tag{3.9}$$

with

$$\varepsilon_z(z,\omega) = \alpha(z) + \frac{1}{i\omega}\beta(z),\ z_n\le z\le z_{n+1},\ \text{ and} \tag{3.10a}$$

$$\alpha(z) = 1+\alpha_0\Big[\frac{z-z_n}{L_{\text{PML}}}\Big]^m,\ \beta(z) = \beta_0\Big[\frac{z-z_n}{L_{\text{PML}}}\Big]^m. \tag{3.10b}$$

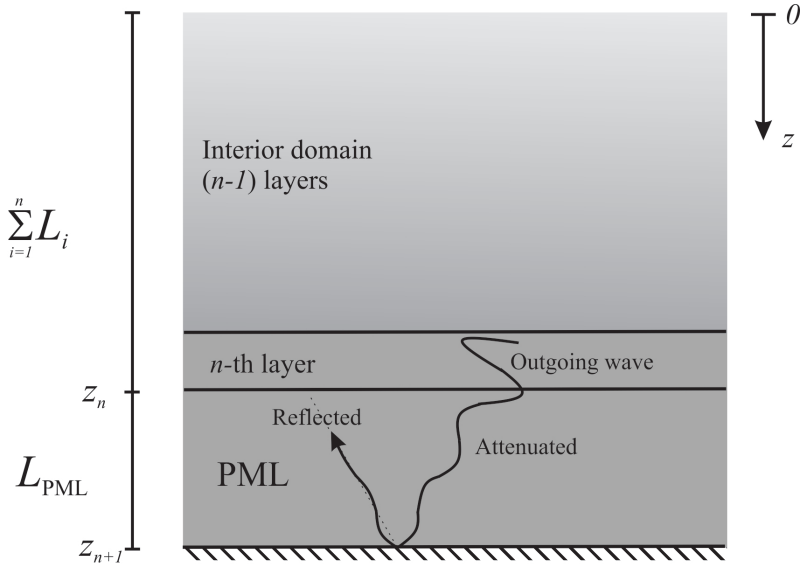

Figure 3.3: Layered medium terminated with a PML buffer

Using the above, we then complex-stretch the equilibrium equations (3.4), which for the PML result in:

$$\frac{\partial \tilde{\sigma}_r}{\partial r} + \frac{\tilde{\sigma}_r - \tilde{\sigma}_\theta}{r} + \frac{1}{\varepsilon_z}\frac{\partial \tilde{\tau}_{rz}}{\partial z} = -\rho_{\mathrm{PML}}\omega^2 \tilde{u}, \tag{3.11a}$$

$$\frac{\partial \tilde{\tau}_{rz}}{\partial r} + \frac{\tilde{\tau}_{rz}}{r} + \frac{1}{\varepsilon_z}\frac{\partial \tilde{\sigma}_z}{\partial z} = -\rho_{\mathrm{PML}}\omega^2 \tilde{w}. \tag{3.11b}$$

By substituting (3.5) and (3.6) into (3.11), while again taking into account the kinematic conditions and the constitutive law, yields the strong form of the

PML equations of motion:

$$
\begin{aligned}
&- \varepsilon_z k^2(\lambda_{\mathrm{PML}} + 2G_{\mathrm{PML}})u + \frac{1}{\varepsilon_z} G_{\mathrm{PML}} \frac{d^2u}{dz^2} \\
&- k(\lambda_{\mathrm{PML}} + G_{\mathrm{PML}}) \frac{dw}{dz} + \varepsilon_z \rho_{\mathrm{PML}} \omega^2 u = 0, \qquad (3.12a) \\
&- \varepsilon_z k^2 G_{\mathrm{PML}} w + \frac{1}{\varepsilon_z}(\lambda_{\mathrm{PML}} + 2G_{\mathrm{PML}}) \frac{d^2w}{dz^2} \\
&+ k(\lambda_{\mathrm{PML}} + G_{\mathrm{PML}}) \frac{du}{dz} + \varepsilon_z \rho_{\mathrm{PML}} \omega^2 w = 0. \qquad (3.12b)
\end{aligned}
$$

Equations (3.12) can then be cast in a weak form:

$$
\begin{aligned}
&k^2(\lambda_{\mathrm{PML}} + 2G_{\mathrm{PML}}) \int_{z_n}^{z_{n+1}} \varepsilon_z u \check{u} dz \\
&+ k\left[\lambda_{\mathrm{PML}} \int_{z_n}^{z_{n+1}} \frac{dw}{dz} \check{u} dz - G_{\mathrm{PML}} \int_{z_n}^{z_{n+1}} w \frac{d\check{u}}{dz} dz\right] \\
&+ G_{\mathrm{PML}} \int_{z_n}^{z_{n+1}} \frac{1}{\varepsilon_z} \frac{du}{dz} \frac{d\check{u}}{dz} dz - \rho_{\mathrm{PML}} \omega^2 \int_{z_n}^{z_{n+1}} \varepsilon_z u \check{u} dz \\
&= G_{\mathrm{PML}}\left[\frac{1}{\varepsilon_z} \frac{du}{dz} - kw\right] \check{u} \Big|_{z_n}^{z_{n+1}} = \tau_{rz}\, \check{u} \Big|_{z_n}^{z_{n+1}} \qquad (3.13a)
\end{aligned}
$$

$$
\begin{aligned}
&k^2 G_{\mathrm{PML}} \int_{z_n}^{z_{n+1}} \varepsilon_z w \check{w} dz \\
&- k\left[G_{\mathrm{PML}} \int_{z_n}^{z_{n+1}} \frac{du}{dz} \check{w} dz - \lambda_{\mathrm{PML}} \int_{z_n}^{z_{n+1}} u \frac{d\check{w}}{dz} dz\right] \\
&+ (\lambda_{\mathrm{PML}} + 2G_{\mathrm{PML}}) \int_{z_n}^{z_{n+1}} \frac{1}{\varepsilon_z} \frac{dw}{dz} \frac{d\check{w}}{dz} dz \\
&- \rho_{\mathrm{PML}} \omega^2 \int_{z_n}^{z_{n+1}} \varepsilon_z w \check{w} dz \\
&= \left[(\lambda_{\mathrm{PML}} + 2G_{\mathrm{PML}}) \frac{1}{\varepsilon_z} \frac{dw}{dz} + k\lambda_{\mathrm{PML}} u\right] \check{w} \Big|_{z_n}^{z_{n+1}} \\
&= \sigma_z\, \check{w} \Big|_{z_n}^{z_{n+1}} \qquad (3.13b)
\end{aligned}
$$

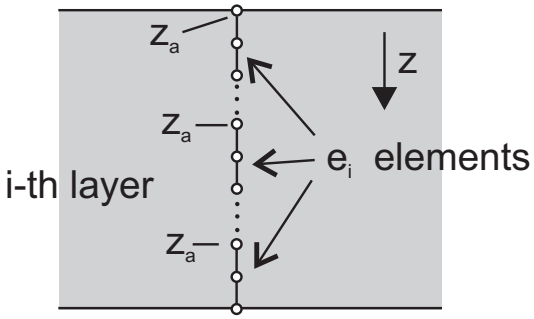

Figure 3.4: i-th layer discretization into e_i elements.

Thus, the solution for the surface-loaded domain problem shown in Fig. 3.2(d), in terms of the radial and vertical displacement components $u(z;k)$ and $w(z;k)$, respectively, can be obtained by the solution of weak forms (3.8) and (3.13), subject to fixed conditions ($u = w = 0$) at z_{n+1} (Fig. 3.2(d)), the continuity of displacements and tractions along the layer interfaces $z_i, i = 1,\ldots,n$, and to the surface conditions:

$$\sigma_z(z=0;k) = \mathcal{H}_0\{\tilde{\sigma}_z(z=0,r)\} = \mathcal{H}_0\left\{\frac{P_0}{\pi R^2}\right\} = P_0\frac{J_1(kR)}{\pi kR} \equiv Q_0, \quad (3.14a)$$

$$\tau_{rz}(z=0;k) = 0. \quad (3.14b)$$

Conversely, the associated eigenvalue problem can be similarly obtained, while enforcing traction-free conditions on the surface ($\sigma_z = \tau_{rz} = 0$) in lieu of (3.14).

3.3.2.3 The discrete eigenvalue problem

Each physical layer i in the interior domain is discretized into e_i elements (Fig. 3.4), while the PML is discretized into e_{PML} elements. Standard Lagrange shape functions are then used to approximate the displacement components of the trial pair (u, w) and of the test pair $(\breve{u}, \breve{w})$. Thus, within each

layer (interior and PML):

$$u(z) = \boldsymbol{\phi}^T(z)\,\boldsymbol{u}, \quad w(z) = \boldsymbol{\phi}^T(z)\,\boldsymbol{w}, \tag{3.15}$$

where, $\boldsymbol{\phi}$ are vectors of shape functions, and

$$\boldsymbol{u} = \begin{bmatrix} \boldsymbol{u}_{\text{int}} \\ \boldsymbol{u}_{\text{PML}} \end{bmatrix}, \quad \boldsymbol{w} = \begin{bmatrix} \boldsymbol{w}_{\text{int}} \\ \boldsymbol{w}_{\text{PML}} \end{bmatrix}, \tag{3.16}$$

are vectors of the nodal values of the radial and vertical displacement components, respectively. If, for example, the element shape functions are of polynomial degree d, then the vector $\boldsymbol{\phi}(z)$ has dimension $e_i d + 1$ for layers in the interior domain, and $e_{\text{PML}} - 1$ for the PML (discretization details are provided in Appendix 3.A). Next, we focus on the eigenvalue problem: inserting the approximations (3.15) into the weak forms (3.8) and (3.13) for the trial pair (and similarly for the test pair), gives rise to the following quadratic eigenvalue problem in terms of the wavenumber k:

$$(k^2\mathbf{A} + k\mathbf{B} + \mathbf{G} - \omega^2\mathbf{M})\boldsymbol{U} = \mathbf{0}\ ;\ \boldsymbol{U} = \begin{bmatrix} \boldsymbol{u} \\ \boldsymbol{w} \end{bmatrix} = \begin{bmatrix} \boldsymbol{u}_{\text{int}} \\ \boldsymbol{u}_{\text{PML}} \\ \boldsymbol{w}_{\text{int}} \\ \boldsymbol{w}_{\text{PML}} \end{bmatrix}, \tag{3.17}$$

where, $\boldsymbol{U}$ denotes eigenvectors. The details of matrices $\mathbf{A}$, $\mathbf{B}$, $\mathbf{G}$ and $\mathbf{M}$ are given in Appendix 3.B.

The quadratic eigenvalue problem (3.17) admits $2N$ eigenvalues (the, generally complex, wavenumbers k), and $2N$ eigenvectors (modes), where N represents the total number of degrees of freedom, defined as:

$$N = 2d\left(\sum_{i=1}^{n} e_i + e_{\text{PML}}\right). \tag{3.18}$$

For each complex wavenumber k, $-k$ also represents an eigenvalue, and, thus, the $2N$ wavenumbers are obtained as N pairs in the form $(k, -k)$. Not all of the wavenumbers lead to admissible displacement solutions, and thus, a selection process must be devised to filter out the undesirable/problematic modes. Such a mode selection process is straightforward in the case of a stratum (layered medium terminated at a fixed boundary); however, in the presence of the PML, the process becomes more challenging and merits a detailed discussion (see section 3.3.2.4). For the moment, and without loss of generality, we will assume that there are N modes that survive the selection process. Then, the N surviving eigenvectors are normalized similarly to Kausel [39] and Waas [79]:

$$\frac{1}{2}\boldsymbol{U}_s^T(2k_s\mathbf{A}+\mathbf{B})\boldsymbol{U}_s = k_s, \qquad s = 1, 2, ..., N, \tag{3.19}$$

where the subscript s denotes the s-th mode. We use the discrete eigenvalue problem (3.17), and the orthonormality condition (3.19) to define the side constraint $\mathfrak{C}$ as:

$$\begin{aligned}\mathfrak{C} = \Re e \Bigg\{ \sum_{j=1}^{M_\omega}\sum_{s=1}^{N} {\boldsymbol{\chi}_s^{(j)}}^T \left[\ {k_s^{(j)}}^2\mathbf{A}^{(j)} + k_s^{(j)}\mathbf{B} + \mathbf{G}^{(j)}\ -{\omega_j}^2\mathbf{M}^{(j)}\right]\boldsymbol{U}_s^{(j)} + \\ \sum_{j=1}^{M_\omega}\sum_{s=1}^{N}\xi_s^{(j)}\left(\frac{1}{2}{\boldsymbol{U}_s^{(j)}}^T(2k_s^{(j)}\mathbf{A}^{(j)}+\mathbf{B})\boldsymbol{U}_s^{(j)} - k_s^{(j)}\right)\Bigg\},\end{aligned} \tag{3.20}$$

where $\boldsymbol{\chi}_s^{(j)}$ is a vector of Lagrange multipliers used to side-impose the eigenvalue problem (3.17) for each mode, and $\xi_s^{(j)}$ is a scalar Lagrange multiplier used for the side-imposition of the orthonormality condition (3.19). It should be noted that, due to the presence of the stretching function ε_z inside matrices $\mathbf{A}$, $\mathbf{G}$ and $\mathbf{M}$, the superscript (j) is used to indicate that they are frequency-dependent.

Given the definition (3.20) of the constraint $\mathfrak{C}$, in order to complete the definition of the Lagrangian (3.3), the computed vertical displacement components $\tilde{w}^{(j)}(r,0)$ must also be computed for each ω_j frequency; accordingly, per [39]:

$$\tilde{w}^{(j)}(r,0) = \frac{P_0}{\pi R}\sum_{s=1}^{N}(U^{(j)}_{s,\frac{N}{2}+1})^2 I^{(j)}_{1s}(r), \tag{3.21}$$

where

$$I^{(j)}_{1s}(r) = \begin{cases} \dfrac{\pi}{2\boldsymbol{i}k_s^{(j)}} J_0(k_s^{(j)}r)H_1^{(2)}(k_s^{(j)}R) - & \dfrac{1}{Rk_s^{(j)^2}}, \\ & 0 \le r \le R \\ \dfrac{\pi}{2\boldsymbol{i}k_s^{(j)}} J_1(k_s^{(j)}R)H_0^{(2)}(k_s^{(j)}r), & R \le r \end{cases} \tag{3.22}$$

where, $H_0^{(2)}$, and $H_1^{(2)}$ denote Hankel functions of the second kind and of zeroth and first order, respectively, and J_0 denotes the Bessel function of zeroth order. Introducing (3.21) and (3.22) into (3.3) yields:

$$\mathfrak{L} = \begin{cases} \frac{1}{2}\displaystyle\sum_{j=1}^{M_\omega}\sum_{i=1}^{N_s}\left|\frac{P_0}{\pi R}\sum_{s=1}^{N}\left[(U^{(j)}_{s,\frac{N}{2}+1})^2\frac{\pi}{2\boldsymbol{i}k_s^{(j)}}\right.\right. & \left. J_0(k_s^{(j)}r_i)H_1^{(2)}(k_s^{(j)}R) - \dfrac{1}{Rk_s^{(j)^2}}\right] \\ & \left. -\tilde{w}_m^{(j)}(r_i,0)\right|^2 + \mathfrak{C}, \quad 0 \le r_i \le R \\ \dfrac{1}{2}\displaystyle\sum_{j=1}^{M_\omega}\sum_{i=1}^{N_s}\left|\frac{P_0}{\pi R}\sum_{s=1}^{N}\left[(U^{(j)}_{s,\frac{N}{2}+1})^2\frac{\pi}{2\boldsymbol{i}k_s^{(j)}}\right.\right. & \left. J_1(k_s^{(j)}R)H_0^{(2)}(k_s^{(j)}r_i)\right] \\ & \left. -\tilde{w}_m^{(j)}(r_i,0)\right|^2 + \mathfrak{C}, \quad R \le r_i \end{cases} \tag{3.23}$$

The Lagrangian (3.23) is the basis for the full waveform inversion methodology.

3.3.2.4 Mode selection

In the case of a layered stratum (fixed base), the selection process for the set of admissible wavenumbers is straightforward, especially in the presence of a small amount of material damping [55]. As it can be deduced from (3.22), owing to the presence of $H_0^{(2)}$ (which is also present in the stratum case), the asymptotic behavior for large radial distances and for each mode is proportional to $e^{-ik_s^{(j)}r}$, and therefore, the wavenumbers with positive imaginary part ($\Im m(k_s^{(j)}) > 0$) correspond to modes that grow exponentially away from the origin, thus violating the boundedness condition. Consequently, only half of the wavenumbers are physically acceptable, i.e., from each pair $(k_s^{(j)}, -k_s^{(j)})$, only the wavenumbers with negative imaginary part ($\Im m(k_s^{(j)}) < 0$) should be retained [39, 55]. Figure 3.5 depicts a typical distribution of wavenumbers on the complex plane for a fixed (real) frequency and for the stratum problem: in this case, only the wavenumbers in the lower halfplane will be retained.

The question then becomes whether the selection process used for the stratum can also be used for the layered medium over halfspace, where the halfspace has been replaced/modeled by a PML. The PML is, primarily, a mathematical construct, with no physical analog (it is not a proper viscoelastic medium). The introduction of a PML alters the spectral properties of the combined medium (physical layers+PML), resulting in problematic (some non-physical) modes. Consider, for example, the case of a single layer over a PML buffer, with the parameters shown in Fig. 3.6(a): Figure 3.6(b) shows the distribution of radial wavenumbers for this case. If, out of all eigenval-

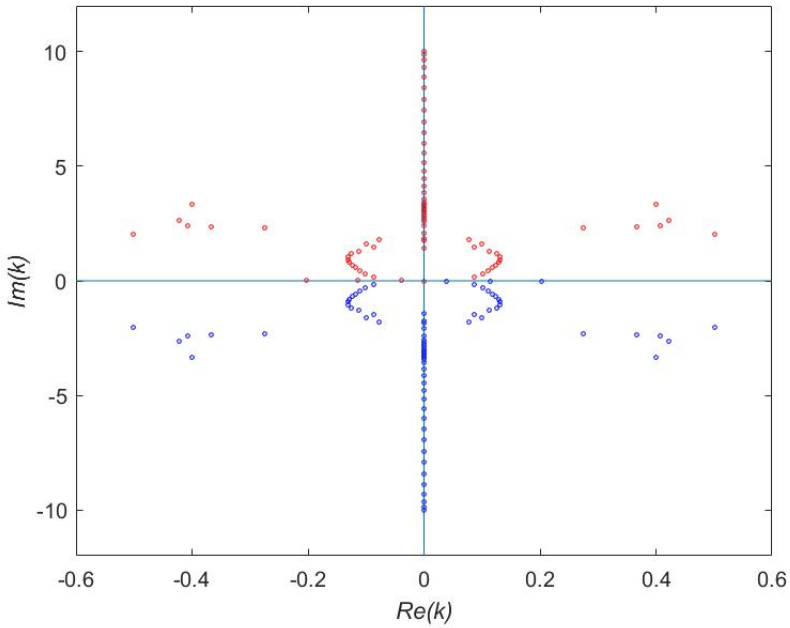

Figure 3.5: Typical distribution of wavenumbers for a layered stratum at a fixed frequency ω_j

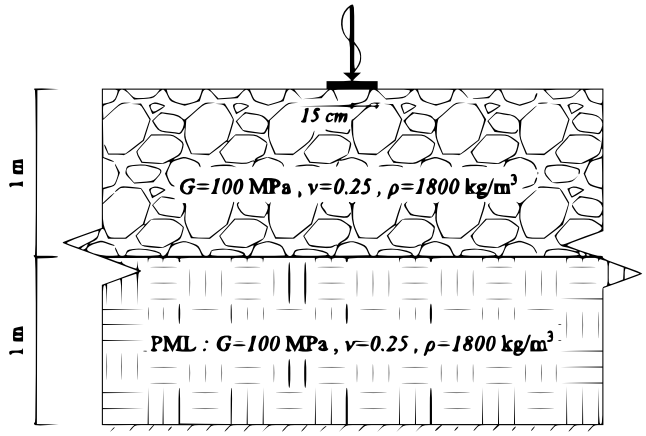

(a) A layer over PML

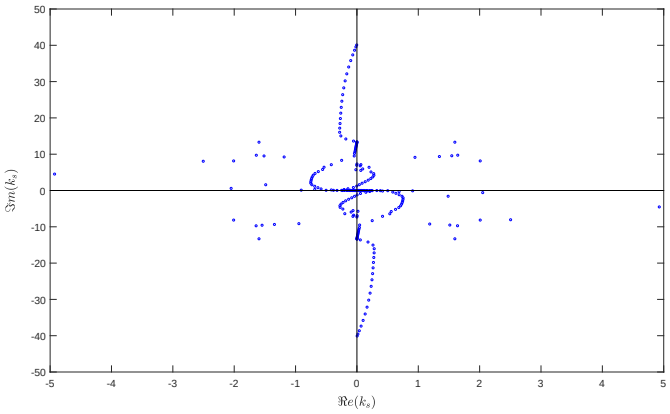

(b) Wavenumber distribution

Figure 3.6: Typical distribution of wavenumbers for a layer over PML at a fixed frequency ω_j

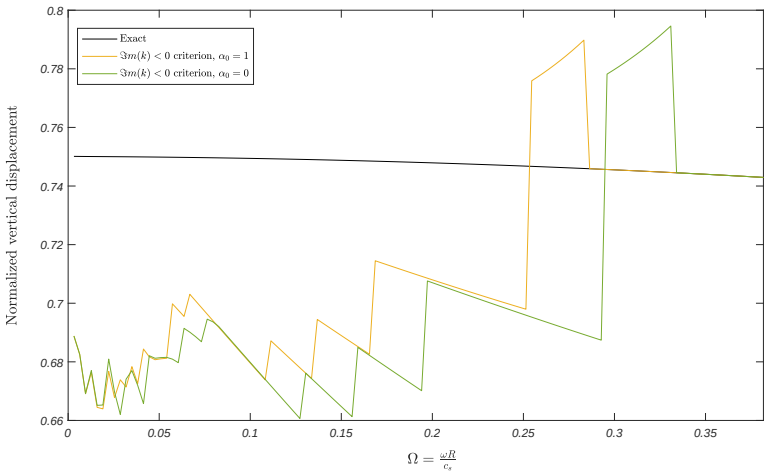

Figure 3.7: Normalized vertical displacement under the center of the disc load as a function of normalized frequency for a layer over PML

ues/wavenumbers generated by the solution to the eigenvalue problem, one were to retain the wavenumbers that satisfy the ($\Im m(k_s^{(j)}) < 0$), and use the associated modes to construct the displacement response per (3.21), the vertical displacement under the load ($r = 0$) would exhibit the erratic pattern depicted in Fig. 3.7. Two of the three depicted curves correspond to solutions obtained using two different values for the PML parameter α_0: the $\alpha_0 = 0$ corresponds to a particular implementation of the PML and TLM that first appeared in [17], which forces a constant real part for the stretching function ε_z, whereas the $\alpha_0 = 1$ allows for a varying $\alpha(z)$ (3.10a), and thus for a varying real part for the PML stretching function ε_z. The benefit of the latter is, primarily, the user-controlled attenuation of evanescent modes in the PML. Nevertheless, as it can be seen in Fig. 3.7, irrespective of the α_0 value,

the response is wrong; it can be further seen that beyond a certain frequency ($\Omega = 0.333$), the three curves coincide. This is due to the fact that, for higher frequencies, modes that, for lower frequencies, were previously excluded by the $\Im m(k_s^{(j)}) < 0$ criterion, have rotated out of the first to the fourth quadrant, thus now satisfying the criterion. In other words, it appears that the criterion excludes modes that have a beneficial effect to the response (must be included), despite the fact that their inclusion would violate the boundedness condition.

To better understand the role of the modes to the response, we compute next the modal total energy flux E_s across the curved surface of the cylinder at an arbitrary distance r_0 from the origin ($r_0 > R$). The total energy flux is the rate at which energy is transferred, during one cycle, through the surface, without normalization with respect to the area. As it is shown in Appendix 3.C, E_s is given as:

$$E_s = -\pi\omega r_0 \Im m\Big\{\bar{\boldsymbol{U}}_s^T \mathbf{H}_s(k_s\mathbf{A}_e + \mathbf{D}_e)\boldsymbol{U}_s\Big\}, \tag{3.24}$$

The sign of (3.24) determines whether the energy is outgoing ($E_s > 0$), or incoming ($E_s < 0$). We remark that E_s is computed over the curved surface of both the interior domain and the PML buffer. Whereas for the interior domain there is physical meaning to E_s, there is no physical meaning that can be ascribed to the E_s quantity defined over the PML. Numerically, the PML contribution to E_s is leaving its sign unaltered for all r_0; moreover, the sign remains the same, irrespective of the r_0 value, that is, the flux is either

outgoing or incoming at any r_0. Thus, for practical computations one can use either (3.24) or the reduced expression (3.51).

Using (3.24), we filter the wavenumbers by retaining only those with positive outgoing energy: for the interior domain, the sign of the flux also indicates the sign of the group velocity, and thus, another way of considering the filtering is that we retain wavenumbers for which both the phase and the group velocity are outgoing. Under the new filtering criterion, the distribution of wavenumbers is plotted again in Fig. 3.8, where the red circles indicate wavenumbers with incoming energy (and thus rejectable), and the blue circles indicate wavenumbers with outgoing energy. A cursory look at Fig. 3.8(a) would suggest that the rejected wavenumbers are the same as those rejected by the $\Im m(k_s^{(j)})$ criterion, but as the insert of Fig. 3.8(b) clearly shows, there are wavenumbers with outgoing energy (blue circles in the first quadrant, and thus retainable), which would have been rejected with the previous criterion ($\Im m(k_s^{(j)})$). We note that: a) only a few of the first quadrant wavenumbers are retained by the energy criterion; however, those retained violate the boundedness condition, and they ought not to be used for calculations in the far field; b) for the stratum case, the two criteria (energy-based and imaginary-part-based) return the same set of acceptable wavenumbers. To show the effect the set of wavenumbers that is now retained by the energy criterion has on the response, Fig. 3.9 depicts seven curves for the normalized vertical component of the displacement at the center of the load. It can be seen that only the responses rendered with the aid of the energy criterion produce the correct be-

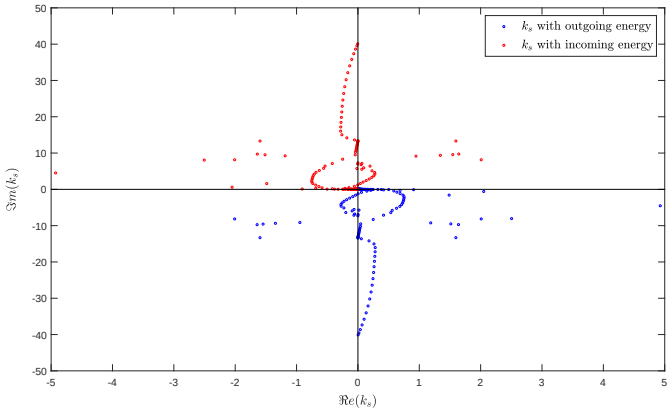

(a) Wavenumber distribution

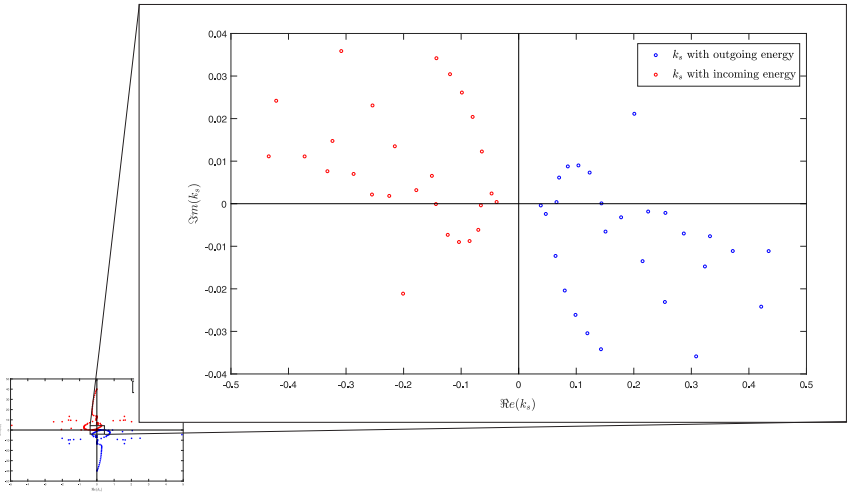

(b) Wavenumber distribution near the origin

Figure 3.8: Typical distribution of wavenumbers for a layer over PML at a fixed frequency ω_j as classified by the sign of the modal energy (red: negative group velocity/incoming energy; blue: positive group velocity/outgoing energy)

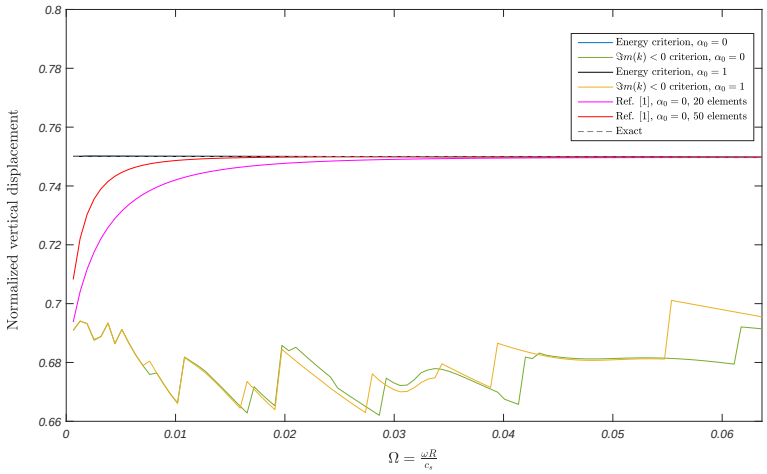

Figure 3.9: Normalized vertical displacement under the center of the disc load as a function of normalized frequency for a layer over PML; exact and approximate responses

havior: the exact response, and the two energy criterion curves (for different α_0 values) coincide. By contrast, the imaginary part criterion produces an erratic response. In the figure, we have also provided the response produced when the imaginary part criterion is applied to the implementation of [17], while increasing the depth of the PML layer and the number of elements used in the PML: though there is clear improvement, the low frequency response remains inaccurate, and can only be improved at impractical computational cost, i.e., with a very deep and finely discretized PML (the low frequency regime requires PML thickness of about 150 meters, 150 times the PML thickness we used with the energy criterion).

3.4 Inversion process

Equation (3.23) shows that the Lagrangian functional is a function of the Lagrange multipliers $\boldsymbol{\chi}_s^{(j)}$ and $\xi_s^{(j)}$, the state variables $\boldsymbol{U}_s^{(j)}$ and $k_s^{(j)}$, and the material parameters G_c, i.e.,

$$\mathfrak{L} \equiv \mathfrak{L}(\boldsymbol{\chi}_s^{(j)}, \xi_s^{(j)}, \boldsymbol{U}_s^{(j)}, k_s^{(j)}, G_c). \tag{3.25}$$

The latter (G_c) are the shear moduli of all the elements in the discretization, which are assumed to be constant for each element. The next step is to seek a stationary point for the Lagrangian, and to this end, we seek to satisfy the first-order optimality conditions by requiring that the first variations of $\mathfrak{L}$ vanish.

3.4.1 Optimality conditions

Specifically, we require that:

$$\nabla\mathfrak{L} \;=\; \begin{bmatrix} \delta_{\left[\boldsymbol{\chi}_s^{(j)}, \xi_s^{(j)}\right]}\mathfrak{L} \\ \delta_{\left[\boldsymbol{U}_s^{(j)}, k_s^{(j)}\right]}\mathfrak{L} \\ \delta_{G_c}\mathfrak{L} \end{bmatrix} = 0\ . \tag{3.26}$$

3.4.1.1 The state problem

The first variation of the Lagrangian $\mathfrak{L}$ with respect to the adjoint variables $\boldsymbol{\chi}_s^{(j)}$ and $\xi_s^{(j)}$ recovers the forward eigenvalue problem (3.17) and the

orthonormality condition (3.19):

$$\delta_{\boldsymbol{\chi}_s^{(j)}}\mathfrak{L} = 0 \Rightarrow$$
$$(\mathbf{A}^{(j)}{k_s^{(j)}}^2 + \mathbf{B}k_s^{(j)} + \mathbf{G}^{(j)} - {\omega_j}^2\mathbf{M}^{(j)})\boldsymbol{U}_s^{(j)} = 0, \tag{3.27a}$$

$$\delta_{\xi_s^{(j)}}\mathfrak{L} = 0 \Rightarrow$$
$$\frac{1}{2}{\boldsymbol{U}_s^{(j)}}^T(2\mathbf{A}^{(j)}k_s^{(j)} + \mathbf{B})\boldsymbol{U}_s^{(j)} = k_s^{(j)}. \tag{3.27b}$$

3.4.1.2 The adjoint problem

Similarly, we enforce the vanishing of the variation of $\mathfrak{L}$ with respect to the state variables, i.e., the wavenumbers $k_s^{(j)}$, and the eigenvectors $\boldsymbol{U}_s^{(j)}$. There results:

$$\begin{aligned}
&\delta_{\boldsymbol{U}_s^{(j)}}\mathfrak{L} = 0, \Rightarrow \\
&(\mathbf{A}^{(j)}{k_s^{(j)}}^2 + \mathbf{B}k_s^{(j)} + \mathbf{G}^{(j)} - \omega_j^2\mathbf{M}^{(j)})^T\boldsymbol{\chi}_s^{(j)} \\
&+ (2\mathbf{A}^{(j)}k_s^{(j)} + \mathbf{B})\boldsymbol{U}_s^{(j)}\xi_s^{(j)} \\
&= -2\frac{P_0}{\pi R}U_{s,\frac{N}{2}+1}^{(j)}\sum_{i=1}^{N_s} I_{1s}^{(j)}(r_i)\,\overline{d_i^{(j)}}\,\boldsymbol{W}_I,
\end{aligned} \tag{3.28}$$

and,

$$\begin{aligned}
&\delta_{k_s^{(j)}}\mathfrak{L} = 0, \Rightarrow \\
&{\boldsymbol{U}_s^{(j)}}^T(2\mathbf{A}^{(j)}k_s^{(j)} + \mathbf{B})^T\boldsymbol{\chi}_s^{(j)} + ({\boldsymbol{U}_s^{(j)}}^T\mathbf{A}^{(j)}\boldsymbol{U}_s^{(j)} - 1)\xi_s^{(j)} = \\
&-\frac{P_0}{\pi R}(U_{s,\frac{N}{2}+1}^{(j)})^2\sum_{i=1}^{N_s}\hat{I}_{1s}^{(j)}(r_i)\,\overline{d_i^{(j)}}.
\end{aligned} \tag{3.29}$$

In the above equations, $\boldsymbol{W}_I = \Big[0, \ldots 0, 1, 0, \ldots 0\Big]^T$, and

$$\hat{I}_{1s}^{(j)}(r) = \begin{cases} \dfrac{\pi\, i}{2k_s^{(j)}}[RJ_0(k_s^{(j)}r)H_2^{(2)}(k_s^{(j)}R) + rJ_1(k_s^{(j)}r)H_1^{(2)}(k_s^{(j)}R)] + \dfrac{2}{Rk_s^{(j)^3}}, & \\ & 0 \le r \le R \\ \dfrac{\pi\, i}{2k_s^{(j)}}[RJ_2(k_s^{(j)}R)H_0^{(2)}(k_s^{(j)}r) + rJ_1(k_s^{(j)}R)H_1^{(2)}(k_s^{(j)}r)], & R \le r \end{cases} \tag{3.30}$$

Equations (3.28) and (3.29) constitute the adjoint problem, which is a symmetric system of $N+1$ linear equations:

$$\begin{bmatrix} (\mathbf{A}^{(j)}k_s^{(j)^2} + \mathbf{B}k_s^{(j)} + \mathbf{G}^{(j)} - \omega_j^2\mathbf{M}^{(j)})^T & (2\mathbf{A}^{(j)}k_s^{(j)} + \mathbf{B})\boldsymbol{U}_s^{(j)} \\ \boldsymbol{U}_s^{(j)^T}(2\mathbf{A}^{(j)}k_s^{(j)} + \mathbf{B})^T & (\boldsymbol{U}_s^{(j)^T}\mathbf{A}^{(j)}\boldsymbol{U}_s^{(j)} - 1) \end{bmatrix} \begin{bmatrix} \boldsymbol{\chi}_s^{(j)} \\ \xi_s^{(j)} \end{bmatrix} = \begin{bmatrix} -2\frac{P_0}{\pi R}U_{s,\frac{N}{2}+1}^{(j)}\Big(\sum_{i=1}^{N_s} I_{1s}^{(j)}(r_i)\,\overline{d_i^{(j)}}\Big)\boldsymbol{W}_I \\ -\frac{P_0}{\pi R}(U_{s,\frac{N}{2}+1}^{(j)})^2\Big(\sum_{i=1}^{N_s} \hat{I}_{1s}^{(j)}(r_i)\,\overline{d_i^{(j)}}\Big) \end{bmatrix}. \tag{3.31}$$

Thus, the Lagrange multipliers, or adjoint variables, $\boldsymbol{\chi}_s^{(j)}$ and $\xi_s^{(j)}$ are obtained as a solution of the linear system (3.31), which is driven by the (conjugated) misfit, as it can be seen from the right-hand-side of (3.31).

3.4.1.3 The control problem

Lastly, we consider the variation of $\mathfrak{L}$ with respect to the unknown shear moduli G_c. There results::

$$\delta_{G_c}\mathfrak{L} = \Re e\Bigg\{ \sum_{j=1}^{M_\omega}\sum_{s=1}^{N} \boldsymbol{\chi}_s^{(j)^T}\Big(\frac{\partial \mathbf{A}^{(j)}}{\partial G_c}{k_s^{(j)}}^2 + \frac{\partial \mathbf{B}}{\partial G_c}k_s^{(j)} + \frac{\partial \mathbf{G}^{(j)}}{\partial G_c}\Big)\boldsymbol{U}_s^{(j)} + \sum_{j=1}^{M_\omega}\sum_{s=1}^{N} \xi_s^{(j)}\Big(\frac{1}{2}\boldsymbol{U}_s^{(j)^T}\Big(2\frac{\partial \mathbf{A}^{(j)}}{\partial G_c}k_s^{(j)} + \frac{\partial \mathbf{B}}{\partial G_c}\Big)\boldsymbol{U}_s^{(j)}\Big)\Bigg\}\delta G_c. \tag{3.32}$$

We note that the methodology is capable of recovering other material parameters when assumed unknown. For example, if the first Lamé parameter, the damping factor η, and/or the density ρ were to be among the unknowns, then the first-order variations of the Lagrangian $\mathcal{L}$ with respect to each of the additional parameters would need to vanish as well. In that case the variations become:

$$\delta_{\lambda_c}\mathfrak{L} = \Re e\Bigg\{ \sum_{j=1}^{M_\omega}\sum_{s=1}^{N} \boldsymbol{\chi}_s^{(j)^T}\Big(\frac{\partial \mathbf{A}^{(j)}}{\partial \lambda_c}{k_s^{(j)}}^2 + \frac{\partial \mathbf{B}}{\partial \lambda_c}k_s^{(j)} + \frac{\partial \mathbf{G}^{(j)}}{\partial \lambda_c}\Big)\boldsymbol{U}_s^{(j)} + \sum_{j=1}^{M_\omega}\sum_{s=1}^{N} \xi_s^{(j)}\Big(\frac{1}{2}\boldsymbol{U}_s^{(j)^T}\Big(2\frac{\partial \mathbf{A}^{(j)}}{\partial \lambda_c}k_s^{(j)} + \frac{\partial \mathbf{B}}{\partial \lambda_c}\Big)\boldsymbol{U}_s^{(j)}\Big)\Bigg\}\delta \lambda_c. \tag{3.33}$$

$$\delta_{\eta_c}\mathfrak{L} = \Re e\Bigg\{ \sum_{j=1}^{M_\omega}\sum_{s=1}^{N} \boldsymbol{\chi}_s^{(j)^T}\Big(\frac{\partial \mathbf{A}^{(j)}}{\partial \eta_c}{k_s^{(j)}}^2 + \frac{\partial \mathbf{B}}{\partial \eta_c}k_s^{(j)} + \frac{\partial \mathbf{G}^{(j)}}{\partial \eta_c}\Big)\boldsymbol{U}_s^{(j)} + \sum_{j=1}^{M_\omega}\sum_{s=1}^{N} \xi_s^{(j)}\Big(\frac{1}{2}\boldsymbol{U}_s^{(j)^T}\Big(2\frac{\partial \mathbf{A}^{(j)}}{\partial \eta_c}k_s^{(j)} + \frac{\partial \mathbf{B}}{\partial \eta_c}\Big)\boldsymbol{U}_s^{(j)}\Big)\Bigg\}\delta \eta_c. \tag{3.34}$$

$$\delta_{\rho_c}\mathfrak{L} = \Re e\Bigg\{ \sum_{j=1}^{M_\omega}\sum_{s=1}^{N} \boldsymbol{\chi}_s^{(j)^T}{\omega_j}^2\frac{-\partial \mathbf{M}^{(j)}}{\partial \rho_c}\boldsymbol{U}_s^{(j)}\Bigg\}\delta \rho_c. \tag{3.35}$$

Then, in addition to (3.32), the vanishing of (3.33), (3.34), and (3.35) would need to be enforced. Herein, to highlight the methodology, we only seek to enforce the vanishing of (3.32), assuming that the shear moduli are the only

unknown properties. The right-hand-side of (3.32), modulo the variation δG_c, represents the reduced gradient of the Lagrangian, since at any given inversion iteration, the state and adjoint problems are satisfied. Thus, from (3.26), it follows that, at any inversion iteration, there holds:

$$\nabla \mathfrak{L} \;=\; \begin{bmatrix} 0 \\ 0 \\ \nabla_{G_c} \mathfrak{L} \end{bmatrix} \;, \tag{3.36}$$

where, the reduced gradient is:

$$\begin{aligned} \nabla_{G_c} \mathfrak{L} = \Re e \Bigg\{ & \sum_{j=1}^{M_\omega} \sum_{s=1}^{N} \boldsymbol{\chi}_s^{(j)^T} \Big(\frac{\partial \mathbf{A}^{(j)}}{\partial G_c} k_s^{(j)^2} + \frac{\partial \mathbf{B}}{\partial G_c} k_s^{(j)} + \frac{\partial \mathbf{G}^{(j)}}{\partial G_c} \Big) \boldsymbol{U}_s^{(j)} \\ & + \sum_{j=1}^{M_\omega} \sum_{s=1}^{N} \xi_s^{(j)} \Big(\frac{1}{2} \boldsymbol{U}_s^{(j)^T} \Big(2 \frac{\partial \mathbf{A}^{(j)}}{\partial G_c} k_s^{(j)} + \frac{\partial \mathbf{B}}{\partial G_c} \Big) \boldsymbol{U}_s^{(j)} \Big) \Bigg\} \,. \end{aligned} \tag{3.37}$$

To update the shear moduli during the inversion iterations, we make use of the reduced gradient $\nabla_{G_c} \mathfrak{L}$. A gradient-based minimization scheme, similar to the one used and described in [55] is employed to determine the shear moduli G_c. A summary of the inversion algorithm is repeated in Appendix 3.D.

3.4.2 Frequency-continuation scheme

The signal agility of modern wave-generating equipment allows probing at a wide range of frequencies, thus affording, to advantage, the design of inverse medium field experiments. We mimic such field experiments with synthetic probes that follow a frequency continuation scheme, aiming at the alleviation of the inherent solution multiplicity. This is particularly important in this case, since no other regularization scheme is enlisted.

Specifically, the layered medium is first probed with a first set of $M_\omega^{(1)}$ frequencies, whose range is between ω_0 and ω_1, and the properties (shear moduli) are reconstructed using Algorithm 2, starting with an initial guess of homogeneous modulus distribution. Once the properties are reconstructed, the medium is probed again with a second set $M_\omega^{(2)}$ of frequencies, within the range (ω_0, ω_2) with $\omega_2 > \omega_1$, starting with the previously converged property profile as initial guess. The process continues until the convergence criterion (misfit reduction and/or number of iterations) is met. Typically, a small number (3-5) of frequency sets is needed, with only 5 to 10 randomly selected frequencies per set. We note that the initial set $M_\omega^{(1)}$ contains low frequencies, while for subsequent sets the frequency range is widened to include higher frequencies.

3.5 Numerical results

We discuss first four cases of varying complexity that are based on noise-free synthetic data and the dispersion-constrained inversion process described earlier. The first case (case A) involves a typical heterogeneous layered halfspace with shear moduli monotonically increasing with depth. The second case (case B) pertains to a layered halfspace with an interspersing soft layer between stiffer layers (a, so-called, inverse layer). For the third case (case C), we consider a target profile with a stiff but fairly thin layer at the top, to mimic pavements; and for the last case (case D) we consider a deeper layered halfspace structure with multiple layers and monotonically increasing shear moduli. Finally, we revisit case A, but drive it with noisy data, to numerically

assess the impact of noise in the inversion quality. In all cases, to quantify the fitness of the inverted profile with respect to the target, we define the following normalized L_2-like fitness metric:

$$\mathcal{E} = \left[\frac{\int_0^{z_n} (G_e - G_c)^2 dz}{\int_0^{z_n} {G_e}^2 dz} \right]^{0.5}, \tag{3.38}$$

where G_e denotes the exact shear modulus profile.

3.5.1 Inversion with noise-free data

3.5.1.1 Case A: Layered halfspace with monotonically increasing moduli

We consider first a target layered halfspace made of two layers over halfspace, where every layer has larger shear modulus than the overlaying layer. Figure 3.10 depicts the profile of the physical problem and of the PML-truncated computational model.

The mass density ρ for all layers is set to 1800 kg/m^3. Poisson's ratio ν is 0.25 for all layers, and a very small damping $\eta = 0.001$ is used. The disc load radius is $R = 15$cm. The target shear modulus profile is:

$$G = \begin{cases} 300\,\text{MPa} & 0 \leq \text{z} \leq 0.8\,\text{m} \\ 400\,\text{MPa} & 0.8\,\text{m} \leq \text{z} \leq 1.5\,\text{m} \\ 500\,\text{MPa} & 1.5\,\text{m} \leq \text{z} \end{cases}$$

For the inversion, we use 25 quadratic elements to discretize the interior domain and 7 quadratic elements for the PML, i.e, each element in the interior domain is 0.08m long and in the PML about 0.07m long. On the other hand, to avoid committing an "inverse crime," we use 60 quadratic elements to produce

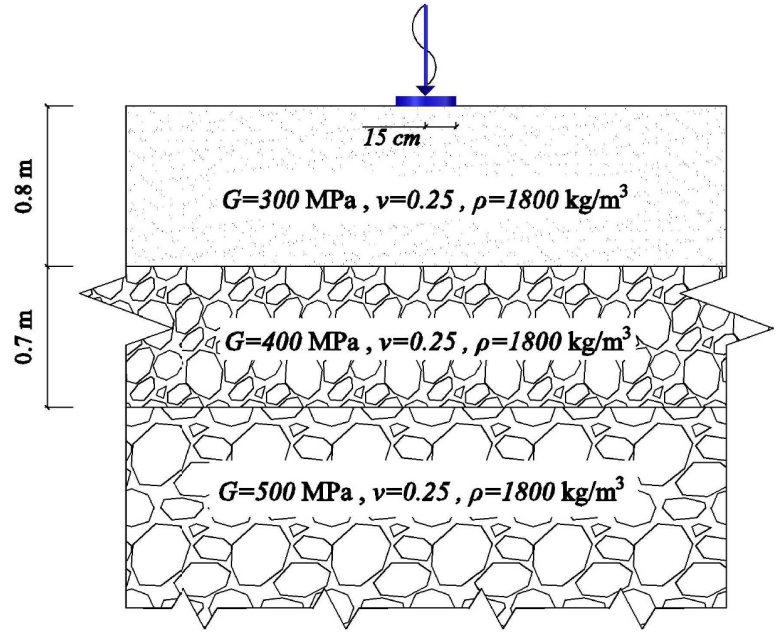

(a) Case A - Physical profile

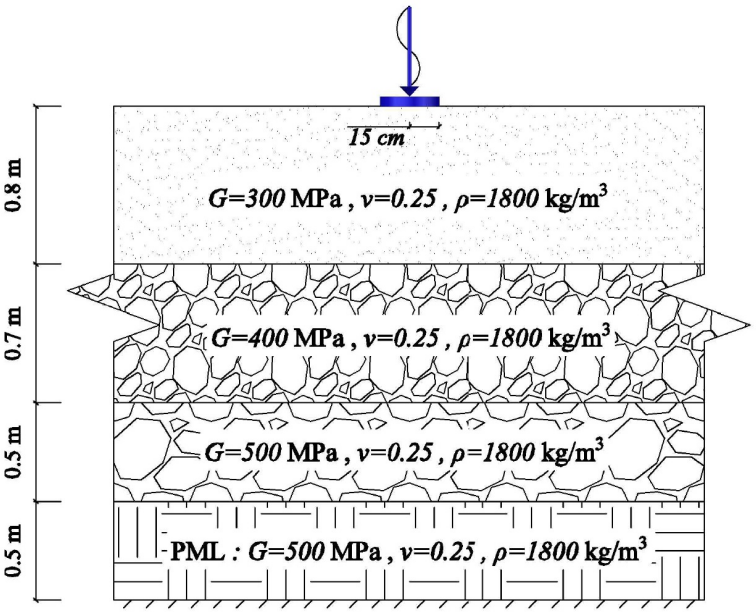

(b) Case A - PML-truncated model

Figure 3.10: Case A - Physical profile and PML-truncated model

the synthetic data. Following the frequency-continuation scheme described in section 3.4.2, we start from a homogeneous initial guess of 100 MPa and use four sets of 10 randomly distributed frequencies within each set; the sets are [0,25] Hz, [0,50] Hz, [0,100] Hz and [0,150] Hz. Figure 3.12 shows the inverted profile at the end of the inversion procedure for each M_ω set. It is noted, as discussed in section 3.4.2, that the first set, which has a lower frequency content, constructs an approximate profile starting from a homogeneous initial guess, while the subsequent sets enhance the profile as convergence to the target profile is attained. Figure 3.11 shows the progress of the misfit through all four frequency sets. We can see that for each frequency set, we have a drop in the misfit of about four orders of magnitude in 2000 iterations. The fitness metric after each frequency set is indicative of the convergence progress.

Figure 3.12(d) represents the final reconstructed shear modulus profile when starting from a homogeneous initial guess. The piecewise-constant modulus distribution reflects the assumption that the modulus is constant within each element. Overall, the three layers and their interfaces have been well recovered, and the final profile is quite close to the target ($\mathcal{E} = 4.8\%$). We note that the last layer represents the properties of the halfspace.

3.5.1.2 Case B: Layered halfspace with a soft trapped between stiffer layers

Next, we consider a layered halfspace with two layers over a homogeneous halfspace with ρ=1800 kg/m^3, ν=0.25, $\eta = 0.001$ and the following

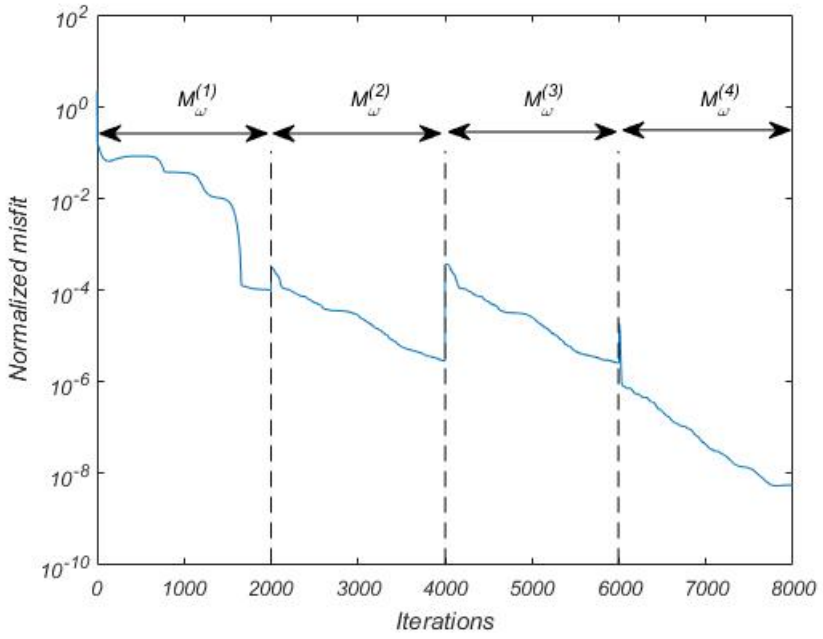

Figure 3.11: Case A - Misfit progress for each frequency set

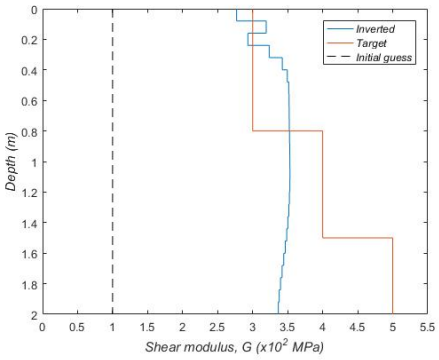

(a) Case A - after $M_\omega^{(1)}$, $\mathcal{E}$=22%

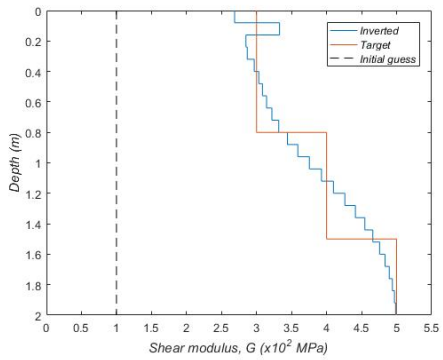

(b) Case A - after $M_\omega^{(2)}$, $\mathcal{E}$=7.2%

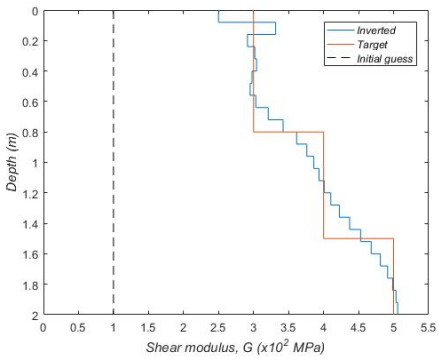

(c) Case A - after $M_\omega^{(3)}$, $\mathcal{E}$=6.1%

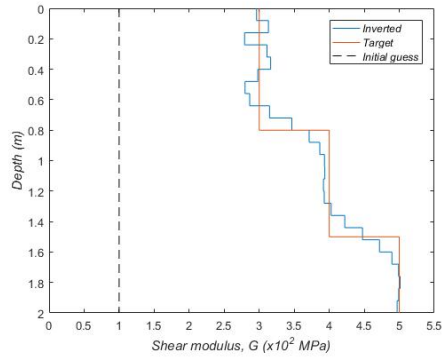

(d) Case A - after $M_\omega^{(4)}$, $\mathcal{E}$=4.8%

Figure 3.12: Case A: target and inverted shear modulus profiles shown at the end of the inversion process for each frequency set M_ω, with fitness metric $\mathcal{E}$

shear modulus target profile:

$$G = \begin{cases} 200\,\text{MPa} & 0 \leq \text{z} \leq 1\,\text{m} \\ 150\,\text{MPa} & 1 \leq \text{z} \leq 1.5\,\text{m} \\ 250\,\text{MPa} & 1.5 \leq \text{z} \end{cases}$$

Figure 3.13 shows the profile of the layered halfspace and the PML-truncated model. We use again 25 quadratic elements along the depth of the interior domain and 5 quadratic elements for the PML in the inversion process, and 65 quadratic elements for creating the synthetic data. The same frequency continuation scheme is used as in case A. We note that there is a thin layer between $1 \leq z \leq 1.5$ m, which has a smaller shear modulus with respect to the adjacent layers. Figure 3.14 shows the inverted profile at the end of the inversion process for each M_ω set. It can be seen that the reconstruction is quite acceptable: this profile is usually hard to image due to the presence of the softer layer that tends to trap the motion and inhibit the reconstruction of the deeper structure. The fitness metric associated with this case is $\mathcal{E} = 5.2\%$.

3.5.1.3 Case C: A thin top layer - typical pavement structure

Next, we consider a medium comprising two layers over halfspace, where the top layer is rather thin and stiff (a typical pavement profile). Figure 3.15 shows the profile of the layered halfspace and the PML-truncated model. The target profile is:

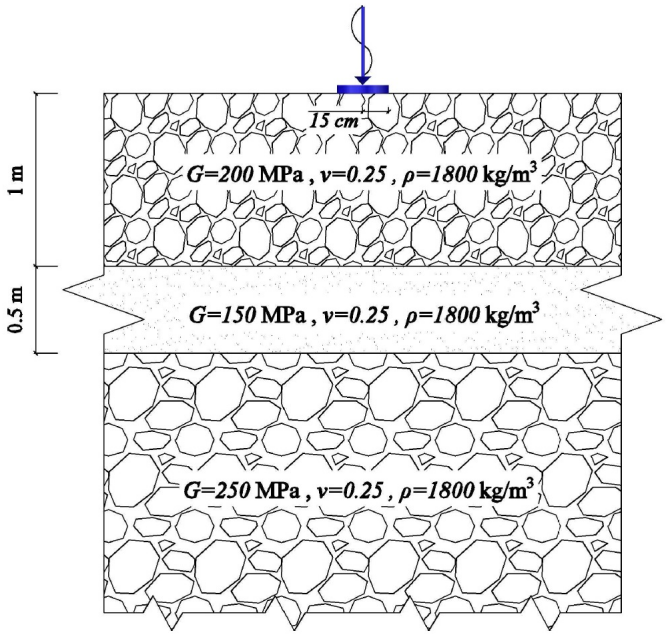

(a) Case B - Physical profile

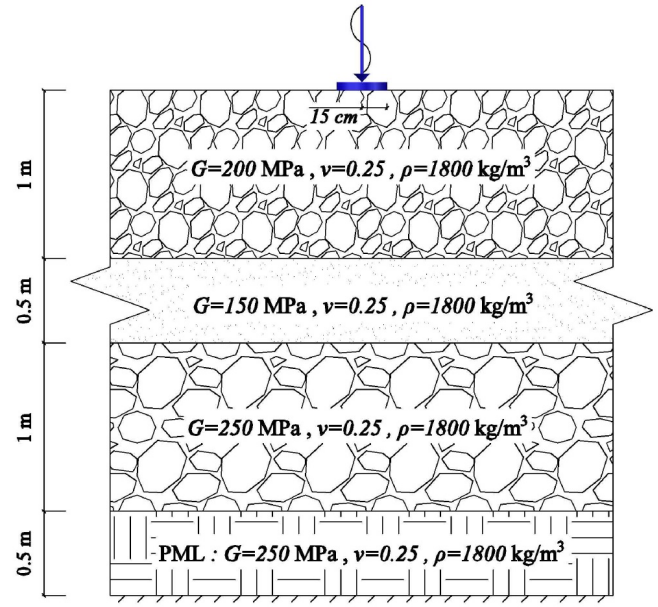

(b) Case B - PML-truncated model

Figure 3.13: Case B - Physical profile and PML-truncated model

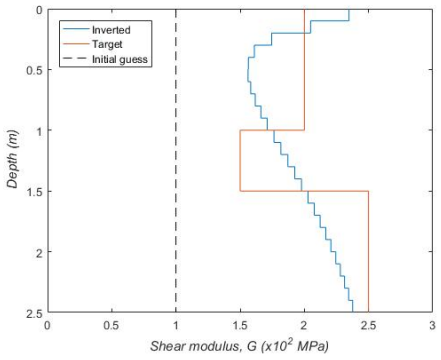

(a) Case B - after $M_\omega^{(1)}$, $\mathcal{E}$=16%

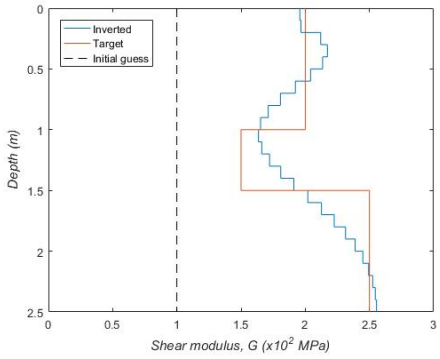

(b) Case B - after $M_\omega^{(2)}$, $\mathcal{E}$=10%

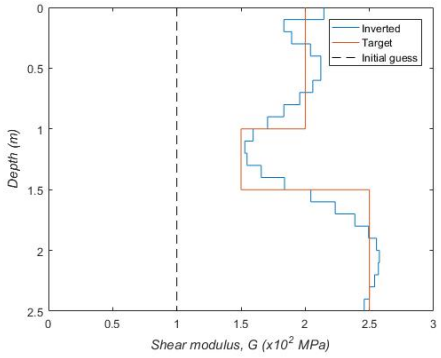

(c) Case B - after $M_\omega^{(3)}$, $\mathcal{E}$=7.7%

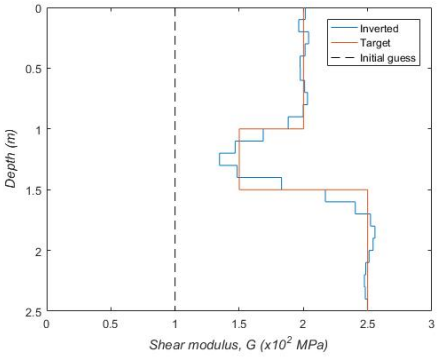

(d) Case B - after $M_\omega^{(4)}$, $\mathcal{E}$=5.2%

Figure 3.14: Case B: target and inverted shear modulus profiles shown at the end of the inversion process for each frequency set M_ω, with fitness metric $\mathcal{E}$

$$G = \begin{cases} 1000\,MPa & 0 \le z \le 0.2\,m \\ 400\,MPa & 0.2 \le z \le 0.7\,m \\ 600\,MPa & 0.7\,m \le z \end{cases}$$

For the inversion, we use 30 quadratic elements along the depth of the interior domain and 10 quadratic elements for the PML, each 0.05m long. For the synthetic data, 75 quadratic elements have been used. We use the same frequency continuation scheme as in the preceding cases. The inverted profiles for each frequency set are shown in Fig. 3.16.

Despite the thinness of the top layer, and the sharp contrast (jump) in the shear moduli between the top and second layers, the inversion process has again quite satisfactorily recovered the target, with a fitness of $\mathcal{E} = 9.1\%$.

3.5.1.4 Case D: A deep multi-layer heterogeneous halfspace with monotonically increasing shear moduli

We consider next a layered medium comprising four layers over halfspace, where each layer is stiffer than the layer above. In this case, the overall depth of the physical layers to disk radius ratio is about 26 (twice the ratio of case A). Figure 3.17 shows the profile of the layered halfspace and the PML-truncated model. The target profile is:

$$G = \begin{cases} 200\,MPa & 0 \le z \le 0.5\,m \\ 300\,MPa & 0.5 \le z \le 1.2\,m \\ 380\,MPa & 1.2 \le z \le 2\,m \\ 520\,MPa & 2 \le z \le 3\,m \\ 700\,MPa & 3\,m \le z \end{cases}$$

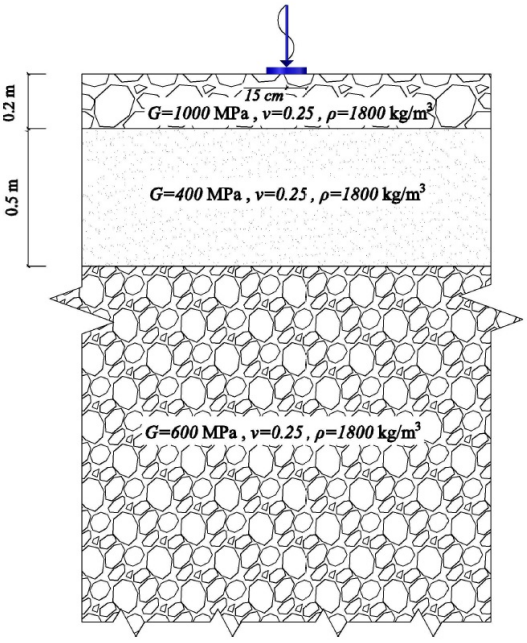

(a) Case C - Physical profile

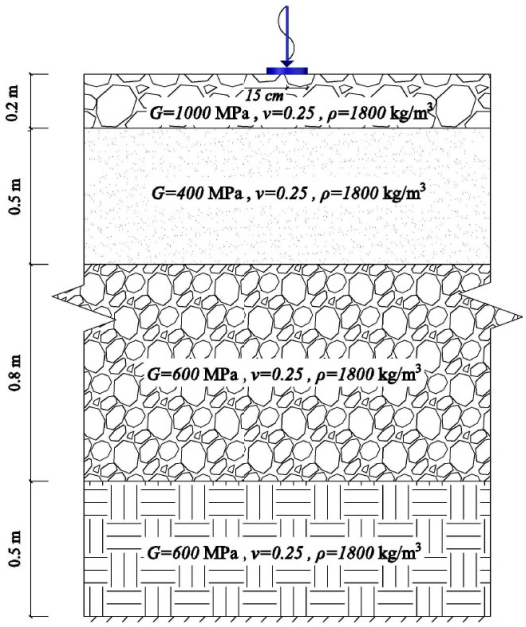

(b) Case C - PML-truncated model

Figure 3.15: Case C - Physical profile and PML-truncated model

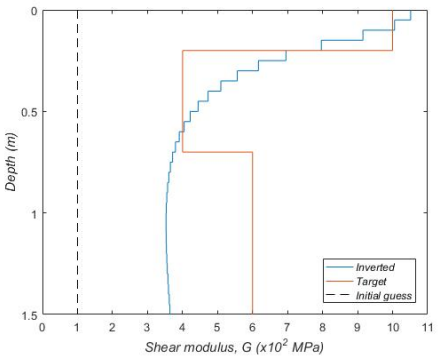

(a) Case C - after $M_\omega^{(1)}$, $\mathcal{E}$=33%

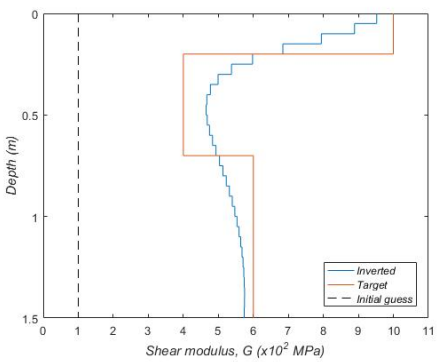

(b) Case C - after $M_\omega^{(2)}$, $\mathcal{E}$=17%

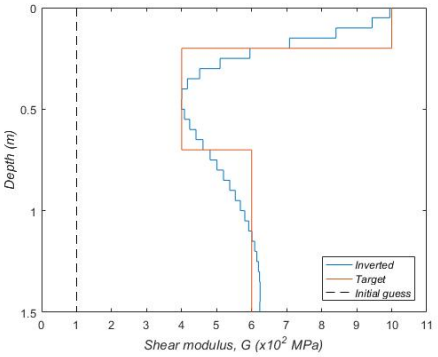

(c) Case C - after $M_\omega^{(3)}$, $\mathcal{E}$=14%

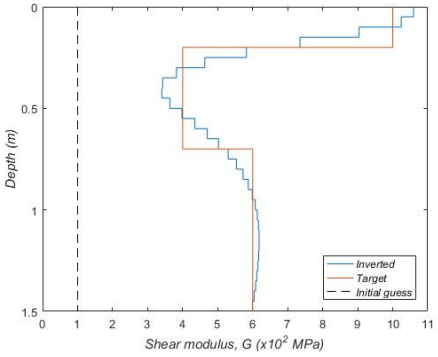

(d) Case C - after $M_\omega^{(4)}$, $\mathcal{E}$=9.1%

Figure 3.16: Case C: target and inverted shear modulus profiles shown at the end of the inversion process for each frequency set M_ω, with fitness metric $\mathcal{E}$

We use 70 quadratic elements to create the synthetic data, and for the inversion, we use 32 quadratic elements along the depth of the interior domain, and 4 quadratic elements for the PML, each of the elements 0.125m long. We use the same frequency continuation scheme as in the preceding cases. The inverted profiles for each frequency set are shown in Fig. 3.18.

We note that the inverted profile for the top layers is almost perfect, and well reconstructed for the deeper layers, with an overall fitness of $\mathcal{E} = 4.9\%$.

3.5.2 Inversion with noisy data

To show the performance of method in the presence of noise, we add 5% Gaussian noise to the synthetic data and revisit case A.

3.5.2.1 Case E: Case A with noisy response

We consider again case A with the same shear modulus profile and the rest of the mechanical properties as before. We also use the same frequency sets used for the inversion in case A. Here, we use 20 quadratic elements for the interior domain and 5 quadratic elements for the PML. To generate the noisy data, we treated the synthetic complex displacements over all frequency sets as a (power) signal, assumed a 5% background noise, and computed the signal-to-noise ratio. We then used Matlab's Gaussian noise function to generate the noisy data. The resulting noisy displacement amplitudes varied between 0.05% and 4.4% of the unperturbed case A synthetic data.

Figure 3.20 shows the inverted shear modulus profile at the end of each

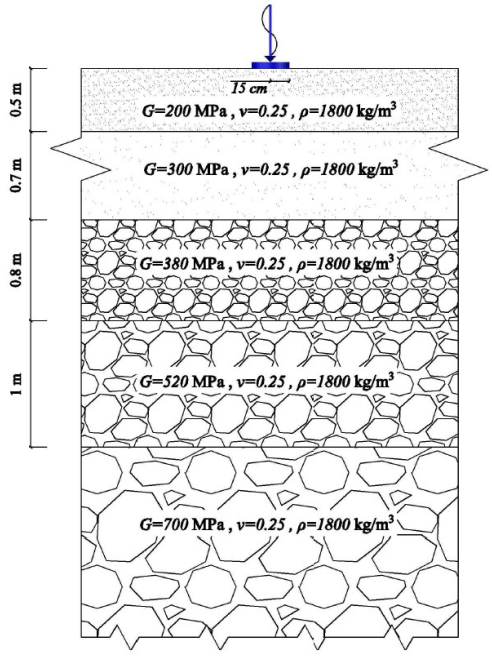

(a) Case D - Physical profile

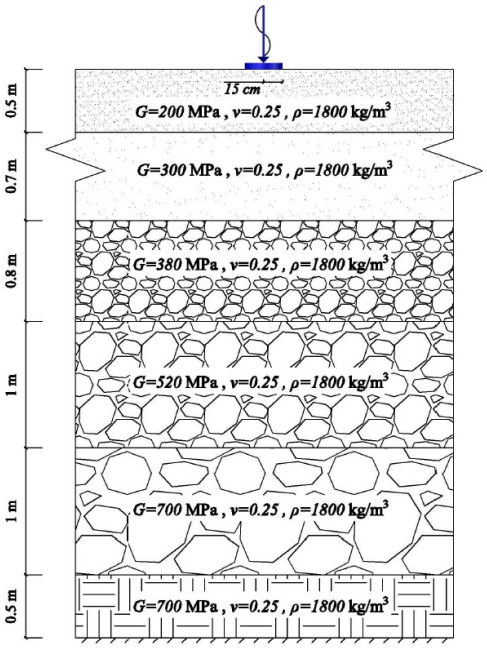

(b) Case D - PML-truncated model

Figure 3.17: Case D - Physical profile and PML-truncated model

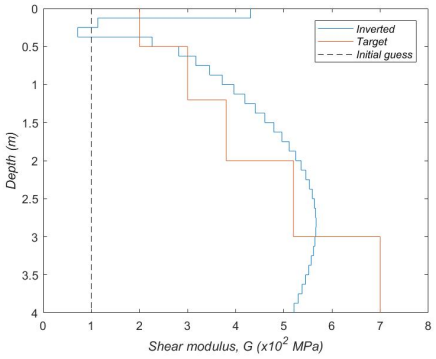

(a) Case D - after $M_\omega^{(1)}$, $\mathcal{E}$=22%

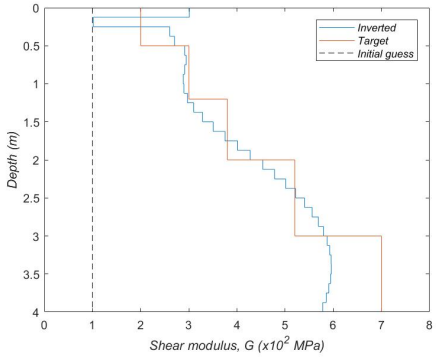

(b) Case D - after $M_\omega^{(2)}$, $\mathcal{E}$=14%

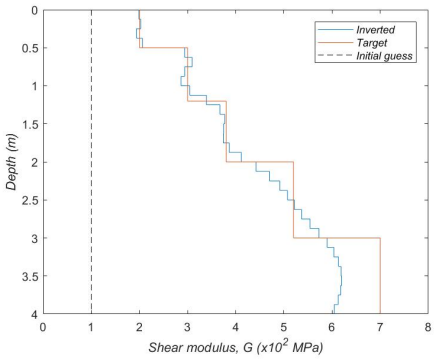

(c) Case D - after $M_\omega^{(3)}$, $\mathcal{E}$=10.3%

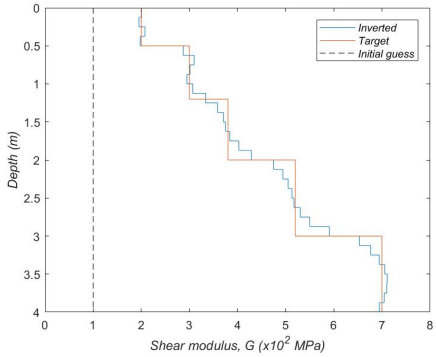

(d) Case D - after $M_\omega^{(4)}$, $\mathcal{E}$=4.9%

Figure 3.18: Case D: target and inverted shear modulus profiles shown at the end of the inversion process for each frequency set M_ω, with fitness metric $\mathcal{E}$

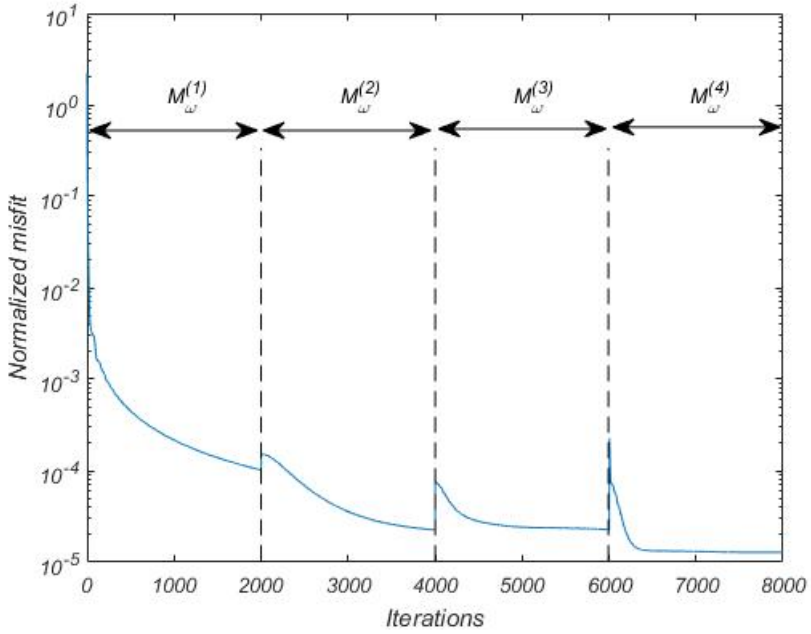

Figure 3.19: Case E - Misfit progress for each frequency set

frequency set along with the corresponding fitness metric. The inverted profile is reasonable, despite the rise in the final fitness metric from 4.8% (Case A) to 7.7%. The second layer is not fully recovered, yet the monotonic rise in shear modulus toward the halfspace is clearly seen. Figure 3.19 shows the progress of the misfit reduction through each set of frequencies.

We can see that after the first frequency set, which caused a drop of four orders of magnitudes in the misfit, the other three frequency sets have resulted in one to two orders of magnitude in misfit reduction, which is expected due to the presence of noise. With a 5% noise in the data, it is impossible to realize misfits below 10^{-5}, however, the fitness metric has been improved in

each set, despite the relatively small changes in the misfit. Figure 3.21 depicts the frequency response of the target and inverted profile, along with the noisy data used for each set of inversion. The closeness of the noise-free-based and noise-based responses is evident from the figure. In fact, the response is typical of near-surface deposits: the absence of rapid (frequency) oscillations is what makes the implementation of an explicit regularization scheme unnecessary, and allows the adoption of relatively coarse meshes.

3.6 Conclusion

We discussed a new dispersion-constrained optimization method for the full-waveform-based resolution of the inverse medium problem associated with the reconstruction of the material profile of a layered medium on a halfspace. The methodology rests on the minimization of the misfit between sensor data in the frequency domain and computed responses, constrained by the discrete eigenvalue problem. To construct the latter, we relied on the coupling of the Thin Layer Method (TLM) with a Perfectly-Matched-Layer (PML), and devised a new procedure, based on an outgoing energy criterion, to arrive at the set of acceptable eigenvalues/wavenumbers. The reduction of an initially three-dimensional problem to a problem defined over one spatial dimension, afforded by the TLM, makes the presented inversion methodology highly promising for various applications where the layered assumption is reasonably well-founded. The numerical experiments demonstrated the capability of the method to recover satisfactorily the material parameters, whether driven by noise-free or

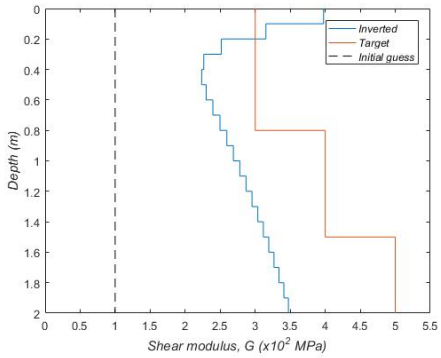

(a) Case E - after $M_\omega^{(1)}$, $\mathcal{E}$=29%

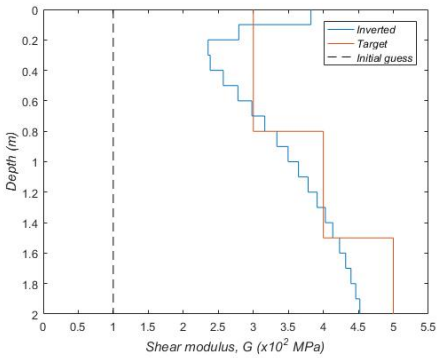

(b) Case E - after $M_\omega^{(2)}$, $\mathcal{E}$=12%

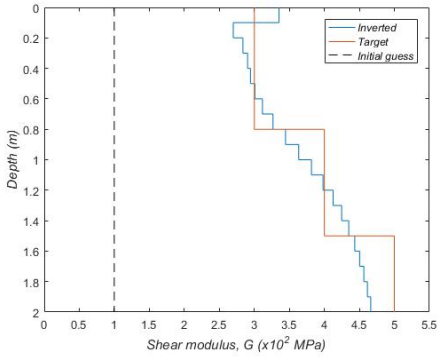

(c) Case E - after $M_\omega^{(3)}$, $\mathcal{E}$=8.9%

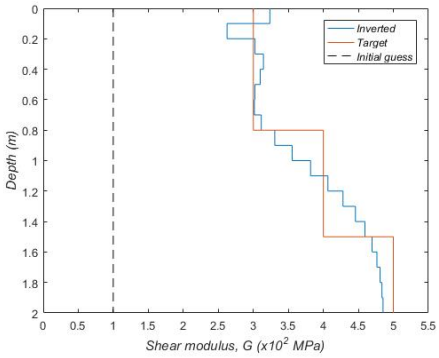

(d) Case E - after $M_\omega^{(4)}$, $\mathcal{E}$=7.7%

Figure 3.20: Case E: target and inverted shear modulus profiles shown at the end of the inversion process for each frequency set M_ω, with fitness metric $\mathcal{E}$

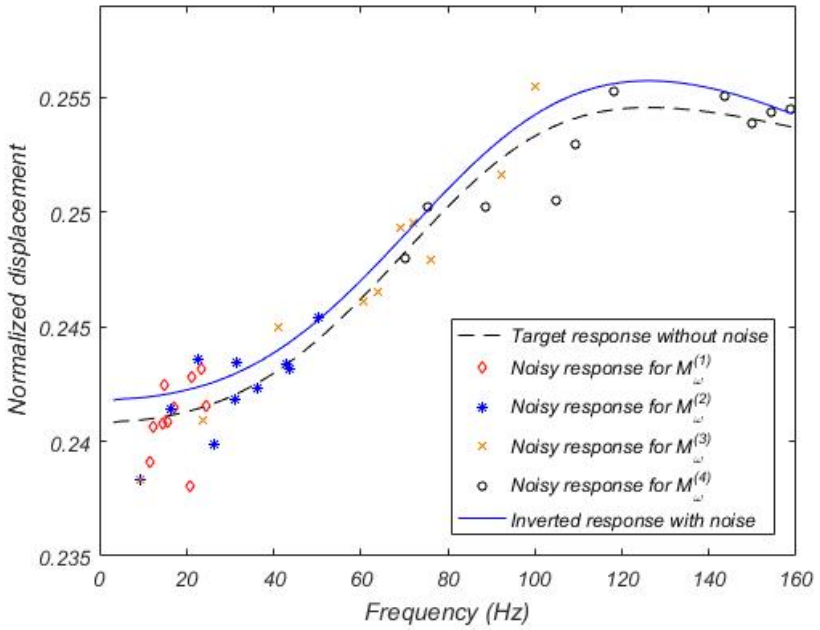

Figure 3.21: Frequency responses of the target profile for cases A and E, of the inverted profile with noisy data, along with the sensor data used for each frequency set

noisy sensor data.

3.A Discretization details

Within every layer i, the elements are numbered from the top of the layer, with z_a denoting the z coordinate at the beginning of the j-th element, with $j = 1, ..., e_i$ (Fig. 3.4). That is:

$$z_a = z_{i-1} + (j-1)\frac{z_i - z_{i-1}}{e_i} \qquad , \qquad j = 1, ..., e_i \; . \tag{3.39}$$

Consequently, $U_{s,l}$ and $U_{s,m}$ indicate the l-th and m-th components of the $\boldsymbol{U}_s$ eigenvector, respectively. We note that the $\boldsymbol{U}_s$ eigenvector's components are arranged such that all the $\frac{N}{2}$ radial components are first, followed by the $\frac{N}{2}$ vertical components. Accordingly:

$$\begin{aligned} &l = 1 + d(j-1), \\ &m = \tfrac{N}{2} + 1 + d(j-1) && \text{if } i = 1 \end{aligned} \tag{3.40a}$$

$$\begin{aligned} &l = 1 + d(j-1) + \sum_{f=1}^{i-1} e_f d, \\ &m = \tfrac{N}{2} + 1 + d(j-1) + \sum_{f=1}^{i-1} e_f d && \text{if } i \neq 1 \end{aligned} \tag{3.40b}$$

3.B Global matrices

A,**B**,**G** and **M** are global matrices assembled using the individual layer matrices, i.e.,

$$\begin{aligned} \mathbf{A} &= \sum_{i=1}^{n} \mathcal{A}_i + \mathcal{A}_{\text{PML}} \quad , \quad \mathbf{B} = \sum_{i=1}^{n} \mathcal{B}_i + \mathcal{B}_{\text{PML}} \quad , \\ \mathbf{G} &= \sum_{i=1}^{n} \mathcal{G}_i + \mathcal{G}_{\text{PML}} \quad , \quad \mathbf{M} = \sum_{i=1}^{n} \mathcal{M}_i + \mathcal{M}_{\text{PML}}, \end{aligned} \tag{3.41}$$

where the i-th layer matrices $\mathcal{A}_i$, $\mathcal{B}_i$, $\mathcal{G}_i$ and $\mathcal{M}_i$ are defined as:

$$\mathcal{A}_i = \begin{bmatrix} (\lambda_i + 2G_i) \int_{z_{i-1}}^{z_i} \boldsymbol{\phi}\boldsymbol{\phi}^T dz & 0 \\ 0 & G_i \int_{z_{i-1}}^{z_i} \boldsymbol{\phi}\boldsymbol{\phi}^T dz \end{bmatrix}, \tag{3.42a}$$

$$\mathcal{G}_i = \begin{bmatrix} G_i \int_{z_{i-1}}^{z_i} \boldsymbol{\phi}'\boldsymbol{\phi}'^T dz & 0 \\ 0 & (\lambda_i + 2G_i) \int_{z_{i-1}}^{z_i} \boldsymbol{\phi}'\boldsymbol{\phi}'^T dz \end{bmatrix}, \tag{3.42b}$$

$$\mathcal{M}_i = \rho_i \begin{bmatrix} \int_{z_{i-1}}^{z_i} \boldsymbol{\phi}\boldsymbol{\phi}^T dz & 0 \\ 0 & \int_{z_{i-1}}^{z_i} \boldsymbol{\phi}\boldsymbol{\phi}^T dz \end{bmatrix}, \tag{3.42c}$$

$$\mathcal{B}_i = \begin{bmatrix} 0 & \lambda_i \int_{z_{i-1}}^{z_i} \boldsymbol{\phi}\boldsymbol{\phi}'^T dz - G_i \int_{z_{i-1}}^{z_i} \boldsymbol{\phi}'\boldsymbol{\phi}^T dz \\ \lambda_i \int_{z_{i-1}}^{z_i} \boldsymbol{\phi}'\boldsymbol{\phi}^T dz - G_i \int_{z_{i-1}}^{z_i} \boldsymbol{\phi}\boldsymbol{\phi}'^T dz & 0 \end{bmatrix}, \tag{3.42d}$$

and for the PML:

$$\mathcal{A}_{\mathrm{PML}} = \begin{bmatrix} (\lambda_{\mathrm{PML}} + 2G_{\mathrm{PML}}) \int_{z_n}^{z_{n+1}} \varepsilon_z \boldsymbol{\phi}\boldsymbol{\phi}^T dz & 0 \\ 0 & G_{\mathrm{PML}} \int_{z_n}^{z_{n+1}} \varepsilon_z \boldsymbol{\phi}\boldsymbol{\phi}^T dz \end{bmatrix},$$

$$\mathcal{B}_{\mathrm{PML}} = \begin{bmatrix} 0 & \lambda_{\mathrm{PML}} \int_{z_n}^{z_{n+1}} \boldsymbol{\phi}\boldsymbol{\phi}'^T dz - G_{\mathrm{PML}} \int_{z_n}^{z_{n+1}} \boldsymbol{\phi}'\boldsymbol{\phi}^T dz \\ \lambda_{\mathrm{PML}} \int_{z_n}^{z_{n+1}} \boldsymbol{\phi}'\boldsymbol{\phi}^T dz - G_{\mathrm{PML}} \int_{z_n}^{z_{n+1}} \boldsymbol{\phi}\boldsymbol{\phi}'^T dz & 0 \end{bmatrix},$$

$$\mathcal{G}_{\mathrm{PML}} = \begin{bmatrix} G_{\mathrm{PML}} \int_{z_n}^{z_{n+1}} \frac{1}{\varepsilon_z} \boldsymbol{\phi}'\boldsymbol{\phi}'^T dz & 0 \\ 0 & (\lambda_{\mathrm{PML}} + 2G_{\mathrm{PML}}) \int_{z_n}^{z_{n+1}} \frac{1}{\varepsilon_z} \boldsymbol{\phi}'\boldsymbol{\phi}'^T dz \end{bmatrix},$$

$$\mathcal{M}_{\mathrm{PML}} = \rho_{\mathrm{PML}} \begin{bmatrix} \int_{z_n}^{z_{n+1}} \varepsilon_z \boldsymbol{\phi}\boldsymbol{\phi}^T dz & 0 \\ 0 & \int_{z_n}^{z_{n+1}} \varepsilon_z \boldsymbol{\phi}\boldsymbol{\phi}^T dz \end{bmatrix}. \tag{3.43}$$

We note that, due to the dependence of ε_z on frequency ω and depth z, the global matrices are functions of geometry, material properties and frequency, and the integrals should be computed numerically. Upon assembly of all the layers, the right-hand-sides of equations (3.8) and (3.13) will sum up to zero, due to the interfacial traction continuity conditions. It is noted that the layer matrices are of dimension $[2(e_i d + 1)] \times [2(e_i d + 1)]$ for the interior layer, and $[2(e_{\mathrm{PML}} d + 1)] \times [2(e_{\mathrm{PML}} d + 1)]$ for the PML.

3.C Energy flux

3.C.1 Interior domain

The total energy flux defined as the average amount of energy passing through the curved surface of a cylinder with radius r_0 (for $r_0 > R$) in one cycle ($0 < t < T = \frac{2\pi}{\omega}$) is equal:

$$E_s = -\frac{1}{T}\int_0^T\int_0^{z_n}\int_0^{2\pi}\left[\hat{\sigma}_r(r,z,t)\frac{d\hat{u}(r,z,t)}{dt} + \hat{\tau}_{rz}(r,z,t)\frac{d\hat{w}(r,z,t)}{dt}\right] r_0\, d\theta\, dz\, dt, \tag{3.44}$$

where

$$\hat{\sigma}_r(r,z,t) = \tilde{\sigma}_r(r,z)e^{i\omega t},\ \hat{\tau}_{rz}(r,z,t) = \tilde{\tau}_{rz}(r,z)e^{i\omega t} \tag{3.45}$$

$$\hat{u}(r,z,t) = \tilde{u}(r,z)e^{i\omega t},\ \hat{w}(r,z,t) = \tilde{w}(r,z)e^{i\omega t} \tag{3.46}$$

and,

$$\frac{d\hat{u}}{dt} = i\omega\tilde{u} = \dot{\tilde{u}}, \quad \frac{d\hat{w}}{dt} = i\omega\tilde{w} = \dot{\tilde{w}}. \tag{3.47}$$

Therefore,

$$\begin{aligned} E_s &= -\pi\Re e\Big\{\int_0^{z_n}\Big[r\tilde{\sigma}_r\overline{\dot{\tilde{u}}} + r\tilde{\tau}_{rz}\overline{\dot{\tilde{w}}}\Big]dz\Big\} \\ &= -\pi r\Re e\Big\{\int_0^{z_n}\Big[\tilde{\sigma}_r(-i\omega\bar{\tilde{u}}) + \tilde{\tau}_{rz}(-i\omega\bar{\tilde{w}})\Big]dz\Big\}. \end{aligned} \tag{3.48}$$

Substituting

$$\tilde{u}(r,z) = u(z)H_1^{(2)}(kr),\ \tilde{w}(r,z) = w(z)H_0^{(2)}(kr), \tag{3.49}$$

in (3.48) results in:

$$E_s = -\pi r_0 \omega \Im m\Big\{ k_s H_0^{(2)} \overline{H_1^{(2)}} \int_0^{z_n} (\lambda + 2G)\overline{u} u dz - \\ k_s H_1^{(2)} \overline{H_0^{(2)}} \int_0^{z_n} G\overline{w} w dz + \\ H_0^{(2)} \overline{H_1^{(2)}} \int_0^{z_n} \lambda \overline{u} \frac{dw}{dz} dz + \\ H_1^{(2)} \overline{H_0^{(2)}} \int_0^{z_n} G\overline{w} \frac{du}{dz} dz \Big\}, \tag{3.50}$$

where a bar over a variable denotes complex conjugate of the subtended variable and the argument of the Hankel functions is $k_s r_0$. Upon introduction of the displacement approximants, there results:

$$E_s = -\pi \omega r_0 \Im m\Big\{ \bar{\boldsymbol{U}}_s^T \mathbf{H}_s (k_s \mathbf{A} + \mathbf{D}) \boldsymbol{U}_s \Big\}, \tag{3.51}$$

where,

$$\mathbf{D} = \sum_{i=1}^{n} \mathcal{D}_i, \quad \mathcal{D}_i = \begin{bmatrix} 0 & \lambda_i \int\limits_{z_{i-1}}^{z_i} \boldsymbol{\phi}\boldsymbol{\phi}'^T dz \\ -G_i \int\limits_{z_{i-1}}^{z_i} \boldsymbol{\phi}\boldsymbol{\phi}'^T dz & 0 \end{bmatrix} \tag{3.52}$$

$$\mathbf{H}_s = \begin{bmatrix} H_0^{(2)}(k_s r_0)\overline{H_1^{(2)}}(k_s r_0) & 0 \\ 0 & -H_1^{(2)}(k_s r_0)\overline{H_0^{(2)}}(k_s r_0) \end{bmatrix} \tag{3.53}$$

and $\mathbf{D} + \mathbf{D}^T = \mathbf{B}$.

3.C.2 PML domain

In the PML layer, we similarly have:

$$\begin{aligned} E_s = -\pi r_0 \omega \Im m\Big\{ & k_s H_0^{(2)} \overline{H_1^{(2)}} \int_{z_n}^{z_{n+1}} (\lambda_{\mathrm{PML}} + 2G_{\mathrm{PML}}) \overline{u} u dz - \\ & k_s H_1^{(2)} \overline{H_0^{(2)}} \int_{z_n}^{z_{n+1}} G_{\mathrm{PML}} \overline{w} w dz + \\ & H_0^{(2)} \overline{H_1^{(2)}} \int_{z_n}^{z_{n+1}} \lambda_{\mathrm{PML}} \overline{u} \frac{dw}{dz} dz + \\ & H_1^{(2)} \overline{H_0^{(2)}} \int_{z_n}^{z_{n+1}} G_{\mathrm{PML}} \overline{w} \frac{du}{dz} dz \Big\} \\ = -\pi \omega r_0 \Im m\Big\{ & \bar{\boldsymbol{U}}_s^T \mathbf{H}_s (k_s \mathcal{A}_{e,\mathrm{PML}} + \mathcal{D}_{e,\mathrm{PML}}) \boldsymbol{U}_s \Big\}, \end{aligned} \tag{3.54}$$

where,

$$\mathcal{A}_{e,\mathrm{PML}} = \begin{bmatrix} (\lambda_{\mathrm{PML}} + 2G_{\mathrm{PML}}) \int_{z_n}^{z_{n+1}} \boldsymbol{\phi}\boldsymbol{\phi}^T dz & 0 \\ 0 & G_{\mathrm{PML}} \int_{z_n}^{z_{n+1}} \boldsymbol{\phi}\boldsymbol{\phi}^T dz \end{bmatrix}, \tag{3.55}$$

$$\mathcal{D}_{e,\mathrm{PML}} = \begin{bmatrix} 0 & \lambda_{\mathrm{PML}} \int_{z_n}^{z_{n+1}} \frac{1}{\varepsilon_z} \boldsymbol{\phi}\boldsymbol{\phi}'^T dz \\ -G_{\mathrm{PML}} \int_{z_n}^{z_{n+1}} \frac{1}{\varepsilon_z} \boldsymbol{\phi}\boldsymbol{\phi}'^T dz & 0 \end{bmatrix}. \tag{3.56}$$

3.C.3 Combined interior and PML domains

Therefore, for a layered half-space, approximated as a layered medium over PML, the modal total energy flux can be defined as:

$$E_s = -\pi \omega r_0 \Im m\Big\{ \bar{\boldsymbol{U}}_s^T \mathbf{H}_s (k_s \mathbf{A}_e + \mathbf{D}_e) \boldsymbol{U}_s \Big\}, \tag{3.57}$$

where,

$$\mathbf{A}_e = \sum_{i=1}^{n} \mathcal{A}_i + \mathcal{A}_{e,\mathrm{PML}}, \quad \mathbf{D}_e = \sum_{i=1}^{n} \mathcal{D}_i + \mathcal{D}_{e,\mathrm{PML}}. \tag{3.58}$$

3.D Inversion details

We begin with an assumed initial distribution of the moduli G_c, and a set of M_ω frequencies, to solve the state problem (3.17) and (3.19), to obtain $k_s^{(j)}$ and $\boldsymbol{U}_s^{(j)}$. This is followed by computing the vertical displacement $\tilde{w}^{(j)}$ via (3.21), using the wavenumbers $k_s^{(j)}$ and the eigenvectors $\boldsymbol{U}_s^{(j)}$. This, in turn, allows the computation of the misfit $\tilde{w}^{(j)} - \tilde{w}_m^{(j)}$ for every sensor for which measurements have been collected. The next step is solving the adjoint problem (3.31) for each frequency set to obtain the adjoint variables $\boldsymbol{\chi}_s^{(j)}$ and $\xi_s^{(j)}$. Here, we use the already obtained misfit and the state variables $(k_s^{(j)}, \boldsymbol{U}_s^{(j)})$. A conjugate gradient approach [62] is used to update the moduli G_c, and to ensure the sufficient decrease of the objective functional at each inversion iteration, we utilize an Armijo backtracking line search. Accordingly: let $\boldsymbol{G}_k$ denote the vector of all element moduli G_c and let $\boldsymbol{g}_k = (\nabla_{\boldsymbol{G}} \mathfrak{L})_k$ denote the reduced gradient (3.37) of the Lagrangian at the k-th inversion iteration. Then, the update $\boldsymbol{G}_{k+1}$ to $\boldsymbol{G}_k$ is constructed via:

$$\boldsymbol{G}_{k+1} = \boldsymbol{G}_k + \alpha_k \boldsymbol{S}_k, \tag{3.59}$$

where α_k is a step length, and $\boldsymbol{S}_k$ denotes search direction, defined as:

$$\boldsymbol{S}_k = \begin{cases} -\boldsymbol{g}_k & , \text{for } k = 1 \\ -\boldsymbol{g}_k + \frac{\boldsymbol{g}_k \cdot \boldsymbol{g}_k}{\boldsymbol{g}_{k-1} \cdot \boldsymbol{g}_{k-1}} \boldsymbol{S}_{k-1} & , \text{for } k > 1 \end{cases} \tag{3.60}$$

No inversion is necessary for the shear modulus of the PML layer elements. Therein, we set them all equal to the shear modulus of the last element of the interior domain. The entire inversion process is summarized in Algorithm 2.

Algorithm 2 Shear moduli inversion scheme

Set iteration counter $k \leftarrow 1$
Set initial guess for shear moduli $\boldsymbol{G}$
Compute misfit $\mathfrak{F}$ ▷ Eq. (3.1)
Set convergence tolerance *tol*
Set maximum number of iterations *maxiter*
while $\mathfrak{F} > tol$ and $k < maxiter$ **do**
    Solve the state problem for $k_s^{(j)}$ and $\boldsymbol{U}_s^{(j)}$ ▷ Eqs. (3.17),(3.19)
    Solve the adjoint problem for $\boldsymbol{\chi}_s^{(j)}$ and $\xi_s^{(j)}$ ▷ Eqs. (3.31)
    Compute the discrete reduced gradient $\boldsymbol{g}_k$ ▷ Eq. (3.37)
    Compute search direction $\boldsymbol{S}_k$ ▷ Eq. (3.60)
    Choose step length α_k
    Update material properties and compute $\boldsymbol{G}_{k+1}$ ▷ Eq. (3.59)
    Compute misfit $\mathfrak{F}$ ▷ Eq. (3.1)
    $k \leftarrow k + 1$
end while

Chapter 4

Layered soil parameter estimation from a moving load [1]

4.1 Introduction

The need to characterize the near-surface soil in terms of its mechanical properties arises in various infrastructure applications. Without any prior knowledge on the site's geology, and in the presence of arbitrary spatial heterogeneity, to characterize the deposits requires probing the soil with waves that, in turn, leads to a full-fledged three-dimensional inverse medium problem. Of interest herein is the characterization of a less demanding problem, that of horizontally-layered soils. The assumption of horizontal layering, if justified by local site conditions, reduces the problem's dimensionality, since the heterogeneity is confined along the depth only. Despite the dimensionality reduction, the characterization remains a challenging problem, due to the complexities that are typical of all inverse problems.

To date, the vast majority of imaging methods for the characterization of soils (layered or not) rely on stationary, dynamic, loads; these methods include, so-called, surface methods, where imaging relies on the analysis of the

[1] Hamidreza Mashayekh, Loukas F. Kallivokas

dispersion characteristics of surface waves (Spectral Analysis of Surface Waves (SASW) [10, 74, 80], and Multichannel Analysis of Surface Waves (MASW) [58, 63]), impact methods (e.g., Falling weight Deflectometer (FWD) [33, 71, 78]), where imaging relies on the analysis of the soil's response to a suddenly applied surface load, and Full-Waveform Inversion methods, where the imaging relies on an optimization approach that seeks to match computed to measured soil responses, constrained by the partial differential equations (PDEs) governing the propagation of waves in the probed medium [21, 37].

Imaging methodologies based on moving loads, though highly desirable, are less common, partly due to the associated mathematical complexities, and partly due to difficulties with field implementation.

In this article, we discuss a new methodology for imaging layered media using moving loads. Besides site characterization, the method is also applicable to the condition assessment of pavements, where an actuator, mounted on a moving vehicle, could serve as the probing moving source (e.g., Rolling Dynamic Deflectometer (RDD) [42]). Herein, of particular interest is the characterization of sites in the proximity of rail tracks, where a passing train can serve as the moving load. Such investigations are of increasing importance in urban environments, when new construction is planned in the neighborhood of existing rail tracks, and vibration mitigation must be addressed for human comfort.

To address the characterization problem, the forward problem –the response of the layered medium to the moving load– must be tackled first. Most

of the existing literature on the forward problem pertains to a moving point load; for example, Payton [64] determined the motion of an elastic body acted upon by a moving point load by application of the dynamic Betti-Rayleigh reciprocal theorem. Barros and Luco [15] obtained the steady-state displacements and stresses within a layered viscoelastic halfspace due to a surface point load moving with constant speed. Lu and Jeng [50] derived an analytical solution for the dynamic response of a porous halfspace medium subjected to a moving point load. Honglei et al. [76] investigated the dynamic response of a poroelastic halfspace soil medium subjected to a moving point load. Zhenning et al. [9] used the direct stiffness method combined with the inverse Fourier transform to obtain the steady-state dynamic response of a layered halfspace due to a point load moving at constant speed. Grundmann and Trommer [32] considered the interaction of train, rail, and subsoil, and used the double Fourier transform to calculate the response of a layered halfspace subjected to a moving point load.

The dynamic response of a layered elastic medium under a moving line load was first studied by Dunkin [19] and Payton [65]. Barros and Luco [16] provided solutions for a layered viscoelastic halfspace subjected to a line load moving at constant speed. Lee et al. [44] used a Thin Layer method, enhanced by continued-fraction absorbing boundary conditions, to study the dynamic response of a layered halfspace subjected to time-harmonic moving line loads. Zhenning et al. [8] used the dynamic stiffness method combined with the inverse Fourier transform to develop the dynamic 2.5D Green's func-

tions for a layered halfspace under a moving line load. Yang [81] investigated different frequency contents of moving loads at different speeds and considered the wavenumber-frequency content of train load. Yet, others used different FEM/BEM methods to determine the dynamic response of transversely isotropic soils subjected to train loads [13, 26, 28, 29, 45, 75].

Here, to address the forward problem, we choose the Thin Layer method [39], owing to dimensionality reduction it affords us. To image the layered medium, i.e., to address the associated inverse medium problem, we borrow from PDE-constrained optimization ideas [2, 11, 37], but instead of constraining the search for the properties of the medium that minimize the difference between computed and measured responses with the governing PDEs, we use the medium's dispersion relation as a constraint. The latter, as will be shown, is a natural choice given the selection of the Thin Layer method for the underlying forward problem. The foundations of the dispersion-constrained imaging, when the probing source is stationary, have been laid in a recent article [55]; however, the extension to the moving load requires modifications, which we highlight herein. Numerical results, based on synthetic data, demonstrate the applicability of the method.

4.2 Problem assumptions

Let us consider the linear elastic layered soil profile depicted in Fig. 4.1, consisting of n horizontal layers, terminated at a fixed boundary (at $z = z_n$). Each physical layer i is characterized by its thickness h_i, mass density ρ_i, and

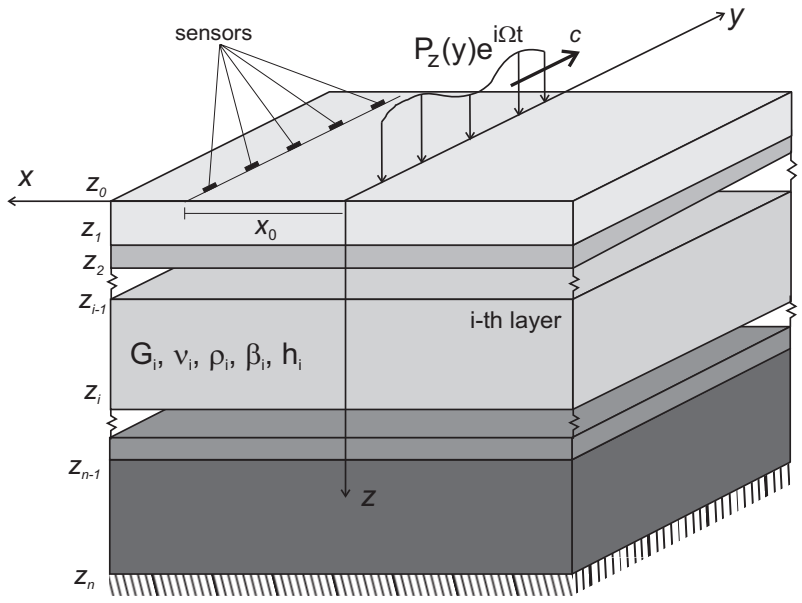

Figure 4.1: Layered soil subjected to a moving train load

a pair of elastic parameters: here, we use the shear modulus G_i, and Poisson's ratio ν_i.

The soil deposits are subjected to a dynamic train load, which moves at a constant speed c (Fig. 4.1). The train load is idealized as a dynamic line load of finite length: it is applied vertically along the z axis, on the $z = 0$ surface, and extends along the y axis. Without loss of generality, we assume that the load is harmonic at an operating frequency Ω. The load distribution along the y axis depends on a number of parameters, which, among others, include the number and configuration of the train engine(s) and railcars, the wheel spacing, the railcar length, the rail track type, the railroad tie spacing, the soil compliance, etc. An often-used approximation (e.g., [81]) for the stationary

train load is derived based on the simplifying assumptions that each wheel axle applies a point load on the track, and that the rail track behaves as an Euler-Bernoulli beam with flexural rigidity EI, resting on a Winkler foundation of distributed stiffness s. Accordingly, the vertical load distribution $q(y)$ on the rail, due to a single stationary wheel load is [81]:

$$q(y) = \frac{W_{\text{axle}}}{2\alpha} e^{-\frac{|y|}{\alpha}} \left[\cos\left(\frac{|y|}{\alpha}\right) + \sin\left(\frac{|y|}{\alpha}\right) \right], \tag{4.1}$$

where W_{axle} is the magnitude of the single axle load, and α is a characteristic length defined as $\alpha = \sqrt[4]{\frac{4EI}{s}}$. We further assume that: a) the train consists of N_r identical railcars, each of length L; b) the wheel axle spacing within each wheel assembly is a; and c) the wheel assemblies are $a + b$ apart (center-to-center) (Fig. 4.2). With these assumptions in mind, the stationary train load (total length $N_r L$) can be expressed as:

$$P_z(y) = \sum_{n=0}^{N_r-1} \Big[q(y-nL) + q(y-nL-a) + q(y-nL-a-b) + q(y-nL-2a-b) \Big]. \tag{4.2}$$

When the train is moving at a constant speed of c, then $y \to y - ct$, and the surface traction $\tilde{\sigma}_z$, with respect to a fixed reference frame, can be expressed as:

$$\tilde{\sigma}_z(x, y, t) = \delta(x) P_z(y - ct) e^{i\Omega t}, \tag{4.3}$$

where the harmonic factor $e^{i\Omega t}$ has been included to account for the dynamic behavior of the moving load.

A number of N_s sensors is deployed parallel to the rail track, at a distance of x_0 from the track (Fig. 4.1). Each sensor records the vertical com-

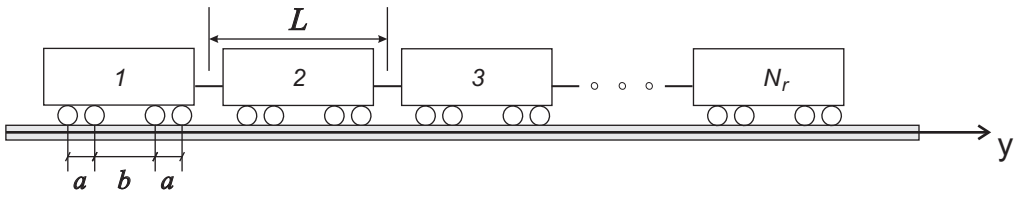

Figure 4.2: Typical train and railcar configuration

ponent of the surface displacement $\tilde{w}(x_0, y, t)$ as the train passes by[2]. Then, the goal is to estimate the layered soil properties, using the sensor data. To this end, we assume further that of the three material parameters per layer (G_i, ν_i, ρ_i), the mass density ρ_i and Poisson's ratio ν_i are *a priori* known, leaving the shear modulus G_i as the only unknown material property per layer. For soils, the assumption of prior knowledge of the elastic moduli cannot be justified; here, for simplicity, we make the aforementioned assumption in order to delineate the method. We note though that the method is applicable, with minor modifications, even when all material properties are treated as unknown. In the latter case, the computational complexity is not affected, but the ill-posedness of the associated inverse problem is aggravated, requiring the enlisting of suitable regularization schemes to alleviate it. We also note that the layer thicknesses h_i are not treated as unknowns, since they need not be recovered explicitly: upon inverting for the discrete shear moduli associated with the discretization elements, the individual layer thicknesses h_i and the layer moduli G_i are determined indirectly by lumping together adjacent

[2]In general, a three-component geophone would be recording all three displacement components; in such a case, all three components could be accommodated, to advantage, by the methodology presented herein

near-valued element moduli.

To invert for the shear moduli using the sensor records, we appeal to the recently developed dispersion-constrained full-waveform method [55], with suitable modifications. Specifically: using the recorded data, it is possible to construct a misfit functional between computed sensor data that are based on a trial shear-modulus profile for the layered medium, and the measured data. Then, we form a Lagrangian, by side-imposing to the misfit functional the dispersion relation of the trial medium. Minimization of the Lagrangian would then imply that the misfit is minimized (thereby matching the measured data to the computed), while simultaneously satisfying the dispersion relation; these lines of investigation are similar to inverse-medium, full-waveform, PDE-constrained problems [2, 20, 21].

The dispersion-constrained approach we follow was first discussed in [55] for stationary loads; here, the key difficulty stems from the moving character of the applied load. To fix ideas, we discuss next the modifications the presence of the moving load imparts on the forward problem, which is at the heart of the inversion scheme. As in [55], among all possible choices for describing the forward problem, we choose the associated eigenvalue problem, i.e., the medium's dispersion relation.

4.3 The forward eigenvalue problem

Application of a Fourier transform[3] $\mathcal{F}_t$ in time to the standard equations of equilibrium for a linear elastic solid yields the following equations written in the frequency domain for the i-th layer:

$$\frac{\partial \hat{\hat{\sigma}}_x}{\partial x} + \frac{\partial \hat{\hat{\tau}}_{xy}}{\partial y} + \frac{\partial \hat{\hat{\tau}}_{xz}}{\partial z} = -\rho_i \omega^2 \hat{\hat{u}} \tag{4.4a}$$

$$\frac{\partial \hat{\hat{\tau}}_{xy}}{\partial x} + \frac{\partial \hat{\hat{\sigma}}_y}{\partial y} + \frac{\partial \hat{\hat{\tau}}_{yz}}{\partial z} = -\rho_i \omega^2 \hat{\hat{v}} \tag{4.4b}$$

$$\frac{\partial \hat{\hat{\tau}}_{xz}}{\partial x} + \frac{\partial \hat{\hat{\tau}}_{yz}}{\partial y} + \frac{\partial \hat{\hat{\sigma}}_z}{\partial z} = -\rho_i \omega^2 \hat{\hat{w}}, \tag{4.4c}$$

where quantities marked with ($\hat{\hat{\cdot}}$) denote displacements and stresses in the frequency domain; for example, the normal stress $\hat{\hat{\sigma}}_z \equiv \hat{\hat{\sigma}}_z(x, y, z; \omega)$, where ω is frequency, and, otherwise, customary notation is used for the displacement vector and stress tensor components. Inserting the constitutive law and kinematic conditions in (4.4), the equations of motion for each layer, in the frequency domain, become:

$$G_i[\frac{\partial^2 \hat{\hat{u}}}{\partial x^2} + \frac{\partial^2 \hat{\hat{u}}}{\partial y^2} + \frac{\partial^2 \hat{\hat{u}}}{\partial z^2}] + (\lambda_i + G_i)[\frac{\partial^2 \hat{\hat{u}}}{\partial x^2} + \frac{\partial^2 \hat{\hat{v}}}{\partial x \partial y} + \frac{\partial^2 \hat{\hat{w}}}{\partial x \partial z}] + \rho_i \omega^2 \hat{\hat{u}} = 0 \tag{4.5a}$$

$$G_i[\frac{\partial^2 \hat{\hat{v}}}{\partial x^2} + \frac{\partial^2 \hat{\hat{v}}}{\partial y^2} + \frac{\partial^2 \hat{\hat{v}}}{\partial z^2}] + (\lambda_i + G_i)[\frac{\partial^2 \hat{\hat{u}}}{\partial x \partial y} + \frac{\partial^2 \hat{\hat{v}}}{\partial y^2} + \frac{\partial^2 \hat{\hat{w}}}{\partial y \partial z}] + \rho_i \omega^2 \hat{\hat{v}} = 0 \tag{4.5b}$$

$$G_i[\frac{\partial^2 \hat{\hat{w}}}{\partial x^2} + \frac{\partial^2 \hat{\hat{w}}}{\partial y^2} + \frac{\partial^2 \hat{\hat{w}}}{\partial z^2}] + (\lambda_i + G_i)[\frac{\partial^2 \hat{\hat{u}}}{\partial x \partial z} + \frac{\partial^2 \hat{\hat{v}}}{\partial y \partial z} + \frac{\partial^2 \hat{\hat{w}}}{\partial z^2}] + \rho_i \omega^2 \hat{\hat{w}} = 0, \tag{4.5c}$$

[3]Throughout, we use $\mathcal{F}_\tau\{f(\tau)\} = \hat{f}(\eta) = \int_{-\infty}^{\infty} f(\tau) e^{-i\eta\tau} d\tau$, to denote the Fourier transform of $f(\tau)$, where τ and η are the dual transform variables.

where λ_i denotes the first Lamé constant for the i-th layer. Next, following the Thin Layer method concepts [39], the governing equations of motion (4.5) are doubly Fourier-transformed in space ($\mathcal{F}_x\mathcal{F}_y$), with respect to x and y, respectively, to yield:

$$k_x^2(\lambda_i + 2G_i)u + k_y^2 G_i u + k_x k_y(\lambda_i + G_i)v - ik_x(\lambda_i + G_i)\frac{dw}{dz} - G_i\frac{d^2u}{dz^2} - \rho_i\omega^2 u = 0 \quad (4.6a)$$

$$k_y^2(\lambda_i + 2G_i)v + k_x^2 G_i v + k_x k_y(\lambda_i + G_i)u - ik_y(\lambda_i + G_i)\frac{dw}{dz} - G_i\frac{d^2v}{dz^2} - \rho_i\omega^2 v = 0 \quad (4.6b)$$

$$k_x^2 G_i w + k_y^2 G_i w - (\lambda_i + 2G_i)\frac{d^2w}{dz^2} - ik_x(\lambda_i + G_i)\frac{du}{dz} - ik_y(\lambda_i + G_i)\frac{dv}{dz} - \rho_i\omega^2 w = 0 \quad (4.6c)$$

where, k_x and k_y denote spatial wavenumbers, dual to x and y, respectively, and, for example, the displacement component along x is $u \equiv u(z; k_x, k_y, \omega)$, i.e., the displacement components depend only on the depth z. Next, we multiply (4.6) by test functions $\check{u}, \check{v}, \check{w}$, and integrate by parts, to obtain the

following weak form of the equations of motion for each layer:

$$
\begin{aligned}
&k_x^2(\lambda_i+2G_i)\int_{z_{i-1}}^{z_i} u\check{u}dz + k_y^2 G_i\int_{z_{i-1}}^{z_i} u\check{u}dz + k_xk_y(\lambda_i+G_i)\int_{z_{i-1}}^{z_i} v\check{u}dz \\
&- ik_x\lambda_i\int_{z_{i-1}}^{z_i}\frac{dw}{dz}\check{u}dz + ik_xG_i\int_{z_{i-1}}^{z_i} w\frac{d\check{u}}{dz}dz + G_i\int_{z_{i-1}}^{z_i}\frac{du}{dz}\frac{d\check{u}}{dz}dz \\
&- \rho_i\omega^2\int_{z_{i-1}}^{z_i} u\check{u}dz = \tau_{xz}\,\check{u}\,\Big|_{z_{i-1}}^{z_i}
\end{aligned}
\tag{4.7a}
$$

$$
\begin{aligned}
&k_y^2(\lambda_i+2G_i)\int_{z_{i-1}}^{z_i} v\check{v}dz + k_x^2 G_i\int_{z_{i-1}}^{z_i} v\check{v}dz + k_xk_y(\lambda_i+G_i)\int_{z_{i-1}}^{z_i} u\check{v}dz \\
&- ik_y\lambda_i\int_{z_{i-1}}^{z_i}\frac{dw}{dz}\check{v}dz + ik_yG_i\int_{z_{i-1}}^{z_i} w\frac{d\check{v}}{dz}dz + G_i\int_{z_{i-1}}^{z_i}\frac{dv}{dz}\frac{d\check{v}}{dz}dz \\
&- \rho_i\omega^2\int_{z_{i-1}}^{z_i} v\check{v}dz = \tau_{yz}\,\check{v}\,\Big|_{z_{i-1}}^{z_i}
\end{aligned}
\tag{4.7b}
$$

$$
\begin{aligned}
&k_x^2 G_i\int_{z_{i-1}}^{z_i} w\check{w}dz + k_y^2 G_i\int_{z_{i-1}}^{z_i} w\check{w}dz + (\lambda_i+2G_i)\int_{z_{i-1}}^{z_i}\frac{dw}{dz}\frac{d\check{w}}{dz}dz \\
&+ ik_x\lambda_i\int_{z_{i-1}}^{z_i} u\frac{d\check{w}}{dz}dz + ik_y\lambda_i\int_{z_{i-1}}^{z_i} v\frac{d\check{w}}{dz}dz - ik_xG_i\int_{z_{i-1}}^{z_i}\frac{du}{dz}\check{w}dz \\
&- ik_yG_i\int_{z_{i-1}}^{z_i}\frac{dv}{dz}\check{w}dz - \rho_i\omega^2\int_{z_{i-1}}^{z_i} w\check{w}dz = \sigma_z\,\check{w}\,\Big|_{z_{i-1}}^{z_i}
\end{aligned}
\tag{4.7c}
$$

The solution for the surface-loaded layered medium problem can be obtained by the solution of weak forms (4.7) subject to: a) fixed conditions ($u = v = w = 0$) at z_n (Fig. 4.1); b) the continuity of displacements and tractions along the layer interfaces $z_i, i = 1, \ldots, n-1$; and, c) using definitions

(4.2) and (4.3), to the surface conditions:

$$\begin{aligned}\sigma_z(z=0;k_x,k_y,\omega)=\mathcal{F}_x\mathcal{F}_y\mathcal{F}_t\{\tilde{\sigma}_z\} &= \mathcal{F}_x\{\delta(x)\}\mathcal{F}_t\{\mathcal{F}_y\{P_z(y-ct)e^{i\Omega t}\}\} \\ &= \mathcal{F}_t\{\hat{P}_z(k_y)e^{-ik_yct}e^{i\Omega t}\} \\ &= \hat{P}_z(k_y)\ \delta[\omega-(\Omega-k_yc)], \qquad (4.8a)\end{aligned}$$

$$\tau_{xz}(z=0;k_x,k_y,\omega)=0, \qquad (4.8b)$$

$$\tau_{yz}(z=0;k_x,k_y,\omega)=0. \qquad (4.8c)$$

where,

$$\hat{P}_z(k_y)=\mathcal{F}_y\{P_z(y)\}=\frac{4W_{axle}}{4+{k_y}^4\alpha^4}\sum_{n=0}^{N_r-1}e^{-ik_ynL}\Big[1+e^{-ik_ya}+e^{-ik_y(a+b)}+e^{-ik_y(2a+b)}\Big], \qquad (4.9)$$

is the spatial Fourier transform of the (stationary) train load. We note that, as it can be seen from the presence of the Dirac function in (4.8a), the response is dominated by the spectrum of the train load (k_y): for a non-moving train ($c=0$), the response is, as expected, harmonic at the operating frequency Ω, but for a moving train, the frequency is shifted by k_yc.

Introducing standard Lagrange-family polynomial approximations for the triad of the trial functions u, v, and w, and the triad of test functions $\breve{u}$, $\breve{v}$, and $\breve{w}$, yields a linear system of equations for the unknown (triply-Fourier-transformed) displacement components:

$$(k_x^2\mathbf{A}+k_x\underbrace{(\mathbf{B}_1+\mathbf{B}_2)}_{\mathbf{B}}+\underbrace{(\mathbf{G}_1+\mathbf{G}_2+\mathbf{G}_3)-(\Omega-k_yc)^2\mathbf{M}}_{\mathbf{C}})\boldsymbol{U}=\boldsymbol{P},\quad \boldsymbol{U}=\begin{bmatrix}-i\boldsymbol{u}\\-i\boldsymbol{v}\\\boldsymbol{w}\end{bmatrix}, \qquad (4.10)$$

where, $\boldsymbol{u}$, $\boldsymbol{v}$, and $\boldsymbol{w}$ are vectors of nodal components of displacements in the x, y, and z directions, respectively, $\boldsymbol{P}$ is the load vector, and the various matrices are defined as:

$$\mathcal{A}_i = \begin{bmatrix} (\lambda_i + 2G_i) \int_{z_{i-1}}^{z_i} \boldsymbol{\phi}\boldsymbol{\phi}^T & 0 & 0 \\ 0 & G_i \int_{z_{i-1}}^{z_i} \boldsymbol{\phi}\boldsymbol{\phi}^T & 0 \\ 0 & 0 & G_i \int_{z_{i-1}}^{z_i} \boldsymbol{\phi}\boldsymbol{\phi}^T \end{bmatrix}, \tag{4.11a}$$

$$\mathcal{B}_{1i} = \begin{bmatrix} 0 & 0 & -\lambda_i \int_{z_{i-1}}^{z_i} \boldsymbol{\phi}\boldsymbol{\phi}'^T + G_i \int_{z_{i-1}}^{z_i} \boldsymbol{\phi}'\boldsymbol{\phi}^T \\ 0 & 0 & 0 \\ -\lambda_i \int_{z_{i-1}}^{z_i} \boldsymbol{\phi}'\boldsymbol{\phi}^T + G_i \int_{z_{i-1}}^{z_i} \boldsymbol{\phi}\boldsymbol{\phi}'^T & 0 & 0 \end{bmatrix}, \tag{4.11b}$$

$$\mathcal{B}_{2i} = k_y \begin{bmatrix} 0 & (\lambda_i + G_i) \int_{z_{i-1}}^{z_i} \boldsymbol{\phi}\boldsymbol{\phi}^T & 0 \\ (\lambda_i + G_i) \int_{z_{i-1}}^{z_i} \boldsymbol{\phi}\boldsymbol{\phi}^T & 0 & 0 \\ 0 & 0 & 0 \end{bmatrix}, \tag{4.11c}$$

$$\mathcal{G}_{1i} = \begin{bmatrix} G_i \int_{z_{i-1}}^{z_i} \boldsymbol{\phi}'\boldsymbol{\phi}'^T & 0 & 0 \\ 0 & G_i \int_{z_{i-1}}^{z_i} \boldsymbol{\phi}'\boldsymbol{\phi}'^T & 0 \\ 0 & 0 & (\lambda_i + 2G_i) \int_{z_{i-1}}^{z_i} \boldsymbol{\phi}'\boldsymbol{\phi}'^T \end{bmatrix}, \tag{4.11d}$$

$$\mathcal{G}_{2i} = k_y \begin{bmatrix} 0 & 0 & 0 \\ 0 & 0 & -\lambda_i \int_{z_{i-1}}^{z_i} \boldsymbol{\phi}\boldsymbol{\phi}'^T + G_i \int_{z_{i-1}}^{z_i} \boldsymbol{\phi}'\boldsymbol{\phi}^T \\ 0 & -\lambda_i \int_{z_{i-1}}^{z_i} \boldsymbol{\phi}'\boldsymbol{\phi}^T + G_i \int_{z_{i-1}}^{z_i} \boldsymbol{\phi}\boldsymbol{\phi}'^T & 0 \end{bmatrix}, \tag{4.11e}$$

$$\mathcal{G}_{3i} = k_y^2 \begin{bmatrix} G_i \int_{z_{i-1}}^{z_i} \boldsymbol{\phi}\boldsymbol{\phi}^T & 0 & 0 \\ 0 & (\lambda_i + 2G_i) \int_{z_{i-1}}^{z_i} \boldsymbol{\phi}\boldsymbol{\phi}^T & 0 \\ 0 & 0 & G_i \int_{z_{i-1}}^{z_i} \boldsymbol{\phi}\boldsymbol{\phi}^T \end{bmatrix}, \tag{4.11f}$$

$$\mathcal{M}_i = \begin{bmatrix} \rho_i \int_{z_{i-1}}^{z_i} \boldsymbol{\phi}\boldsymbol{\phi}^T & 0 & 0 \\ 0 & \rho_i \int_{z_{i-1}}^{z_i} \boldsymbol{\phi}\boldsymbol{\phi}^T & 0 \\ 0 & 0 & \rho_i \int_{z_{i-1}}^{z_i} \boldsymbol{\phi}\boldsymbol{\phi}^T \end{bmatrix}. \tag{4.11g}$$

For a train load moving at a speed c, the k_y wavenumbers are obtained from the load's spectrum by application of the Fourier transform along y; then, the apparent frequency $\Omega - k_y c$ is known, and provided that the horizontal wavenumbers k_x are obtained, a solution can be rendered for the displacement components in the wavenumber-frequency space. To resolve the k_x wavenum-

bers, we turn to the eigenvalue problem, defined similarly to (4.10) as:

$$(k_x^2\mathbf{A} + k_x\mathbf{B} + \mathbf{C})\,\boldsymbol{U} = \mathbf{0}. \tag{4.12}$$

If k_x is an eigenvalue satisfying the quadratic eigenvalue problem (4.12), then, due to the specific structure of the involved matrices, it can be shown that $-k_x$ is also an eigenvalue [55]. Thus, for N total degrees-of-freedom, (4.12) admits $2N$ eigenvalues in the form of N pairs $(k_x, -k_x)$. Not all of the, generally complex, k_x are admissible, as shown in [55]: only the wavenumbers for which $\Im m(k_x) > 0$ are retained, since only these wavenumbers satisfy the radiation and boundedness conditions at infinity. The N surviving wavenumbers/eigenvalues are associated with N eigenvectors, for which we use the following normalization, borrowing from the one adopted by Kausel [39] and Waas [79]:

$$\frac{1}{2}\boldsymbol{U}_s^T(2k_{x,s}\mathbf{A} + \mathbf{B})\boldsymbol{U}_s = k_{x,s}\ , \qquad s = 1, 2, ..., N, \tag{4.13}$$

where s denotes the s-th mode. Then, following Kausel [39], the expression for the vertical displacement component on the surface ($z = 0$), and at any distance x from the rail track, becomes:

$$w(x, k_y, \Omega - k_y c) = \hat{P}_z(k_y)\sum_{s=1}^{N}(U_{s,\frac{2N}{3}+1})^2\frac{1}{2\boldsymbol{i}k_{x,s}}e^{-ik_{x,s}x}. \tag{4.14}$$

Dividing throughout by the load $\hat{P}_z$, equation (4.14) can be rewritten as:

$$\Psi(x, k_y, \Omega - k_y c) = \frac{w(x, k_y, \Omega - k_y c)}{\hat{P}_z(k_y)} = \sum_{s=1}^{N}(U_{s,\frac{2N}{3}+1})^2\frac{1}{2\boldsymbol{i}k_{x,s}}e^{-ik_{x,s}x}. \tag{4.15}$$

In effect, Ψ in (4.15) is the Green's function of a layered medium subjected to a moving load of known distribution in the y direction (in the doubly Fourier-transformed space). The Green's function Ψ, as it will be discussed next,

is used in defining the misfit functional between measured (sensor data) and computed responses, instead of the vertical displacement component.

4.4 The full-waveform inversion problem

The inversion process for a moving load borrows from a similar process developed earlier for a stationary disc load [55], with a few notable modifications. A first step, and a first difference, involves the definition of the misfit functional. The standard approach is to define the misfit based on the normed difference between measured and computed responses, the latter obtained for trial distributions of the unknown shear moduli. Instead, here we opt to define the functional based on the medium's Green's function, thus presenting the optimizer with smoother functions than those provided by the displacements: the spectrum of the displacement response (w) follows closely that of the load ($\hat{P}_z$), and they are both non-smooth. By contrast, the Green's function, as will be shown in the next section, is fairly smooth. Accordingly, let the misfit functional $\mathfrak{F}$ be defined as:

$$\mathfrak{F} = \frac{1}{2} \sum_{i=1}^{N_{k_y}} \left| \Psi(x_0, k_y^{(i)}, \Omega - k_y^{(i)} c) - \Psi_m(x_0, k_y^{(i)}, \Omega - k_y^{(i)} c) \right|^2 , \tag{4.16}$$

where, N_{k_y} is the total number of k_y wavenumbers from the discrete load spectrum ($k_y^{(i)}$ denotes the i-th wavenumber in the N_{k_y} set). A successful minimization of the misfit (4.16) would lead to the sought shear-modulus profile. The minimization is constrained by the underlying physical behavior, which we choose to represent here (as in [55]) by the problem's dispersion relation, or

equivalently, by the eigenvalue problem. Accordingly, to construct the problem's Lagrangian, we side-impose to the misfit $\mathfrak{F}$, via Lagrange multipliers, the discrete eigenvalue problem; there results:

$$\begin{aligned}\mathfrak{L} =&\frac{1}{2}\sum_{i=1}^{N_{k_y}}\left|\Psi(x_0,k_y^{(i)},\Omega-k_y^{(i)}c)-\Psi_m(x_0,k_y^{(i)},\Omega-k_y^{(i)}c)\right|^2+\\ &\Re e\Big\{\sum_{i=1}^{N_{k_y}}\sum_{s=1}^{N}\boldsymbol{\chi}_s^{(i)^T}(\mathbf{A}{k_{x,s}^{(i)}}^2+\mathbf{B}^{(i)}k_{x,s}^{(i)}+\mathbf{C}^{(i)})\boldsymbol{U}_s^{(i)}\\ &+\sum_{i=1}^{N_{k_y}}\sum_{s=1}^{N}\xi_s^{(i)}\Big(\frac{1}{2}\boldsymbol{U}_s^{(i)^T}(2\mathbf{A}k_{x,s}^{(i)}+\mathbf{B}^{(i)})\boldsymbol{U}_s^{(i)}-k_{x,s}^{(i)}\Big)\Big\}\,,\end{aligned}\tag{4.17}$$

where $\boldsymbol{\chi}_s^{(i)}$ is a vector of Lagrange multipliers used to side-impose the eigenvalue problem (4.12), and $\xi_s^{(i)}$ is a scalar used to side-impose the orthonormality condition (4.13).

4.4.1 Optimality conditions

Similar to the stationary load case [55], the first variations of $\mathfrak{L}$ with respect to: a) the state variables $k_{x,s}^{(i)}$, $\boldsymbol{U}_s^{(i)}$; b) the Lagrange multipliers $\boldsymbol{\chi}_s^{(i)}$, $\xi_s^{(i)}$; and c) the unknown, discrete element, shear moduli G_c, must vanish. The vanishing of the first variation with respect to the Lagrange multipliers recovers the forward eigenvalue problem and the orthonormality condition. Similarly, the first variation with respect to the state variables returns the adjoint problem:

$$\begin{aligned}&\delta_{\boldsymbol{U}_s^{(i)}}\mathfrak{L}=0\rightarrow\\ &\quad(\mathbf{A}{k_{x,s}^{(i)}}^2+\mathbf{B}^{(i)}k_{x,s}^{(i)}+\mathbf{C}^{(i)})^T\boldsymbol{\chi}_s^{(i)}+(2\mathbf{A}k_{x,s}^{(i)}+\mathbf{B}^{(i)})\boldsymbol{U}_s^{(i)}\xi_s^{(i)}\\ &\qquad=-(\overline{\Psi^{(i)}-\Psi_m^{(i)}})U^{(i)}_{s,\frac{2N}{3}+1}\frac{1}{\boldsymbol{i}k_{x,s}^{(i)}}e^{-ik_{x,s}^{(i)}x_0}\,\boldsymbol{W}_I,\end{aligned}\tag{4.18}$$

and,

$$\begin{aligned}\delta_{k_{x,s}^{(i)}}\mathfrak{L} = 0 \rightarrow \\ \boldsymbol{U}_s^{(i)^T}(2\mathbf{A}k_{x,s}^{(i)} + \mathbf{B}^{(i)})^T\boldsymbol{\chi}_s^{(i)} + (\boldsymbol{U}_s^{(i)^T}\mathbf{A}\boldsymbol{U}_s^{(i)} - 1)\xi_s^{(i)} \\ = -(\overline{\Psi^{(i)} - \Psi_m^{(i)}})(U_{s,\frac{2N}{3}+1}^{(i)})^2\frac{\boldsymbol{i} - k_{x,s}^{(i)}x_0}{{k_{x,s}^{(i)}}^2}e^{-ik_{x,s}^{(i)}x_0}\end{aligned} \tag{4.19}$$

where, $\boldsymbol{W}_I = \left[\underbrace{0,\ldots\ldots,0,}_{2N/3}1,0,\ldots 0\right]^T$, and the i-th computed and measured Green's functions are denoted by $\Psi^{(i)} = \Psi(x_0, k_y^{(i)}, \Omega - k_y^{(i)}c)$ and $\Psi_m^{(i)} = \Psi_m(x_0, k_y^{(i)}, \Omega - k_y^{(i)}c)$, respectively. We note that the adjoint problem is a system of linear equations (and not an eigenvalue problem), driven by the misfit of the Green's functions.

Lastly, the control problem results from the vanishing of the first variation with respect to the unknown shear moduli G_c, where the latter are defined as piecewise constant over every element of the discretization:

$$\begin{aligned}\delta_{G_c}\mathfrak{L} = (\nabla_{G_c}\mathfrak{L})\ \delta G_c = \Re e\Bigg\{\sum_{i=1}^{N_k}\sum_{s=1}^{N}\boldsymbol{\chi}_s^{(i)^T}\Big(\frac{\partial\mathbf{A}}{\partial G_c}{k_{x,s}^{(i)}}^2 + \frac{\partial\mathbf{B}^{(i)}}{\partial G_c}k_{x,s}^{(i)} + \frac{\partial\mathbf{C}^{(i)}}{\partial G_c}\Big)\boldsymbol{U}_s^{(i)} \\ + \sum_{i=1}^{N_k}\sum_{s=1}^{N}\xi_s^{(i)}\Big(\frac{1}{2}\boldsymbol{U}_s^{(i)^T}\Big(2\frac{\partial\mathbf{A}}{\partial G_c}k_{x,s}^{(i)} + \frac{\partial\mathbf{B}^{(i)}}{\partial G_c}\Big)\boldsymbol{U}_s^{(i)}\Big)\Bigg\}\delta G_c\end{aligned} \tag{4.20}$$

The reduced gradient $\nabla_{G_c}\mathfrak{L}$ is used to update the shear moduli at each inversion iteration (see 4.A for details).

4.5 The inversion process

The inversion process requires preprocessing of the field-recorded data to construct the Green's function Ψ_m that corresponds to the sensor data. In

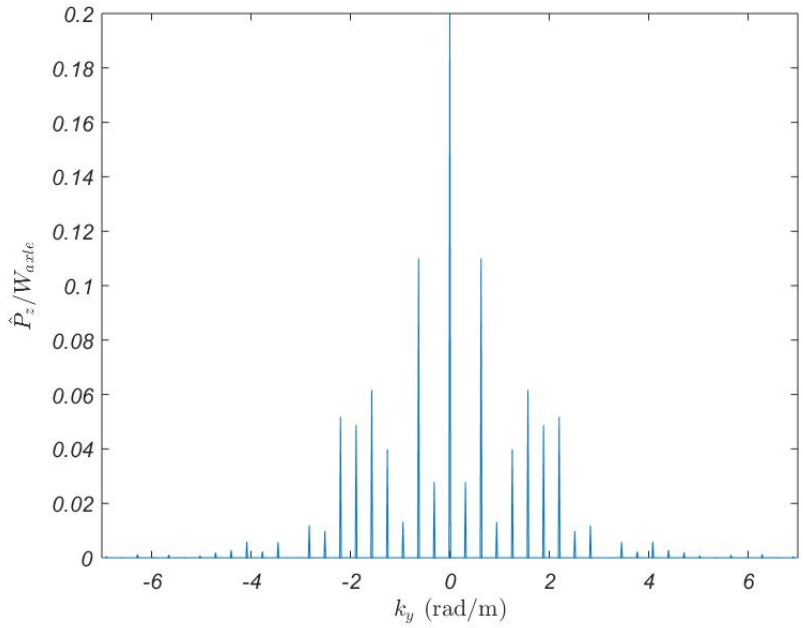

Figure 4.3: Typical Fourier transform $\mathcal{F}_y$ of a stationary static train load

turn, assuming that the train configuration, the operating frequency Ω, and the speed of the train c are known, the first step is the Fourier transform of the train load, per (4.9). For example, Fig. 4.3 shows the load spectrum for a train with $N_r = 30$ railcars, each of length $L = 20$m, wheel spacings of $a = 3$m and $b = 6$m, and a rail with relative stiffness $\alpha = 0.8$. Similarly, Fig. 4.4 shows the double spatio-temporal ($\mathcal{F}_t\mathcal{F}_y$) Fourier transform of the moving dynamic load, based on (4.8a), for an operating frequency $\Omega = 94.25$ rad/s, and four different train speeds, including the stationary train load case ($c = 0$). As it can be seen from Fig. 4.4, despite the fact that the stationary train load has only one temporal operating frequency $\Omega = 94.25$ rad/s, the moving load has

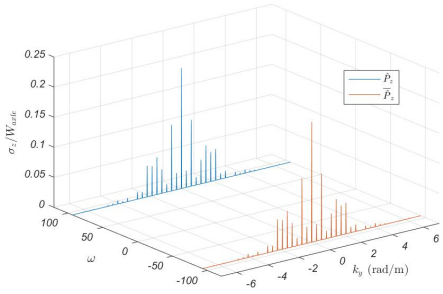

(a) Double Fourier spectrum for $c = 0$ m/s (stationary)

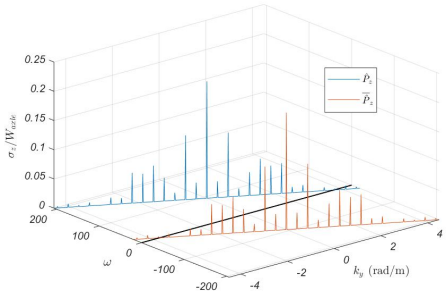

(b) Double Fourier spectrum for $c = 25$ m/s

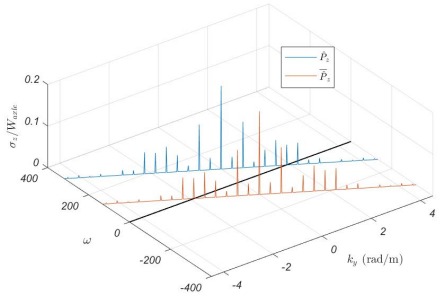

(c) Double Fourier spectrum for $c = 50$ m/s

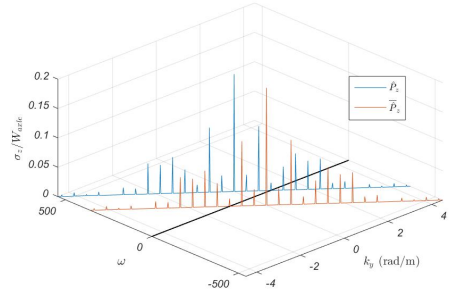

(d) Double Fourier spectrum for $c = 100$ m/s

Figure 4.4: Double spatio-temporal Fourier spectrum of train load at different speeds

a richer frequency content (ω) as a result of the train speed and the load's spectrum.

The next step involves the pre-processing of the sensor data. To illustrate, we use a three-layer stratum with the following moduli and layer-thickness distribution:

$$G = \begin{cases} 150\,\text{MPa} & 0 \leq \text{z} \leq 1\,\text{m} \\ 250\,\text{MPa} & 1 \leq \text{z} \leq 1.7\,\text{m} \\ 350\,\text{MPa} & 1.7 \leq \text{z} \leq 2.5\,\text{m} \end{cases}$$

Then, the time-domain records at N_s sensors are first time-shifted so that the record at the first sensor in the set starts at the moment when the first railcar passes by. Typical time-domain records are shown in Fig. 4.5(a). The set of the sensor time-series are then Fourier-transformed in space ($\mathcal{F}_y$) and time ($\mathcal{F}_t$) to produce the vertical displacement component $w(x_0, k_y, \omega)$ (with $\omega = \Omega - k_y c$) for a sensor line at x_0; graphically, the operation results in the spectrum shown in Fig. 4.5(b). Normalizing the spectrum of Fig. 4.5(b) with the load spectrum (Fig. 4.4(c)) results in the "measured" Green's function Ψ_m of (4.15): the latter is shown in Fig. 4.6, and, as it can be seen, the typical Ψ_m is fairly smooth. The pre-processing of the sensor data, culminating to the construction of Ψ_m, is succinctly captured in the flowchart depicted in Fig. 4.14 of 4.B.

Next, the inversion process starts with an initial guess, or trial distribution, for the shear moduli. With the moduli known, for each $k_y^{(i)}$ of the N_{k_y} wavenumbers present in the load's spectrum, the forward eigenvalue problem

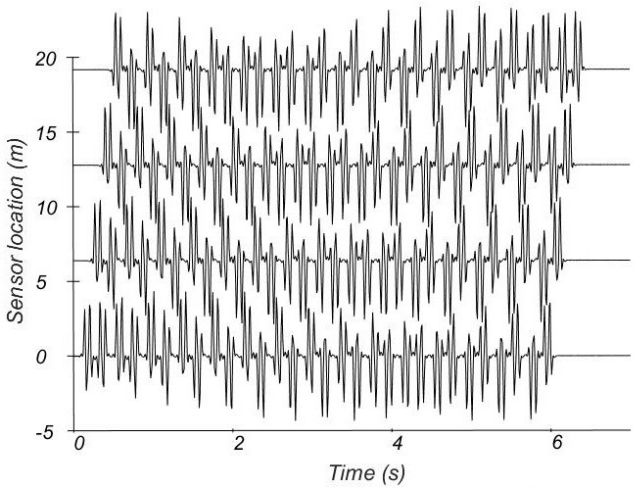

(a) Typical sensor time series

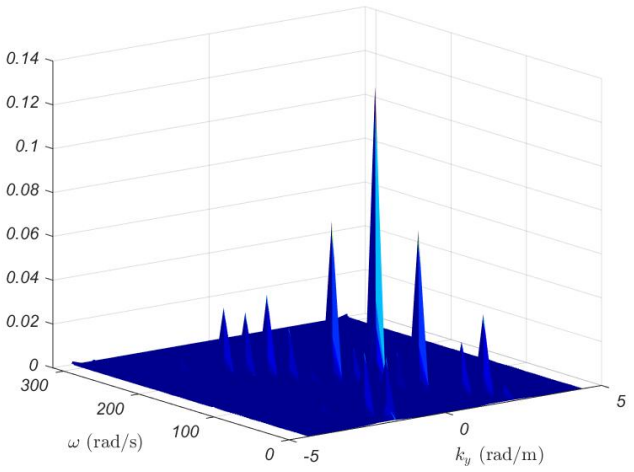

(b) Double spatio-temporal Fourier transform of sensor records along the $x = x_0$ line, parallel to the rail track

Figure 4.5: Sensor data: a) time series; and b) spatio-temporal Fourier transform

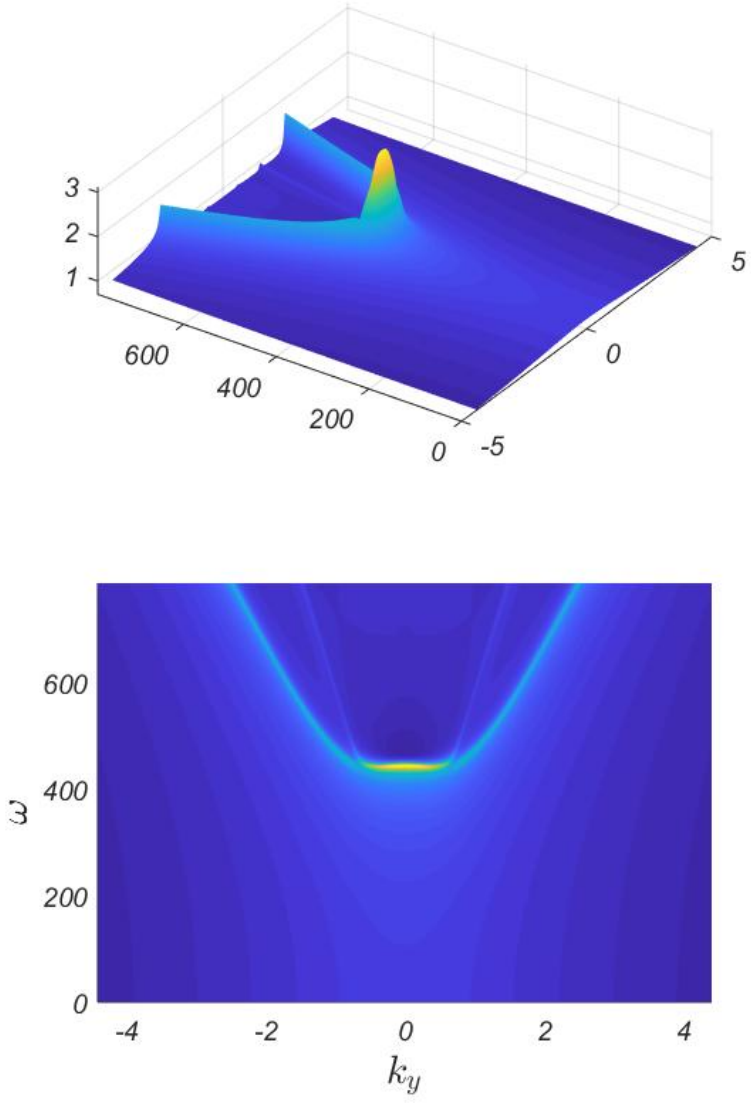

Figure 4.6: Typical measured Green's function Ψ_m

is solved, to obtain all the horizontal wavenumbers $k_x^{(i)}$ and the associated modes, from which the vertical component of the displacement (w) can be computed along the sensor line x_0, and from it, the Green's function Ψ is obtained by mere division of the displacement by the load. Repeating the process N_{k_y} times, produces the computed Green's functions Ψ that enter the misfit definition (4.16).

With the misfit known for the trial property distribution, the adjoint problem (4.18) and (4.19) is solved next, to obtain the Lagrange multipliers. With the set of state and Lagrange multipliers known, the reduced gradient can then be computed, from (4.20). The moduli are updated using the reduced gradient: any gradient-based update scheme can be used; herein, we use a conjugate gradient approach, as described in [62]. The entire process is summarized in the flowchart shown in Fig. 4.15 of 4.B.

4.6 Numerical results

We discuss next two cases, both based on synthetically-created data, to highlight the inversion process when sensors record the vertical component of the surface displacement due to a moving train load. The first case is based on the ideal setting of an infinite (or very long line) line of sensors to create a baseline for comparison. The second case resides on a smaller number of sensors, and the effect on the reconstructed profile of the shear moduli is noted. In both cases, we assumed that the train moves at a sub-critical speed (below the Rayleigh wave velocity of the top soil layer). We note that the synthetic

data have been generated while adhering to typical norms for avoiding inverse crimes, that is, the synthetic sensor data have been generated using mesh densities that are different than the mesh densities used for inversion.

4.6.1 An infinite line of sensors

We consider the three-layer stratum described in section 4.5, with mass density set to 1800 kg/m^3, and Poisson's ratio equal to 0.25 for all three layers. We also consider the same 30-car train ($\Omega = 94.25$rad/s, $L = 20$m, $N_r = 30$, $a = 3$m, $b = 6$m and $\alpha = 0.8$) described earlier in section 4.5, moving at a speed of 50m/s (or 180km/h). We use 50 quadratic elements along the depth ($N = 300$), and generate the "measured" Green's function, per (4.15). Figure 4.7 depicts the exact (modulo the discretization error) "measured" Green's function for a finely discretized k_y space (dashed line). On the same curve, the values marked by the solid circles correspond to the dominant components of the train load. Next, we use 25 quadratic elements of equal size to mesh the 2.5m-deep probed stratum. We follow the inversion process outlined in section 4.5, starting with a homogeneous initial guess for the 25 unknown moduli. The inverted profile is shown in Fig. 4.8; shown also are the initial guess, and the target (real) profile. To quantify the closeness of the inverted moduli to the target, we define the following normalized L_2-like metric:

$$\mathcal{E} = \left[\frac{\int_0^{z_n} \left[G_e(z) - G_c(z) \right]^2 dz}{\int_0^{z_n} {G_e}^2(z) dz} \right]^{0.5}, \tag{4.21}$$

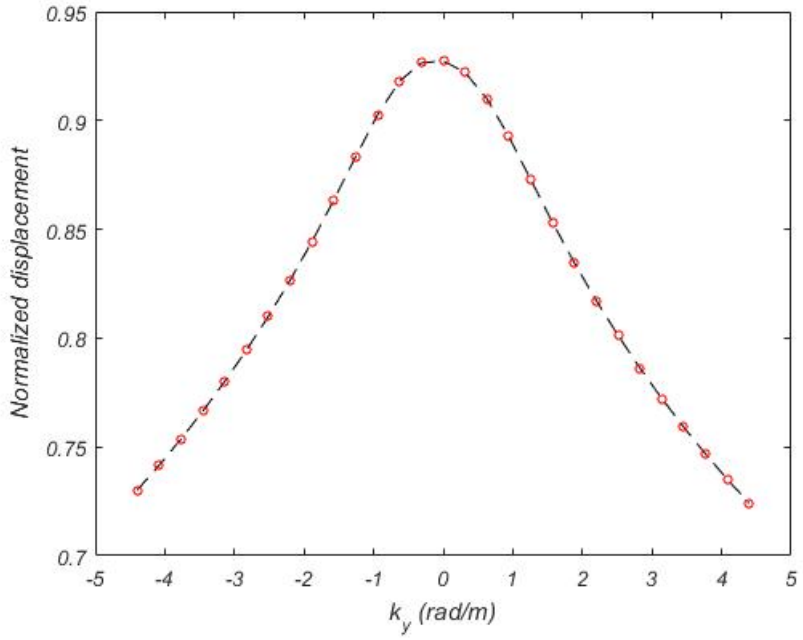

Figure 4.7: Measured Green's function for a train moving at $c = 50$m/s as a function of the train track wavenumber k_y; infinite line of sensors

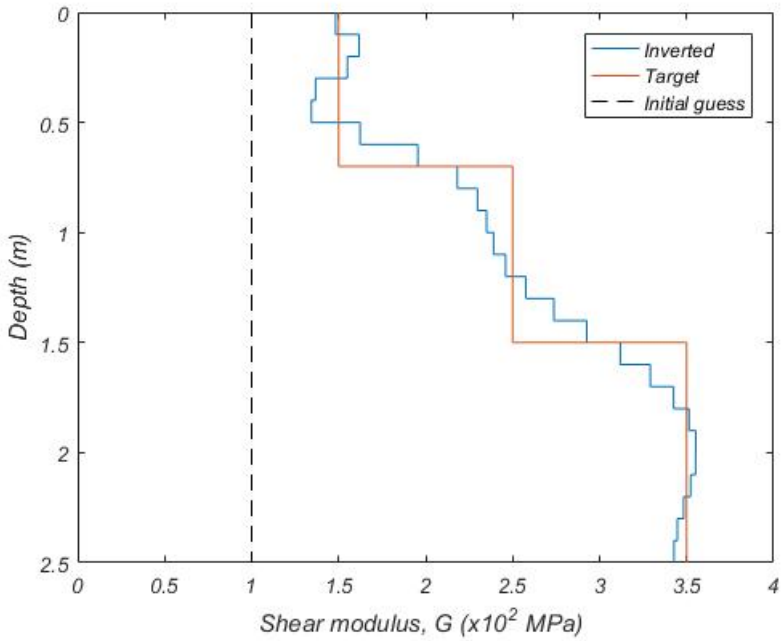

Figure 4.8: Inverted profile using an infinite line of sensors; fitness metric $\mathcal{E} = 6.9\%$

where $G_e(z)$ denotes the exact shear modulus profile, and $G_c(z)$ corresponds to the piecewise-constant distribution of the inverted-for moduli. In the case of the profile obtained with an infinite line of sensors (Fig. 4.8), the fitness metric for the inverted profile is $\mathcal{E} = 6.9\%$.

4.6.2 Real field case - finite sensor line

In practice, having an infinite, or large, number of sensors to generate the exact (or nearly exact) displacements $w_m(x_0, k_y, \Omega - k_y c)$, is not possible. However, it is still possible to drive the inversion with a finite (small) number of sensors, appropriately spaced based on *a priori* knowledge of the train's

configuration. For example, consider the spectrum of the train load depicted in Fig. 4.3, and notice again the dominant wavenumbers: it is important that they be captured in the sensor measurements. For example, if there are N_s sensors equispaced Δy apart, then the resulting wavenumbers of the discrete Fourier transform at which the motion is sampled, should be spaced $\frac{\pi}{\Delta y}$ apart. For the train load of our example, the dominant wavenumbers are

$$k_y = \pm\frac{n\pi}{10}, \quad n = 0, ..., 14$$

Therefore, with $N_s = 28$ sensors, spaced at $\Delta y = \frac{10}{14}\text{m} \approx 71\text{cm}$, the dominant wavenumbers will be captured. We note that, even if the sensors are not placed exactly at the ideal spacing dictated by the train load, the effect on the response (and the "measured" Green's function) will be tantamount to noisy data. As was shown in [55], a moderate level of noise in the data will not substantively affect the quality of the inverted profile. In short, the process is forgiving. Figure 4.9 shows the Green's function Ψ_m generated with 28 sensors (points marked with a star) along with the previously-generated exact Ψ_m.

We then use the synthetically-generated measured Green's function to drive the inversion. Figure 4.10 depicts the inverted profile; the associated fitness metric is $\mathcal{E} = 7.8\%$, only marginally different than the profile obtained using the infinite line of sensors.

4.6.3 Train configuration effect

To further demonstrate the effect that different trains (same speed, but different configuration) may have on the quality of the inversion process, we

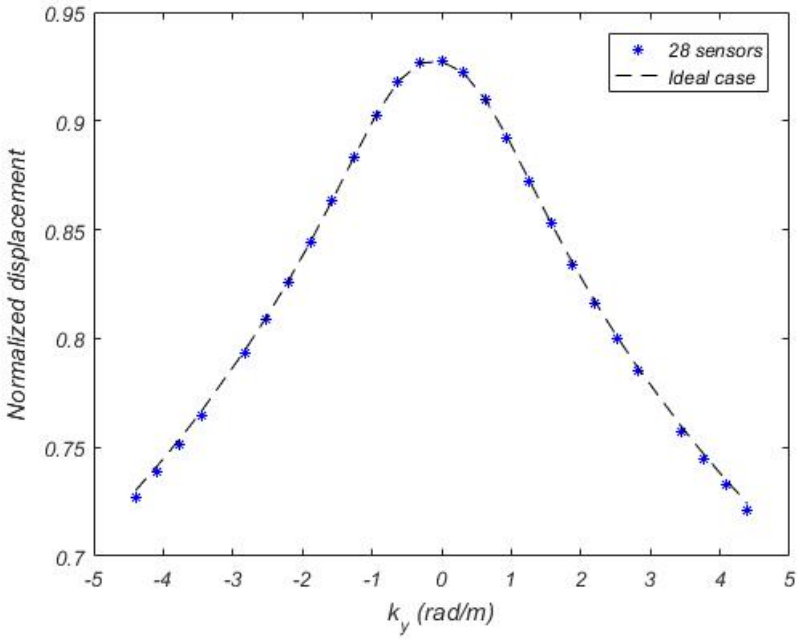

Figure 4.9: Measured Green's function for a train moving at $c = 50$m/s as a function of the train track wavenumber k_y; 28-sensor line

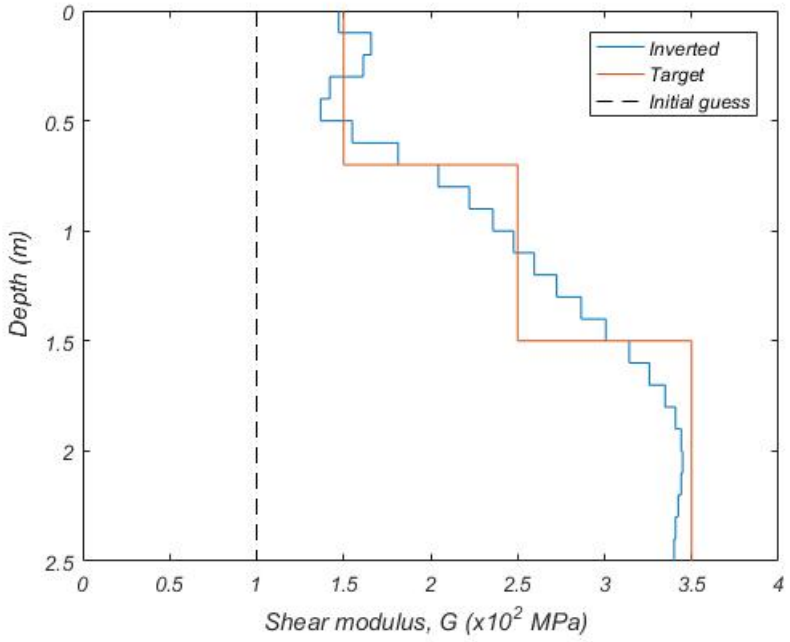

Figure 4.10: Inverted profile using 28 sensors; fitness metric $\mathcal{E} = 7.8\%$

modify the train configuration, and perform the inversion while keeping the same number of sensors. To this end, we synthetically generate the measured displacement time-series (and from those the measured Green's functions, per the process described in section 4.5) for a train with medium length ($N_r = 15$ railcars), and a train with a rather short length ($N_r = 7$ railcars). Figure 4.11 depicts the Fourier transform of the train load for the two new train configurations. As it can be seen from the figures, while the dominant wavenumbers are still present owing to the same individual railcar characteristics (compare also with Fig. 4.3), additional wavenumbers of significance appear for shorter trains. The effect can also be seen in Fig. 4.12, which shows a comparison between the exact "measured" Green's function Ψ_m, computed based on an infinite line of sensors, and the approximate Ψ_m, computed based on 28 sensors: the departure from the exact becomes more pronounced at higher wavenumbers for the shorter trains.

Next, we use the $N_r = 7$ train, with the same 28 sensors and sensor-spacing as before, to perform the inversion, thus missing the contribution of the additional wavenumbers introduced by the shorter train. The inverted-for shear modulus profile is shown in Fig. 4.13; the associated fitness metric is $\mathcal{E} = 8.5\%$. Although the fitness metric has not changed significantly when compared with the $N_r = 30$ train, we note that the inverted profile has recovered the overall trend of the shear modulus profile, but the layer interfaces are not clearly distinguishable.

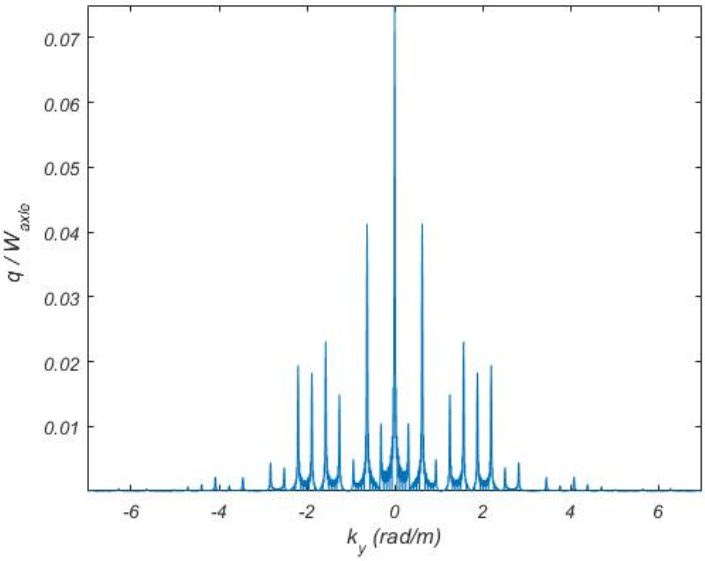

(a) N_r=15

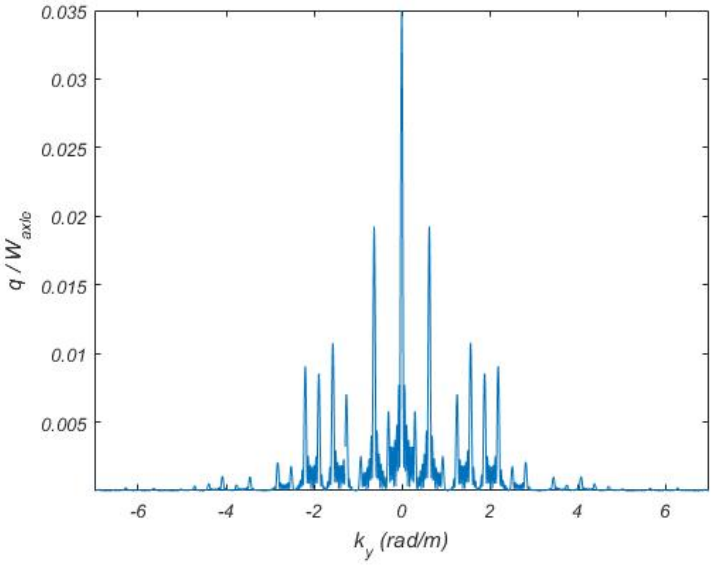

(b) N_r=7

Figure 4.11: Train load Fourier transform for different number of railcars

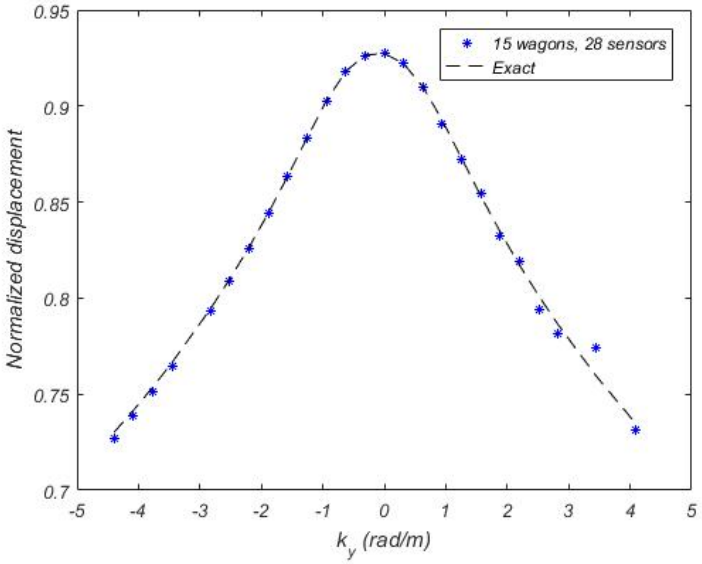

(a) N_r=15

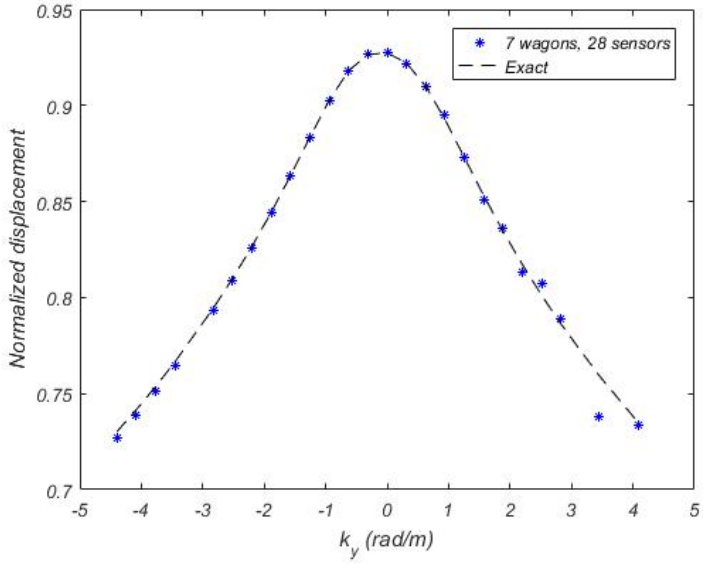

(b) N_r=7

Figure 4.12: Measured Green's function Ψ_m for two different train configurations

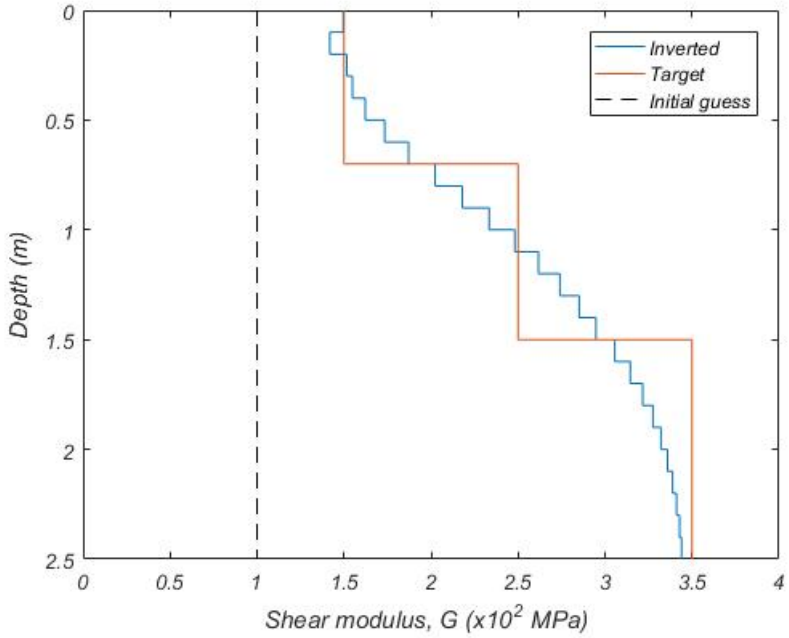

Figure 4.13: Inverted profile using 28 sensors for a train with $N_r = 7$; fitness metric $\mathcal{E} = 8.5\%$

4.7 Conclusion

We discussed a full-waveform-based approach for the characterization of layered media, when probed by a known moving load. The approach is based on a recently-developed dispersion-constrained optimization method for stationary loads, suitably modified to accommodate moving loads. We demonstrated satisfactory reconstruction of shear moduli profiles using synthetic data based on realistic field conditions. We note that it is possible to use the data collected by the passage of multiple trains to further refine the subsurface characterization. We also briefly discussed the effect the train configuration may have on the quality of the inversion, but, further parametric studies are necessary to fully assess the effect of train geometry, train speed, sensor spacing, etc, may have on the characterization: these studies will be reported in a future communication The outlined dispersion-constrained method, partly due to the dimensionality reduction to a single spatial dimension, offers a rapid and reliable platform for condition assessment and/or characterization of the near-surface deposits in the proximity of rail tracks.

4.A Shear moduli updates

To update the moduli G_c, we use a conjugate gradient approach [62], and to ensure sufficient decrease of the objective functional at each inversion iteration, we employ an Armijo backtracking line search. Accordingly: let $\boldsymbol{G}_k$ denote the vector of all element moduli G_c and let $\boldsymbol{g}_k = (\nabla_{\boldsymbol{G}}\mathfrak{L})_k$ denote the reduced gradient (4.20) of the Lagrangian at the k-th inversion iteration.

Then, the update $\boldsymbol{G}_{k+1}$ to $\boldsymbol{G}_k$ is constructed via:

$$\boldsymbol{G}_{k+1} = \boldsymbol{G}_k + \alpha_k \, \boldsymbol{s}_k, \tag{4.22}$$

where α_k is a step length, and $\boldsymbol{s}_k$ denotes search direction, defined as:

$$\boldsymbol{s}_k = \begin{cases} -\boldsymbol{g}_k & , \text{for } k = 1 \\ -\boldsymbol{g}_k + \frac{\boldsymbol{g}_k \cdot \boldsymbol{g}_k}{\boldsymbol{g}_{k-1} \cdot \boldsymbol{g}_{k-1}} \boldsymbol{s}_{k-1} & , \text{for } k > 1 \end{cases} \tag{4.23}$$

4.B Inversion process flowcharts

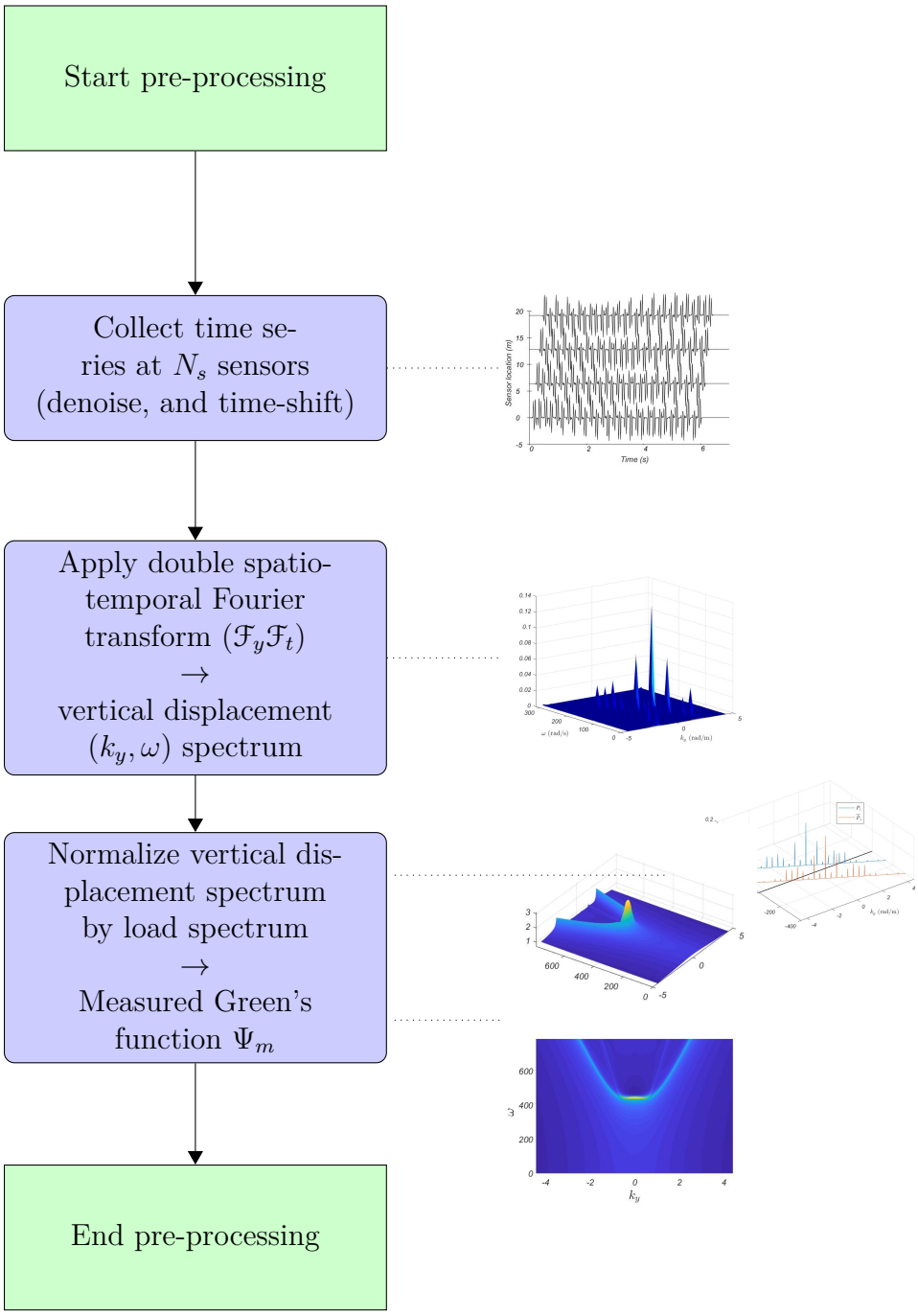

Figure 4.14: Sensor data pre-processing flowchart

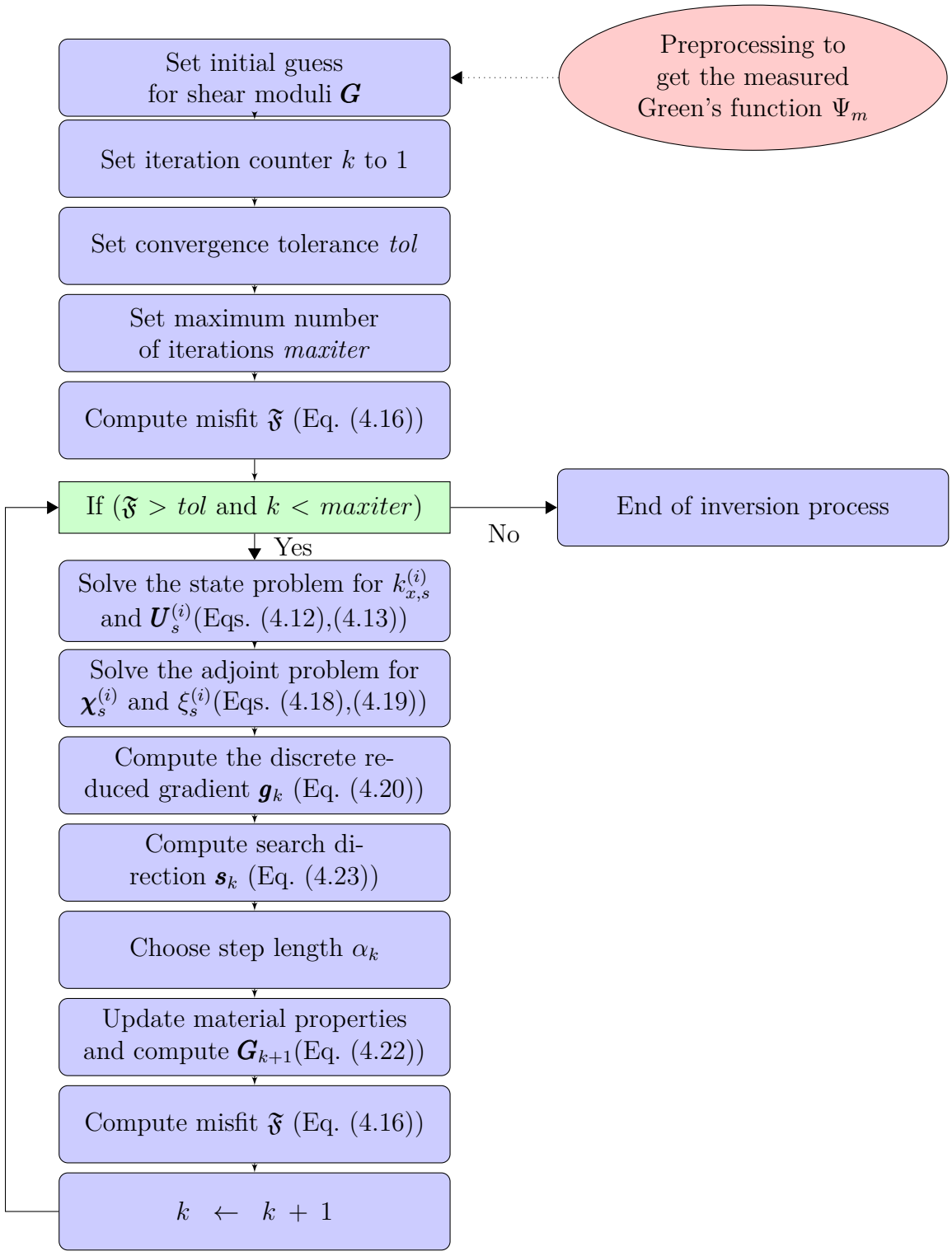

Figure 4.15: Full-waveform inversion flowchart

Chapter 5

Conclusion

5.1 Summary and contributions

In this dissertation, we discussed a new dispersion-constrained optimization approach for resolving the inverse medium problem associated with the reconstruction of the material profile of a layered medium, based on surface measurements of its response to surface excitation. The methodology is applicable to either a layered stratum or a layered halfspace subjected to dynamic stationary or moving loads. Key advantages of the methodology include: a) use is made of the complete recorded displacement waveforms, whether in the near-field or the far-field, without need for any simplifying assumptions; b) spatial discretization is needed only in one dimension–along the depth.

The reported numerical results show the method's ability to invert for the moduli, and indirectly for the thicknesses, of a layered medium. Furthermore, our computational experiments indicate that the methodology is also capable of recovering the material parameters satisfactorily in the presence of moderate noise levels in the recorded data.

5.2 Extensions

5.2.1 Regularization

We have introduced a new methodology for the full-waveform inversion, but unlike typical inversion methods, we did not use any regularization. It was noted that the coarseness of the required mesh for inversion acted indirectly, as a regularizer, making explicit regularization unnecessary. Nevertheless, adding explicit regularization will improve the capabilities of the methodology.

5.2.2 Moving load over halfspace

We have applied the dispersion-constrained inversion methodology to the case of a moving load over a layered stratum. Extending the methodology to the case of a layered halfspace subjected to a moving load is straightforward, by direct use of the criterion developed in the second paper.

5.2.3 Inversion for other material properties

We have used the inversion process to recover the shear moduli of a layered medium explicitly, and to determine the layer thicknesses implicitly. However, the methodology's framework can accommodate inversing of other properties (damping, density, Poisson's ratio) at increased computational cost.

Bibliography

[1] United States Federal Aviation Administration. *Use of nondestructive testing in the evaluation of airport pavements*. U.S. Dept. of Transportation, Federal Aviation Administration, Washington DC, 2004.

[2] V. Akçelik, G. Biros, O. Ghattas, J. Hill, D. Keyes, and B. van Bloemen Waanders. Parallel algorithms for PDE-constrained optimization. In M. Heroux, P. Raghavan, and H. Simon, editors, *Parallel Processing for Scientific Computing*, pages 291–322. SIAM, 2006.

[3] V. Akçelik, G. Biros, O. Ghattas, D. Keyes, K. Ko, L. Lee, and E.G Ng. Adjoint methods for electromagnetic shape optimization of the low-loss cavity for the international linear collider. *Journal of Physics: Conference Series*, 16(1):435–445, 2005.

[4] R. Al-Khoury, C. Kasbergen, A. Scarpas, and J. Blaauwendraad. Spectral element technique for efficient parameter identification of layered media. *International Journal of Solids and Structures*, 38(48):8753–8772, 2001.

[5] N. Ali and N. Khosla. Determination of layer moduli using a falling weight deflectometer. *Transportation Research Record*, 1117:1–10, 1987.

[6] M. Anderson. A data base method for backcalculation of composite pavement layer moduli. In *Nondestructive Testing of Pavements and Backcalculation of Moduli*, volume 1026, pages 201–216. ASTM International, 1989.

[7] A. V. Astaneh and M. N. Guddati. Improved inversion algorithms for near-surface characterization. *Geophysical Journal International*, 206(2):1410–1423, 2016.

[8] Zhenning Ba, Vincent W. Lee, Jianwen Liang, and Yan Yang. Dynamic 2.5D Green's functions for moving distributed loads acting on an inclined line in a multi-layered TI half-space. *Soil Dynamics and Earthquake Engineering*, 99:172–188, 2017.

[9] Zhenning Ba, Jianwen Liang, Vincent W. Lee, and Hang Ji. 3D dynamic response of a multi-layered transversely isotropic half-space subjected to a moving point load along a horizontal straight line with constant speed. *International Journal of Solids and Structures*, 100-101:427–445, 2016.

[10] Leo T. Brown, David M. Boore, and Kenneth H. Stokoe. Comparison of shear-wave slowness profiles at 10 strong-motion sites from noninvasive sasw measurements and measurements made in boreholes. *Bulletin of the Seismological Society of America*, 92(8):3116–3133, 2002.

[11] T. Bui-Thanh and O. Ghattas. A PDE-constrained optimization approach to the discontinuous Petrov-Galerkin method with a trust region

inexact Newton-CG solver. *Computer Methods in Applied Mechanics and Engineering*, 278:20–40, 2014.

[12] A. J. Bush and D. R. Alexander. Pavement evaluation using deflection basin movement and layered theory. *Transportation Research Record*, 1022(1):16–29, 1985.

[13] Yuanqiang Cai, Honglei Sun, and Changjie Xu. Three-dimensional analyses of dynamic responses of track–ground system subjected to a moving train load. *Computers and Structures*, 86(7):816–824, 2008.

[14] Y. Chou and R. Lytton. Accuracy and consistency of backcalculated pavement layer moduli. *Transportation Research Record*, 1293:72–85, 1991.

[15] F. C. P. de Barros and J. E. Luco. Response of a layered viscoelastic half-space to a moving point load. *Wave Motion*, 19(2):189–210, 1994.

[16] F. C. P. de Barros and J. E. Luco. Stresses and displacements in a layered half-space for a moving line load. *Applied Mathematics and Computation*, 67(1):103–134, 1995.

[17] João Manuel de Oliveira Barbosa, Joonsang Park, and Eduardo Kausel. Perfectly matched layers in the thin layer method. *Computer Methods in Applied Mechanics and Engineering*, 217-220:262–274, 2012.

[18] J. F. Doyle. *Wave propagation in structures: spectral analysis using fast discrete Fourier transforms*. Springer, New York, 2nd edition, 1997.

[19] J. W. Dunkin and D. G. Corbin. Deformation of a layered, elastic, half-space by uniformly moving line loads. *Bulletin of the Seismological Society of America*, 60(1):167–191, 1970.

[20] I. Epanomeritakis, V. Akçelik, O. Ghattas, and J. Bielak. A Newton-CG method for large-scale three-dimensional elastic full-waveform seismic inversion. *Inverse Problems*, 24(3):034015, 2008.

[21] A. Fathi, L. F. Kallivokas, and B. Poursartip. Full-waveform inversion in three-dimensional PML-truncated elastic media. *Computer Methods in Applied Mechanics and Engineering*, 296:39–72, 2015.

[22] A. Fathi, B. Poursartip, and L. F. Kallivokas. Time-domain hybrid formulations for wave simulations in three-dimensional PML-truncated heterogeneous media. *International Journal for Numerical Methods in Engineering*, 101(3):165–198, 2015.

[23] G. Fileccia Scimemi, T. Turetta, and C. Celauro. Backcalculation of airport pavement moduli and thickness using the Lévy Ant Colony optimization algorithm. *Construction and Building Materials*, 119:288–295, 2016.

[24] R. Foinquinos. *Dynamic nondestructive testing of pavements*. Ph.D., The University of Texas at Austin, Austin, TX, 1995.

[25] R. Foinquinos, J. Roësset, and K. Stokoe. Response of pavement systems to dynamic loads imposed by nondestructive tests. *Transportation*

Research Record, 1504:57–67, 1995.

[26] S. François, M. Schevenels, P. Galvín, G. Lombaert, and G. Degrande. A 2.5d coupled fe–be methodology for the dynamic interaction between longitudinally invariant structures and a layered halfspace. *Computer Methods in Applied Mechanics and Engineering*, 199(23):1536–1548, 2010.

[27] T. F. Fwa. *The handbook of highway engineering*. Taylor and Francis, Boca Raton, 2006.

[28] P. Galvín and J. Domínguez. Analysis of ground motion due to moving surface loads induced by high-speed trains. *Engineering Analysis with Boundary Elements*, 31(11):931–941, 2007.

[29] G. Y. Gao, Q. S. Chen, J. F. He, and F. Liu. Investigation of ground vibration due to trains moving on saturated multi-layered ground by 2.5D finite element method. *Soil Dynamics and Earthquake Engineering*, 40:87–98, 2012.

[30] Amit Goel and Animesh Das. Nondestructive testing of asphalt pavements for structural condition evaluation: a state of the art. *Nondestructive Testing and Evaluation*, 23(2):121–140, 2008.

[31] S. Grenier and J. Konrad. Dynamic interpretation of falling weight deflectometer tests on flexible pavements using the spectral element method: backcalculation. *Canadian Journal of Civil Engineering*, 36(6):957–968, 2009.

[32] H. Grundmann, M. Lieb, and E. Trommer. The response of a layered half-space to traffic loads moving along its surface. *Archive of Applied Mechanics*, 69(1):55–67, 1999.

[33] R. Hadidi and N. Gucunski. Comparative study of static and dynamic falling weight deflectometer back-calculations using probabilistic approach. *Journal of Transportation Engineering*, 136(3):196–204, 2010.

[34] K. Hall and A. Mohseni. Backcalculation of asphalt concrete-overlaid portland cement concrete pavement layer moduli. *Transportation Research Record*, 1293:112–123, 1991.

[35] R. Harichandran, T. Mahmood, A. Raab, and G. Baladi. Modified Newton algorithm for backcalculation of pavement layer properties. *Transportation Research Record*, 1384:15–22, 1993.

[36] N. A. Haskell. The dispersion of surface waves on multilayered media. *Bulletin of the Seismological Society of America*, 43(1):17–34, 1953.

[37] L. F. Kallivokas, A. Fathi, S. Kucukcoban, K. Stokoe, J. Bielak, and O. Ghattas. Site characterization using full waveform inversion. *Soil Dynamics and Earthquake Engineering*, 47:62–82, 2013.

[38] J. W. Kang and L. F. Kallivokas. The inverse medium problem in heterogeneous PML-truncated domains using scalar probing waves. *Computer Methods in Applied Mechanics and Engineering*, 200(1-4):265–283, 2011.

[39] E. Kausel. *An explicit solution for the Green functions for dynamic loads in layered media.* Department of Civil Engineering, School of Engineering, Massachusetts Institute of Technology, Cambridge, MA, 1981.

[40] E. Kausel and J. Roësset. Stiffness matrices for layered soils. *Bulletin of the Seismological Society of America*, 71(6):1743–1761, 1981.

[41] Eduardo Kausel and João M. de Oliveira Barbosa. PMLs: A direct approach. *International Journal for Numerical Methods in Engineering*, 90(3):343–352, 2012.

[42] S. Kim, J. M. Roesset, and K. H. Stokoe. Numerical simulation of rolling dynamic deflectometer tests. *Journal of Transportation Engineering*, 125(2):85–92, 1999.

[43] S. Kucukcoban and L. F. Kallivokas. A symmetric hybrid formulation for transient wave simulations in PML-truncated heterogeneous media. *Wave Motion*, 50(1):57–79, 2013.

[44] Jin H. Lee, Jae K. Kim, and John L. Tassoulas. Dynamic analysis of a layered half-space subjected to moving line loads. *Soil Dynamics and Earthquake Engineering*, 47:16–31, 2013.

[45] Xujie Liang, Y. B. Yang, Pengbin Ge, Hsiao-Hui Hung, and Yuntian Wu. On computation of soil vibrations due to moving train loads by 2.5D approach. *Soil Dynamics and Earthquake Engineering*, 101:204–208, 2017.

[46] J. L. Lions. *Optimal control of systems governed by partial differential equations*, volume Bd. 170;Bd. 170.;. Springer-Verlag, New York;Berlin;, 1971.

[47] M. Liu, H. Liao, and J. Chuang. Dynamic time domain backcalculation of LTPP test sites. *Journal of the Eastern Asia Society for Transportation Studies*, 7:2017–2029, 2007.

[48] W. Liu and T. Scullion. MODULUS 6.0 for Windows: User's manual. Technical report, Texas Transportation Institute, College Station, TX, 2001.

[49] A. Loizos and J. Scarpas. Verification of falling weight deflectometer backanalysis using a dynamic finite elements simulation. *International Journal of Pavement Engineering*, 6(2):115–123, 2005.

[50] Jian-Fei Lu and Dong-Sheng Jeng. A half-space saturated poro-elastic medium subjected to a moving point load. *International Journal of Solids and Structures*, 44(2):573–586, 2007.

[51] R. Lytton. Backcalculation of pavement layer properties. In *Nondestructive testing of pavement and backcalculation of moduli*, volume 1026, pages 3–37. ASTM International, 1989.

[52] J. Mahoney, B. Winters, N. Jackson, and L. Pierce. Some observations about backcalculation and use of a stiff layer condition. *Transportation Research Record*, 1384:8–14, 1993.

[53] J. Maina, W. Steyn, E. van Wyk, and F. le Roux. Static and dynamic backcalculation analyses of an inverted pavement structure. In *Innovation and Sustainable Technology in Road and Airfield Pavement*, volume 723 of *Advanced Materials Research*, pages 196–203, Portland, OR, 8 2013. Trans Tech Publications.

[54] M. S. Mamlouk. Dynamic analysis of multilayered pavement structures—theory, significance and verification. In *Proc., 6th Int. Conf. on Structural Design of Asphalt Pavements*, pages 466–473, Ann Arbor, MI, 1987. Cushing-Malloy, Inc.

[55] H. Mashayekh, L. F. Kallivokas, and J. L. Tassoulas. Parameter estimation in layered media using dispersion-constrained inversion. *Journal of Engineering Mechanics*, page in press, 2018.

[56] R. Meier and G. Rix. Backcalculation of flexible pavement moduli using artificial neural networks. *Transportation Research Record*, 1448:75–82, 1994.

[57] R. Meier and G. Rix. Backcalculation of flexible pavement moduli from dynamic deflection basins using artificial neural networks. *Transportation Research Record*, 1473:72–81, 1995.

[58] Richard D. Miller, Jianghai Xia, Choon B. Park, and Julian M. Ivanov. Multichannel analysis of surface waves to map bedrock. *The Leading Edge*, 18(12):1392–1396, 1999.

[59] P. Mora. Nonlinear two-dimensional elastic inversion of multioffset seismic data. *Geophysics*, 52(9):1211–1228, 1987.

[60] S.-W. Na and L. F. Kallivokas. Partial-differential-equation-constrained amplitude-based shape detection in inverse acoustic scattering. *Computational Mechanics*, 41(4):579–594, 2008.

[61] S. Nazarian and K. H. Stokoe. Use of surface waves in pavement evaluation. *Transportation Research Record*, pages 132–144, 1986.

[62] J. Nocedal and S. J. Wright. *Numerical optimization*. Springer, New York, second edition, 2006.

[63] Choon B. Park, Richard D. Miller, and Jianghai Xia. Multichannel analysis of surface waves. *Geophysics*, 64(3):800–808, 1999.

[64] R. G. Payton. An application of the dynamic Betti-Rayleigh reciprocal theorem to moving-point loads in elastic media. *Quarterly of Applied Mathematics*, 21(4):299–313, 1964.

[65] Robert G. Payton. Epicenter motion of an elastic half-space due to buried stationary and moving line sources. *International Journal of Solids and Structures*, 4(3):287–300, 1968.

[66] N. Rakesh, A. K. Jain, M. A. Reddy, and K. S. Reddy. Artificial neural networks-genetic algorithm based model for backcalculation of pavement layer moduli. *International Journal of Pavement Engineering*, 7(3):221–230, 2006.

[67] R. Roque, B.E. Ruth, and S.C. Sedwick. Limitations of backcalculation and improved methods for pavement layer moduli predictions. In *5th International Conference on the Bearing Capacity of Roads and Airfields*, page 409–417, Trondheim, Norway, 1998. Tapir Publishers.

[68] Nils Rydén, Peter Ulriksen, Choon B. Park, Richard D. Miller, Jianhai Xia, and Julian Ivanov. High frequency MASW for non-destructive testing of pavements — accelerometer approach. In *Symposium on the Application of Geophysics to Engineering and Environmental Problems 2001*, 2008.

[69] M. Saltan, V. Uz, and B. Aktas. Artificial neural networks–based backcalculation of the structural properties of a typical flexible pavement. *Neural Computing and Applications*, 23(6):1703–1710, 2013.

[70] F. Scrivner, C. Michalak, and W. Moore. Calculation of the elastic moduli of a two-layer pavement system from measured surface deflections. *Highway Research Record*, 431:12–24, 1973.

[71] Joo-Won Seo, Soo-Il Kim, Jun-Sung Choi, and Dae-Wook Park. Evaluation of layer properties of flexible pavement using a pseudo-static analysis procedure of falling weight deflectometer. *Construction and Building Materials*, 23(10):3206–3213, 2009.

[72] S. Sharma and A. Das. Backcalculation of pavement layer moduli from falling weight deflectometer data using an artificial neural network. *Canadian Journal of Civil Engineering*, 35(1):57–66, 2008.

[73] N. Sivaneswaran, S. Kramer, and J. Mahoney. Advanced backcalculation using a nonlinear least squares optimization technique. *Transportation Research Record*, 1293:93–102, 1991.

[74] K. H. Stokoe, S. G. Wright, J. A. Bay, and J. M. Roesset. Characterization of geotechnical sites by sasw method. *SAE Technical Papers*, pages 15–25, 1994.

[75] Honglei Sun, Yuanqiang Cai, and Changjie Xu. Three-dimensional steady-state response of a railway system on layered half-space soil medium subjected to a moving train. *International Journal for Numerical and Analytical Methods in Geomechanics*, 33(4):529–550, 2009.

[76] Honglei Sun, Yuanqiang Cai, and Changjie Xu. Three-dimensional simulation of track on poroelastic half-space vibrations due to a moving point load. *Soil Dynamics and Earthquake Engineering*, 30(10):958–967, 2010.

[77] W. T. Thomson. Transmission of elastic waves through a stratified solid medium. *Journal of Applied Physics*, 21(2):89–93, 1950.

[78] J. Uzan. Advanced backcalculation techniques. In *Nondestructive testing of pavement and backcalculation of moduli*, volume 1198, pages 3–37. ASTM International, 1994.

[79] G. Waas. *Linear two-dimensional analysis of soil dynamics problems in semi-infinite layered media.* Ph.D., University of California, Berkeley, CA, 1972.

[80] S.G. Wright, K.H. Stokoe, and J.M. Roesset. *SASW Measurements at Geotechnical Sites Overlaid by Water*, pages 39–57. ASTM, 1994.

[81] Y. B. Yang, H. H. Hung, and D. W. Chang. Train-induced wave propagation in layered soils using finite/infinite element simulation. *Soil Dynamics and Earthquake Engineering*, 23(4):263–278, 2003.

[82] J. Yi and S. Mun. Backcalculating pavement structural properties using a Nelder–Mead simplex search. *International Journal for Numerical and Analytical Methods in Geomechanics*, 33(11):1389–1406, 2009.

[83] Y. Zhao, D. Cao, and P. Chen. Dynamic backcalculation of asphalt pavement layer properties using spectral element method. *Road Materials and Pavement Design*, 16(4):870–888, 2015.

Vita

Hamidreza Mashayekh received his B.Sc. degree in Civil engineering from University of Tehran (Iran) and M.Sc. degree in Geotechnical Engineering from Khaje Nasir Toosi University (Iran). Hamidreza worked in several consulting engineer companies for five years, where he was designing bridges and tunnels. He taught in different universities in Iran as lecturer. In fall 2010, he joined the Department of Civil, Architectural and Environmental Engineering of the University of Texas at Austin, to pursue a Ph.D. degree in Civil Engineering. He was an Assistant Instructor for numerical methods and programing course at the Department of Petroleum Engineering.

Email address: mashayekh@utexas.edu

Permanent address: University of Texas at Austin
Austin, Texas 78758

This dissertation was typeset with LaTeX[†] by the author.

[†]LaTeX is a document preparation system developed by Leslie Lamport as a special version of Donald Knuth's TeX Program.